



**MONASH** University

# **Plasmonic Nanostructures: Synthesis, Functionalization & Sensing Applications**

A thesis submitted in fulfilment of the requirements for the  
degree of  
Doctor of Philosophy

**Wenjuan Yang**

B.Sc.  
M.Sc.

Department of Chemical Engineering  
Monash University

December 2015



## **COPYRIGHT NOTICE**

Under the Copyright Act 1968, this thesis must be used only under the normal conditions of scholarly fair dealing. In particular no results or conclusions should be extracted from it, nor should it be copied or closely paraphrased in whole or in part without the written consent of the author. Proper written acknowledgement should be made for any assistance obtained from this thesis.

I certify that I have made all reasonable efforts to secure copyright permissions for thirdparty content included in this thesis and have not knowingly added copyright content to my work without the owner's permission.

*This Thesis is dedicated to my  
parents & husband*

# TABLE OF CONTENTS

<b>TABLE OF CONTENTS</b> .....	<b>i</b>
<b>ABSTRACT</b> .....	<b>v</b>
<b>DECLARATION</b> .....	<b>viii</b>
<b>ACKNOWLEDGEMENTS</b> .....	<b>ix</b>
<b>LIST OF PUBLICATIONS</b> .....	<b>xi</b>
<b>LIST OF FIGURES</b> .....	<b>xiii</b>
<b>LIST OF TABLES</b> .....	<b>xviii</b>
<b>LIST OF ABBREVIATIONS</b> .....	<b>xix</b>
<b>LIST OF NOMENCLATURE</b> .....	<b>xxii</b>
<b>Chapter 1. Introduction</b> .....	<b>23</b>
<b>Chapter 2. Literature Review</b> .....	<b>31</b>
2.1 Plasmonic Nanoparticles.....	33
2.1.1 The Optical Property of Plasmonic Nanoparticles.....	34
2.1.2 Plasmonic Coupling .....	40
2.1.3 Plasmonic Application in SERS Sensing .....	42
2.2 Fabrication of Plasmonic Nanoparticles .....	44
2.2.1 Top-Down Fabrication.....	46
2.2.2 Bottom-Up Fabrication .....	52
2.3 Plasmonic Nanoparticle Functionalization .....	56
2.3.1. Chemical Functional Groups .....	57
2.3.2. Polymer.....	58
2.3.3. Biomolecules .....	60
2.3.4. Fluorescent Dyes and Others.....	64
2.4 Self-Assembly of Plasmonic Nanoparticles .....	64
2.4.1 Chemical Directed Self-Assembly.....	65
2.4.2 DNA Direct Assembly .....	67
2.4.3 Template Assisted Self-Assembly.....	73
2.5 References.....	76

### **Chapter 3. Probing Soft Corona Structures of DNA-Capped Nanoparticles by Small Angle Neutron Scattering.....91**

3.1	Introduction .....	93
3.2	Methods and Materials .....	94
3.2.1	Materials .....	94
3.2.2	Synthesis of DNA-Capped AuNP Conjugates .....	95
3.2.3	UV Measurement .....	95
3.2.4	Dynamic Light Scattering Measurement .....	96
3.2.5	Small-Angle Neutron Scattering .....	96
3.2.6	Small-Angle X-Ray Scattering .....	97
3.2.7	SANS and SAXS Data Analysis .....	97
3.2.9	Properties of DNA Corona from Models .....	100
3.3	Results and Discussion .....	101
3.3.1	Salt Effects on Conjugates Size .....	101
3.3.2	Salt Effects on Conjugates Shape .....	102
3.3.3	DNA Corona Configuration .....	105
3.3.4	The Temperature Effects on Conjugate Shape .....	109
3.3.5	The Temperature Effects on Conjugate Size .....	111
3.4	Conclusion .....	112
3.5	References .....	113

### **Chapter 4. Hairy Gold Micro/Nanostructure: Synthesis, Characterization and Application in Strain Sensors .....119**

<b>Part 1</b>	<b>Hairy Gold Nanorods: Synthesis, Characterization and Application in Strain Sensors .....</b>	<b>121</b>
4.1	Introduction .....	121
4.2	Experimental Methods.....	122
4.2.1	Materials .....	122
4.2.2	Methodology of Hairy Plasmonic Nanorods Synthesis .....	122
4.2.2	Strain Sensor Fabrication .....	124
4.2.3	Characterization .....	125
4.3	Results and Discussion .....	125
4.3.1	Synthesis of HGNRs .....	125
4.3.2	UV-Vis Characterization of HGNRs .....	128
4.3.3	Morphological Characterization of HGNRs.....	129

4.3.4	The Tuneable Morphology of HGNRs.....	132
4.3.5	Application of HGNRs in Strain Sensor .....	136
4.4	Conclusion .....	138
<b>Part 2</b>	<b>Hairy Gold Bacteria: Synthesis and Characterization .....</b>	<b>139</b>
4.5	Introduction .....	139
4.6	Experimental Methods.....	141
4.6.1	Synthesis of Hairy Plasmonic Bacteria .....	141
4.6.2	Nanowire Length Control by MBA .....	143
4.6.3	Nanowire Size Control by $\text{HAuCl}_4$ and L-ascorbic Acid .....	143
4.6.4	AuNP Seeds Density Control .....	143
4.6.5	Growth Time Control .....	144
4.7	Results and Discussion .....	144
4.7.1	Synthesis of Hairy Plasmonic Bacteria .....	144
4.7.2	Nanowire Length Control by MBA .....	153
4.7.3	Nanowire Size Control by $\text{HAuCl}_4$ and L-ascorbic Acid .....	154
4.7.4	AuNP Seeds Density Control .....	156
4.7.5	Growth Time Control .....	157
4.8	Conclusion .....	158
4.9	References.....	158
<b>Chapter 5.</b>	<b>Self-Assembly Nanoparticle Pyramids: Shape-Dependent Plasmonics and SERS Enhancement.....</b>	<b>165</b>
5.1	Introduction .....	167
5.2	Method and Materials.....	169
5.2.1	Materials .....	169
5.2.2	Synthesis of Gold Nanocrystals .....	169
5.2.3	Nanoparticles Assembly .....	172
5.2.4	Structural and Optical Characterization .....	172
5.2.5	SERS Measurement .....	173
5.3	Results and Discussion.....	173
5.3.1	Fabrication Nanoparticles Assembly Pyramid Arrays .....	173
5.3.2	Morphological Characterization of Pyramid Arrays .....	175
5.3.3	Scattering Property of Pyramid Arrays .....	177
5.3.4	Nanoparticle Shape and Pyramid Structure for SERS Enhancement .....	181

5.4	Conclusion .....	184
5.5	References.....	185
<b>Chapter 6</b>	<b>Conclusions and Recommendations for Future Work .....</b>	<b>189</b>
6.1	Conclusions .....	191
6.2	Recommendations for Future Work .....	193
<b>Appendix</b> .....		<b>195</b>

## ABSTRACT

Nobel metal nanoparticles possess unique materials properties different from their corresponding bulk materials, which have sparked extensive research developments in the field of nanofabrication over the past few decades. In particular, the rational design of plasmonic nanoparticles (“artificial atoms”) is emerging as an exciting route for engineering material properties with high accuracy. Synthetic advances enable the sophisticated control over their size, shape, composition, and morphology, which has led to a wide spectrum of applications including miniaturized optical and electronic device, sensors and photonic circuits, and medical diagnostics and therapeutics. It is expected that the ability to assemble these elementary plasmonic nanoparticle building blocks into well-defined assemblies such as “artificial molecules”, “artificial polymers” or “superacrytals” will further impact the way materials are synthesized and devices are fabricated. Despite the encouraging progresses in synthesizing metallic nanoparticles, it is still far from the capability of constructing any arbitrary nanostructures in a well-controlled manner.

This thesis is dedicated to synthesis and characterisation of a few novel plasmonic nanostructures including hairy plasmonic nanorods, hairy bacteria, nanoparticle pyramids, etc. I have also thoroughly investigated the soft DNA corona structures via small angle neutron scattering (SANS) for the first time.

Soft organic ligand plays a critical role in synthesis and assembly of plasmonic nanoparticles. In chapter 3, SANS was used to investigate soft ligand corona structures using DNA-capped nanoparticles as the model system. Two 15mer DNA strands with palindromic sequence and poly(dT) sequence under high

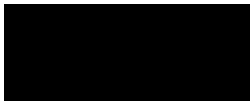
number density packing on gold nanoparticle surfaces, the influence of ionic strength and temperature on DNA corona structures and resultant hybridization has been investigated. Poly(dT) sequences were found to maintain globular corona structures across a range of ionic strengths and temperatures but the corona thickness decreased with increasing salt concentration and increased with increasing temperature. In contrast, palindromic sequenced DNA had globular corona structures in the absence of salt but quickly evolved into dimeric and multimeric structures under high ionic strength or under low annealing temperatures. The structural insights revealed by SANS can help us better understand how DNA controls nanoparticle interaction, which in further guide the design of tailor-made DNA corona structures for customizable designer materials and devices.

In the chapter 4, synthesis and characterization of a new metal nanoarchitecture, hairy gold nanorods (HG NRs), are described. HG NRs were obtained by a seed-mediated growth of nanowires on gold nanorod templates. The hairy nanowires could be obtained in a wider range of ratios of gold precursor to ligand than that reported on solid surfaces or silica beads in the literature. The HG NRs have the unique soft 'hairs' and rigid 'core', allowing for the fabrication of patches with controllable percolation conductivity networks. The soft conducting patches could be used as elastic strain sensors with high stretchability and durability. Remarkably, this nanotemplated approach appears to be general. We found that *E. coli* bacteria could be employed as the template as well, leading to generation of 'hairy plasmonic bacteria' for the first time.

In chapter 5, a combined top-down and bottom-up approach is developed to fabricate structurally well-defined nanoparticle pyramids. The top-down fabricated silicon pyramid well arrays are used as the template to confine self-assembly of pre-synthesized gold nanoparticles. Three types of monodisperse nanoparticles, nanospheres, octahedron, rhomboic dodecahedron, are used as elementary building blocks. For all the three type of nanoparticles, well-defined pyramids could be successfully constructed. The plasmonic properties of these pyramids were thoroughly investigated by micro-UV-visible spectroscopy and dark field spectroscopy. These novel plasmonic pyramids show highly tunable Surface Enhanced Raman Scattering (SERS) enhancements.

## **DECLARATION**

I certify that except where due acknowledgement has been made, the work is that of the author alone; the work has not been submitted previously, in whole or in part, to qualify for any other academic award; the content of the thesis is the result of work which has been carried out since the official commencement date of the approved research program; any editorial work, paid or unpaid, carried out by a third party is acknowledged; and, ethics procedures and guidelines have been followed.

A solid black rectangular box used to redact the signature of the author.

**Wenjuan Yang**

December 2015

## **ACKNOWLEDGEMENTS**

I would like to express my sincere thanks to the people who have given me support in the past 3 years of my graduate study, as listed below.

First and foremost, I am very grateful to have the opportunity to conduct my PhD candidature under the guidance of Professor Wenlong Cheng. It was a great learning experience and I have truly benefitted from his relentless guidance, research enthusiasm and constant demand for excellence. I would also like to extend my thanks to my co-supervisor, Prof. Wei Shen for his availability and constructive suggestions that were determinant for the accomplishment of the work presented in this thesis.

My appreciation and thanks also goes out to those who have helped me in my work in some way or another. They include Dr. Lizhong He, Dr. Elliot Gilbert and Dr. Robert Knott for the help in the small angle neutron scattering experiment and data analysis. I would like to acknowledge the Australian Institute of Nuclear Science and Engineering (AINSE) and Australian Nuclear Science and Technology Organisation (ANSTO) for offering the funding opportunity to conduct the small angle experiment. It was a really great experience.

I would like to acknowledge Melbourne Centre of Nanofabrication, Monash Centre for Electron Microscopy and Department of Chemical Engineering for providing state of the art facilities and instruments. I would also like to thank all the technical staffs for providing inductions and instrument trainings that were important for my research work. In particular Dr John Zhu who provided me detailed training on microscopy.

I acknowledge the financial support provided by Monash University, Department of Chemical Engineering, my supervisor and Professor Kerry Hourigan through MDS and FEIPRS postgraduate scholarships.

Moreover, many thanks go to all my fellow labmates at CHENG NanoBionics Group and friends at Monash. The relationships and friendships formed at Monash University here are now lifelong, many thanks to Yi Chen, Yue Tang, Jye Si, Wei Xiong, Pengzhen Gao, Yongwei Yang, Shu Gong, Upulie Divisekera, Lim Wei Yap, Ramya Chandasekaran, Naveen Jason, Qianqian Shi, Yan Wang, Zhijia Zhang, Dashen Dong, Bin Su, Siyuan Yao, Haili He, Liyuan Zhang, Charlene Ng, Huazhen Li, Jiongiong Lu. Thanks for all helpful insights during lab meetings, the companionship during late nights and helping me to overcome difficult and frustrating moments. I will treasure our friendships and fondly remember all the leisure moments we shared together.

Last but not least, I would like to give my heartfelt thanks to my family and friends who has shared with me my worries, frustrations, and happiness. This work could not have been possible without the support of my parents, sister and my husband. They always give me with their unselfish love, unconditional support and encouragements whenever I needed. My friends were always with me throughout both difficult and fun times.

## LIST OF PUBLICATIONS

### Publications:

1. **Yang, W.**, Lu, J, Gilbert, E., Knott, R., He, L. and Cheng, W. Probing Soft Corona Structures of DNA-Capped Nanoparticles by Small Angle Neutron Scattering. *J. Phys. Chem. C*, 2015, 119, 18773–18778.
2. Mazid, R. R., Divisekera, U., **Yang, W.**, Ranganathan, V., MacFarlane, D. R., Cortez-Jugo, C. and Cheng, W., Biological stability and activity of siRNA in ionic liquids. *ChemComm*, 2014, 50, 13457-13460.

### Manuscripts in Preparation:

1. **Yang, W.**, Yap, L.W., Gong, S. and Cheng, W.. Hairy Gold Nanorods: Synthesis, Characterization and Application in Strain Sensors.
2. **Yang, W.**, Si, K. J., Guo, P. and Cheng, W.. Self-assembly Nanoparticle Pyramids: Shape-Dependent Plasmonics and SERS Enhancement.

### Book Chapter

1. **Yang, W.**, Chen, Y. and Cheng, W. Properties of DNA-Capped Nanoparticles, in *Handbook of Nanomaterials Properties*, B. Bhushan, et al., Editors. 2014, Springer Berlin Heidelberg. p. 1227-1262.

### Conferences

1. **Yang, W.**, Lu, J, Gilbert, E., Knott, R., He, L. and Cheng, W. New Insights on DNA-Capped Nanoparticles by Neutron Scattering. CEPA 4<sup>th</sup>

Annual Chemical Engineering conference, Melbourne, Australia, 30 October 2014. **(Oral presentation)**

2. **Yang, W.**, Shen, W. and Cheng, W. Plasmonic nanoparticle synthesis, functionalization and sensing applications. CEPA 5<sup>th</sup> Annual Chemical Engineering conference, Melbourne, Australia, 28 October 2015. **(Oral presentation)**

## LIST OF FIGURES

Figure 2.1 Electron delocalization. A surface plasmon is characterized as a surface charge density wave at a metal surface. © (2007) Annual Reviews. ....	36
Figure 2.2 Gold nanoparticles – absorption of various sizes and shapes. © (2005) Royal Society of Chemistry .....	38
Figure 2.3 (a) Schematic of the coupling regimes in particle dimers. (b) Scattering coefficient of a set of sphere dimers of radius 40 nm separated by a distance d. The incident light is polarized along the axis of the dimer. © (2010) TAYLOR & FRANCIS GROUP LLC .....	42
Figure 2.4 The fabrication approach of top-down and bottom-up. © (2001). ROYAL ACADEMY OF ENGINEERING. ....	46
Figure 2.5 Schematic illustration of the fabrication process of topographically patterned surfaces semiconductor wafers substrate by conventional photolithography and electroplating. © (2005) American Chemical Society. ....	48
Figure 2.6 A ‘periodic table’ of plasmonic atoms showed various geometrical parameters of plasmonic nanoparticles. © (2011) Rights Managed by Nature Publishing Group. ....	53
Figure 2.7 (a–e) TEM images and (f) summary of the average sizes of gold nanoparticles synthesized in different $\text{Na}_3\text{Ct}/\text{HAuCl}_4$ precursor ratios. © (1973). Rights Managed by Nature Publishing Group.....	54
Figure 2.8 (a) Scheme and average dimensions (in nm) of AuMUA and AgTMA nanoparticles used as the model system. (b) Large-area SEM image of binary crystals obtained from AuMUA/AgTMA precipitates. © (2006) American Association for the Advancement of Science.....	66
Figure 2.9 DNA as entropic ligands in drying-mediated self-assembly. © (2009) Rights Managed by Nature Publishing Group.....	70
Figure 3.1 (a) Schematic of DNA-Au conjugate in the polycore-shell model. SAXS scattering data of T15 (b) and T7-8(c) at various salt concentrations (0M, 0.5M, and 1M). Solid lines show the fits by Schulz distribution of spheres. ....	102
Figure 3.2 SANS scattering data of T15(a) and T7-8(b) at various salt concentrations (0M, 0.5M, 1M). Solid lines show the fits by poly core-shell model. ....	102

Figure 3.3 (a) $p(r)$ function and (b) size distribution of T15 and T7-8 conjugates at various salt concentrations obtained from IFT analysis and DLS measurements respectively. (c) and (d) represent a scheme for the salt effect on poly(dT) DNA and palindromic DNA. ....	103
Figure 3.4 DNA adsorption curves of different initial DNA: AuNP ratios. The dots show the number of moles of DNA adsorbed per nanoparticle; the error bars represent the standard deviation of six independent measurements. Solid lines correspond to the fits calculation. ....	106
Figure 3.5 SANS scattering data of T15 (a) and T7-8 (b) as a function of temperature. The plotted data are offset for clarity as follows: 10x for T15 70°C and T7-8 46°C; 20x for T15 46°C and T7-8 70°C, 30x for T15 30°C. ....	110
Figure 3.6 (a,b) $p(r)$ distribution of T15 and T7-8 conjugates computed at various temperatures (30°C, 46°C, 70°C, 22°C) in 0.5M salt buffer. Insets are scheme of temperature effect on poly (dT) sequenced DNA and palindromic sequenced DNA. ....	111
Figure 4.1 Schematic of hairy gold nanorods synthesis process.....	126
Figure 4.2(a, b, c, d) characterization of morphology of HGNRs synthesis TEM images of Au nanorods and silica coated nanorods. ....	127
Figure 4.3 (a) UV-Vis spectra in process synthesis of HGNR, (b) Optical evolution and (c) UV-Vis spectra of HGNR growth. ....	128
Figure 4.4 SEM images of (a) HGNR, (b) zoom in nanorod core. ....	129
Figure 4.5 SEM images of HGNRs with (a) super long nanowires and (b) high density nanowires. ....	130
Figure 4.6 TEM images of (a) whole HGNR (b) NR core. (c) HRTEM image of silica shell and nanowire root interface region. Inset is a selected area electron diffraction pattern of HGNR, showing the (111), (200), (220) and (311) reflections of gold. ....	131
Figure 4.7 (a, b, c, d) HRTEM images of four continuous parts along a typical nanowire started at silica shell. Inset is the whole view of nanowire heightened high resolution parts. ....	132
Figure 4.8 The length of nanowire tuned by the concentration of nanorod seed (0.034nM, 0.017nM, 0.0067nM, 0.0033nM). Insets are the corresponding SEM images of various length nanowires. ....	133

Figure 4.9 SEM images of gold nanowires grew at different mole ratio of $\text{HAuCl}_4$ to MBA. The molar ratio of $\text{HAuCl}_4$ and MBA is at (a) 1.25, (b) 2.5, (c) 25, (d) 75 and (e) 3. ....	135
Figure 4.10 SEM image of nanoparticles obtained from seed growth without silica substrate, under otherwise the same reaction conditions as for Figure 4.4. ....	136
Figure 4.11 (a) possible mechanism of HG NR film before and under strain. (b) Resistance-time characteristics of the sample's stretchability test for three applied strain. (1V, 0.5 Hz) (c) The durability test under a strain of 5% at a frequency of 0.5 Hz.....	137
Figure 4.12 When the amount of water is excess in the reaction system, there will be unwanted $\text{SiO}_2$ nanoparticles in the final product.....	145
Figure 4.13 E. coli cell surface coated with silica. SEM images of: a, b) bare (uncoated), and d, e) silica-coated cell. The corresponding photographs of the coating at the initial and final stage of reaction: c) bare (uncoated), and f) silica-coated cell. ....	146
Figure 4.14 SEM images of bare (uncoated) bacteria cell and silica-coated cell after 5 days. ....	147
Figure 4.15 Schematic of functionalization bacteria@ $\text{SiO}_2$ surface with APTES. ....	148
Figure 4.16 UV-Vis spectrum of 2.5 nm Au seed nanoparticle. The corresponding photographs of Au colloidal nanoparticles (inset) confirms UV-Vis spectra results. ....	148
Figure 4.17 Photographs of the process of Au. (a) AuNPs, (b) APTES/Silica/Bacteria. After 2 hour of reaction, the Au/APTES/Silica/Bacteria were obtained by centrifuging (c). This pellet was redispersed in water (d, e). ....	150
Figure 4.18 SEM image of Au/APTES/Silica/Bacteria.....	150
Figure 4.19 TEM images of: a) silica-coated bacteria, b, c) Au/APTES/Silica/Bacteria. ....	151
Figure 4.20 Process of Au nanowires growth. (a) Before the start of the reaction, the solution is colorless. After 5 s (b), 20 s (c), and 30 s (d), the reaction solution color changed from colorless to dark blue. ....	152

Figure 4.21 SEM image of AuNWs/APTES/Silica/Bacteria. It can see that Au nanowires entangled together at the outer layer, however in the inner layer it was found the Au nanowires grow very straight and parallel to each other.....	153
Figure 4.22 SEM images of Nanowire length control by MBA. $\text{HAuCl}_4$ and L-ascorbic acid were at 0.425 and 1.205 mM, and the concentration of MBA was lowered to 27.5 (a), 11 (b), 5.5 (c), and 2.75 (d) $\mu\text{M}$ , respectively.....	154
Figure 4.23 SEM images of Nanowire size control by $\text{HAuCl}_4$ and L-ascorbic acid. ....	155
Figure 4.24 Matrix SEM images of different combinations of MBA and $\text{HAuCl}_4$ - L-ascorbic acid.....	156
Figure 4.25 SEM images of AuNP seeds density control. Concentrations of the gold seeds were diluted the colloid solution to $2.93 \times 10^{14}$ (a) to $2.93 \times 10^{13}$ (b), $2.93 \times 10^{12}$ (c), and $2.93 \times 10^{11}$ (d) particles/mL. Then the obtained Au seed-shell was used to grow nanowires.....	157
Figure 4.26 SEM images of AuNWs growth time control. Growth time was compared between 0, 1, 5, and 15 min. There are no extinguished different between the lengths of growth time.....	158
Figure 5.1 Schematic of fabrication nanoparticles assembly pyramid arrays film and corresponding experimental results of single pyramid SEM images.....	174
Figure 5.2 SEM images of (a) Si wafer template with inverted pyramid pattern at low magnification and (b) transfer RD nanoparticles assembly pyramid arrays. ....	175
Figure 5.3 SEM images of single pyramid building block assembly by (a) RD NPs, (b) tip of pyramid and (c) edge of pyramid; (d) octahedral NP assembly pyramid and (e) tip and (f) edge; (f) octahedral NP assembly pyramid and (h) tip and (i) edge.....	176
Figure 5.4 Darkfield images of (a) RD nanoparticles, (b) octahedral nanoparticles and (c) sphere nanoparticles assembly pyramid arrays at low magnification and high magnification.....	178
Figure 5.5 Schematic of scattering spectra measurement. The pyramid was divided into three parts: tip, side and edge. ....	179
Figure 5.6 Optical images of RD (a), octahedral (d) and sphere (h) nanoparticles assembly pyramid. And their corresponding peak position and intensity of scattering spectra at edge and side of pyramid. ....	180

Figure 5.7 (a, c, e) optical images and SERS imaging of 1078 peak band in Raman spectra of RD, octahedral and sphere nanoparticles assembly pyramid film by laser 785nm. (b, d and f). .....	182
Figure 5.8 (a, b, c) optical image and SERS imaging of 1078 peak band in Raman spectra of RD, octahedral, sphere nanoparticles assembly pyramid film by laser 532nm (b, d and f). .....	183
Figure 5.9 SERS intensity of RD, octahedral and sphere nanoparticles assembly pyramid film under (a) 785 nm and (b) 532 nm laser excitation. ....	184

## LIST OF TABLES

Table 3.1 Rg values obtained from IFT and Guinier fitting of SANS scattering data of T15 and T7-8 conjugates at varies salt concentrations. RH values obtained from DLS measurement. ....	99
Table 3.2 Neutron and X-ray scattering length densities used in the analysis. ....	105
Table 3.3 Fit parameters from SAXS and SANS data using Schulz sphere distribution and poly core shell model respectively. ....	105
Table 3.4 Scattering length of DNA. ....	107
Table 3.5 Shell thickness and SLD of shell obtained from fitting poly core-shell model of conjugates and Rg from IFT and Guinier fitting with changing temperature. ....	112
Table 4.1 The concentrations of gold precursor (HAuCl <sub>4</sub> ) and ligand (MBA) and their mole ratios in the growth solution. ....	134

## LIST OF ABBREVIATIONS

1D	One dimensional
2D	Two dimensional
3D	Three-dimensional
4-ATP	4-Aminothiophenol
AA	Ascorbic acid
AgNPs	Silver nanoparticles
APTES	(3-Aminopropyl) triethoxysilane
APTMS	(3-Aminopropyl) trimethoxysilane
AuNPs	Gold nanoparticles
AuNR	Gold nanorod
AuNWs	Gold nanowires
BCC	Body-centered cubic
BEM	Boundary element method
CPC	Cetylpyridinium chloride
CTAB	Cetyltrimethylammonium bromide
CTAC	Cetyltrimethylammonium chloride
DDA	Discrete dipole approximation
DF	Dark field
DLS	Dynamic Light Scattering
DX	Double-crossover
EBL	Focused electron beam
<i>E. coli</i>	<i>Escherichia coli</i>
EUV	Extreme ultraviolet
FDTD	Finite difference in the time domain method
FIB	Focused ion beam

GSNDs	Gold-silver core-shell nanodumbbells
HGNRs	Hairy gold nanorods
HRTEM	High-resolution transmission electron microscopy
IFT	Indirect Fourier Transformation
IPA	Isopropyl alcohol
LB	Luria–Bertani
LSPR	Localized surface plasmon resonance
MUA	11-Mercaptoundecanoic acid
PCR	Polymerase chain reaction
PDDA	Poly (diallyl dimethylammonium chloride)
PDMS	Poly (dimethylsiloxane)
PEG	Polyethylene glycol
PEI	Polyethyleneimine
PMMA	Poly (methyl methacrylate)
PNIPam	Poly (N-isopropylacrylamide)
PS	Polystyrene
PS-SH	Thiolated-polystyrene
PVP	Poly (vinyl pyrrolidone)
PVA	Poly (vinyl alcohol)
PVME	Poly (vinyl methyl ether)
PX	paranemic-crossover
RD	Rhombic dodecahedral
R <sub>g</sub>	Radius of gyration
SAED	Selected area electron diffraction pattern
SANS	Small angle neutron scattering
SAXS	Small angle X-ray scattering
SEM	Scanning electron microscope

SERS	Surface enhanced Raman scattering
SLD	Scattering length densities
Ss/ds-DNA	Single strand/double strand-DNA
TEM	Transmission electron microscope
TEOS	Tetraethyl orthosilicate
TMA	Tetramethylammonium chloride
TX	Triple crossover
UV-Vis	Ultraviolet-visible

## LIST OF NOMENCLATURE

Å	Angstrom
cm	Centimeter
°C	Degree Celsius
g	Gram
Hz	Hertz
KΩ	kiloohm
M	molar
mg	Milligram
mL	Milliliter
mm	Millimeter
mM	millimolar
M <sub>n</sub>	Manganese
mol	Mole
M <sub>w</sub>	Molecular weight
nm	Nanometer
nM	Nanomolar
μL	Microliter
μm	Micrometer
μM	Micromolar
kV	kilovolts

---

# **Chapter 1. Introduction**

---



## Chapter 1

Over the past decades, nanotechnology has become an exciting forefront research field. Nanotechnology is an interdisciplinary field that focuses on fabrication, manipulating, and characterizing materials having at least one spatial dimension between 1 and 100 nm. When size down to the sub-100 nm length scale, all substances become active in a completely different way than their bulk counterparts [1-3]. The optical, mechanical, chemical, magnetic and electronic properties can be systematically tuned by adjusting the size, shape, composition, and arrangement of nanomaterials [4-6]. These exciting change of properties offer the opportunity to rebuild a brand new materials.

In these changed properties, the optical property of noble metal nanoparticles is the subject of one of the most investigated themes in science with an exponentially increasing number of publications. However, the use of nanoparticles, especially optically active noble metal nanoparticles such as silver and gold, long predates the concept of the nanoscale. Two examples of the early use of nanomaterials are the Lycurgus Cup and medieval stained glass windows. Due to their optical properties in the visible range, they show attractive colors. The Lycurgus Cup is a Roman glass cage cup from the fourth century AD. One of the very unusual features of the cup is its color. When lit from the outside it appears green, lit from within it glows red. The secret of the dichroic effect is achieved by making the glass with tiny proportions of gold and silver nanoparticles "dispersed" in colloidal form throughout the glass material [7]. Similarly, the vivid red and yellow colors of the stained glass used for windows in medieval cathedrals contain gold and silver nanoparticles, respectively.

## Chapter 1

Actually, the metal nanoparticles are formed by the reduction of metallic ions in the glass forming process. It was Michael Faraday in 1857 who first described the scientific strategy of production colloidal gold solution which he called "a beautiful ruby fluid" and demonstrated the variation of solution colors with the size of the gold nanoparticles [8]. Based on Faraday's original findings, later works show that the solutions colors of gold and silver nanoparticles are due to a phenomenon known as localized surface plasmon resonance (LSPR). This phenomenon could be explained by Maxwell's equations that not be extracted. In 1908, Gustav Mie rationalized this phenomenon by providing an analytical solution to Maxwell's equations that describes the extinction spectra (extinction = scattering + absorption) of spherical particles with any size. Many experimental observations could be explained by Mie theory [9]. When a nanoscale metallic nanoparticle is irradiated by light, the oscillating electric field causes the conduction band electrons to oscillate coherently.

This plasmonic resonance has a strong dependence on the geometry and size of the metal nanoparticles, direct surrounding medium, as well as the presence of neighbouring nanoparticles [10-12]. Hence, variation of these parameters allow facile tunability of optical properties in unprecedented ways, opening up numerous potential for a wide range of exciting applications that bring plasmonic nanoparticles to the forefront of research and development.

Rationally design of nanoparticles is emerging as exciting route for engineering material structures at nanoscale dimensions. Substantial progress has been made in the past two decades in the synthesis of nanoparticles. Nanofabrication is the methods and processes of generating nanostructure with minimum

## Chapter 1

dimensions lower than 100 nm [13]. This technology involves nearly every aspect of nanomaterial research and development of their use for complex multifunctional devices with a wide spectrum of applications including miniaturized optical [14] and electronic devices [15, 16], sensors [17] and photonic circuits [18], and medical diagnostics and therapeutics [19, 20]. Generally, the construction of nanomaterials can be divided into two major categories: “top-down and bottom up” fabrication according to the process involved in creating nanoscale structures [13]. Despite the encouraging progresses in synthesizing metallic nanoparticles [21, 22], it is still far from the capability of constructing any arbitrary nanostructures in a well-controlled manner due to limitation of control motions and organize matter with nanometer precision. My contribution to this exciting field can be summarised as following:

- Revealing soft DNA corona structures via small angle neutron scattering (SANS) for the first time;
- Development of a general nanotemplating approach to synthesise plasmonic hairy nanorods and plasmonic hairy bacteria;
- Development of a combined top-down and bottom-up strategy to fabricate plasmonic nanoparticle pyramids.

In this thesis, following this introduction, an elaborate literature review on the optical properties of plasmonic nanoparticles, methodology of synthesising and functionalised plasmonic nanoparticle, as well as self-assembly nanoparticles will be presented in Chapter 2. Chapter 3 concerns itself with theoretical studies on DNA-capped gold nanoparticle by Small Angle Neutron Scattering. Chapter 4 presents the experiential methodology of hairy gold micro/nanostructure. The morphological and plasmonic properties of these nanostructures will be thoroughly characterized. Chapter 5 demonstrates templated self-assembly of

## Chapter 1

nanoparticle pyramidal arrays as Surface Enhancement Raman Scattering substrates. Finally, Chapter 6 summarizes the overall conclusion and envisions some of the future challenges in the field of fabrication of plasmonic nanostructures.

### References

1. Roduner, E., *Size matters: why nanomaterials are different*. Chem. Soc. Rev., 2006. **35**(7): p. 583-592.
2. Chaturvedi, S., P.N. Dave, and N.K. Shah, *Applications of nano-catalyst in new era*. Journal of Saudi Chemical Society, 2012. **16**(3): p. 307-325.
3. Uskoković, V., *Entering the Era of Nanoscience: Time to Be So Small*. Journal of biomedical nanotechnology, 2013. **9**(9): p. 1441-1470.
4. Tan, S.J., et al., *Building plasmonic nanostructures with DNA*. Nature Nanotechnology, 2011. **6**: p. 268-276.
5. H. Sargent, E., *Infrared Quantum Dots*. Advanced Materials, 2005. **17**(5): p. 515-522.
6. Piccione, B., et al., *Size-dependent chemical transformation, structural phase-change, and optical properties of nanowires*. Philosophical magazine (Abingdon, England), 2013. **93**(17): p. 2089-2121.
7. Barber, D.J. and I.C. Freestone, *AN INVESTIGATION OF THE ORIGIN OF THE COLOUR OF THE LYCURGUS CUP BY ANALYTICAL TRANSMISSION ELECTRON MICROSCOPY*. Archaeometry, 1990. **32**(1): p. 33-45.
8. Thompson, D., *Michael Faraday's recognition of ruby gold: the birth of modern nanotechnology*. Gold Bulletin, 2007. **40**(4): p. 267-269.
9. Mie, G., *Beiträge zur Optik trüber Medien, speziell kolloidaler Metallösungen*. Ann. Phys., 1908. **330**(3): p. 377-445.
10. Liz-Marzán, L.M., *Tailoring Surface Plasmons through the Morphology and Assembly of Metal Nanoparticles*. Langmuir, 2005. **22**(1): p. 32-41.
11. Kelly, K.L., et al., *The Optical Properties of Metal Nanoparticles: The Influence of Size, Shape, and Dielectric Environment*. The Journal of Physical Chemistry B, 2002. **107**(3): p. 668-677.

## Chapter 1

12. Liz-Marzán, L.M., *Nanometals: Formation and color*. Materials Today, 2004. **7**(2): p. 26-31.
13. Biswas, A., et al., *Advances in top-down and bottom-up surface nanofabrication: Techniques, applications & future prospects*. Advances in Colloid and Interface Science, 2012. **170**(1–2): p. 2-27.
14. Schuller, J.A., et al., *Plasmonics for extreme light concentration and manipulation*. Nat Mater, 2010. **9**(3): p. 193-204.
15. Shipway, A.N., E. Katz, and I. Willner, *Nanoparticle Arrays on Surfaces for Electronic, Optical, and Sensor Applications*. ChemPhysChem, 2000. **1**(1): p. 18-52.
16. Ozbay, E., *Plasmonics: Merging Photonics and Electronics at Nanoscale Dimensions*. Science, 2006. **311**(5758): p. 189-193.
17. Anker, J.N., et al., *Biosensing with plasmonic nanosensors*. Nat Mater, 2008. **7**(6): p. 442-453.
18. Maier, S.A., et al., *Local detection of electromagnetic energy transport below the diffraction limit in metal nanoparticle plasmon waveguides*. Nat Mater, 2003. **2**(4): p. 229-232.
19. Lal, S., S.E. Clare, and N.J. Halas, *Nanoshell-Enabled Photothermal Cancer Therapy: Impending Clinical Impact*. Accounts of Chemical Research, 2008. **41**(12): p. 1842-1851.
20. Yavuz, M.S., et al., *Gold nanocages covered by smart polymers for controlled release with near-infrared light*. Nat Mater, 2009. **8**(12): p. 935-939.
21. Jin, R., et al., *Controlling anisotropic nanoparticle growth through plasmon excitation*. Nature, 2003. **425**(6957): p. 487-490.
22. Wang, C., et al., *A General Approach to the Size- and Shape-Controlled Synthesis of Platinum Nanoparticles and Their Catalytic Reduction of Oxygen*. Angewandte Chemie, 2008. **120**(19): p. 3644-3647.

## Chapter 1

---

## **Chapter 2. Literature Review**

---



## Chapter 2

Due to the unique properties of nanoparticles that different from their corresponding bulk counterparts, there has been increasing research efforts in the development of nanoparticle fabrication. The first part of this literature review provides a summary of optical property of plasmonic nanoparticle and the use of this property in Surface Enhanced Raman Scattering (SERS). Synthesis of plasmonic nanoparticle using both top down and bottom up methodology for improved morphology and property are also reviewed. Furthermore, this chapter summarizes the recent studies in different categories of functional agents for nanoparticle stabilization and application. An extensive review of DNA capped gold nanoparticle and its special properties is included as well. The last part of this literature review outlines the fabrication of nanoparticles assembly, which is a new direction of nanotechnology development. Although many nanoparticles had been synthesised and found a wide range of applications, this review identified a number of issues associated with nanoparticle synthesis and their performance.

### 2.1 Plasmonic Nanoparticles

Rational design of nanoparticles (“artificial atoms”[4]) is emerging as an exciting route for engineering material structures at nanoscopic dimensions. Such nanoparticles are provided for well-defined morphologies with high accuracy and unprecedented properties different from their bulk counterparts. Substantial progress has been made in the past two decades in the synthesis of nanoparticles (particularly, plasmonic nanoparticles, quantum dots, and magnetic nanoparticles, etc.). All of those nanoparticles constitute a library at the nanoscale with a sufficient degree of control over the size, shape, composition, and morphology, which has led to a wide spectrum of applications including

## Chapter 2

miniaturized optical[14] and electronic devices[15, 16], sensors[17] and photonic circuits[18], and medical diagnostics and therapeutics[19, 20]. It is expected that the ability to assemble these elementary nanoparticles into well-defined assemblies (“artificial molecules” [23, 24], “artificial polymers” [25, 26], “superacrystals” [27-32]) will further impact the way materials are synthesized and devices are fabricated. Among all the building-blocks, plasmonic nanoparticles are generating much enthusiasm for their unique optical properties, facile surface chemistry, and appropriate size scale.

### 2.1.1 The Optical Property of Plasmonic Nanoparticles

The optical property of metal materials can be characterized by the Dude model function, which describes how materials interact with electromagnetic radiation. The Dude model assumes that metals consist of a free electron gas known as plasma that moves within the positively charged ion cores. In metal materials, the dielectric function  $\varepsilon(\omega)$  can be describes as:

$$\varepsilon = 1 - \frac{\omega_p^2}{\omega^2 + i\Gamma\omega} \quad (1)$$

where  $\omega$  is frequency,  $\Gamma$  is the plasmon damping in the metal,  $\omega_p$  is the plasma oscillation frequency of the free electron gas, which can be calculated by the electronic density  $n_e$  of the metal,

$$\omega_p = \sqrt{\frac{n_e e^2}{m_e \varepsilon_0}} \quad (2)$$

where  $n_e$  is the density of electrons,  $e$  is the electric charge,  $m_e$  is the effective electron mass and  $\varepsilon_0$  is the permittivity of vacuum.

## Chapter 2

A quantum of plasma oscillation is plasmon in the excitation of the light. Plasmon generated by the metal material, at the surface or in the nanostructures would behave different optical properties. Plasmon are collective oscillation of conduction band electron in response to light, which formed at the metal surface. This surface-bound electromagnetic wave is known as a surface plasmon. The surface plasmon propagates at the interface between the metal and dielectric. The energy of surface plasmon wave is always smaller than energy of bulk plasmon and the plasmon frequency is  $\omega_{sp} = \frac{\omega_p}{\sqrt{2}}$ . The surface plasmon cannot simply be achieved by illuminating a metal surface with light passing through; it needs to be excited under frequency and the wave vector. The wave vector  $k_{sp}$  is derived by

$$k_{sp} = \frac{\omega}{c} \sqrt{\frac{\epsilon_d \epsilon_m}{\epsilon_d + \epsilon_m}} \quad (3)$$

where  $\epsilon_m$  is the dielectric function of the metal,  $\epsilon_d$  is the dielectric surrounding. The surface plasmon resonance (Fröhlich frequency) peak that gives rise to the color of the spherical NP is observed when  $\epsilon_r = -2\epsilon_m$ .

Under external electromagnetic field, free electrons in metal nanostructures create a collective oscillation restricted by the boundaries of the nanostructure. These oscillations are known as localized surface plasmon[33] (Figure 2.1). Since localized surface plasmon do not carry any momentum, only the energy needs to be matched in order to excite the electrons that mean that free photons can be used for excitation and no momentum matching is needed. Consequently, exploration of localized surface plasmon can be done by rather simple optical equipment.

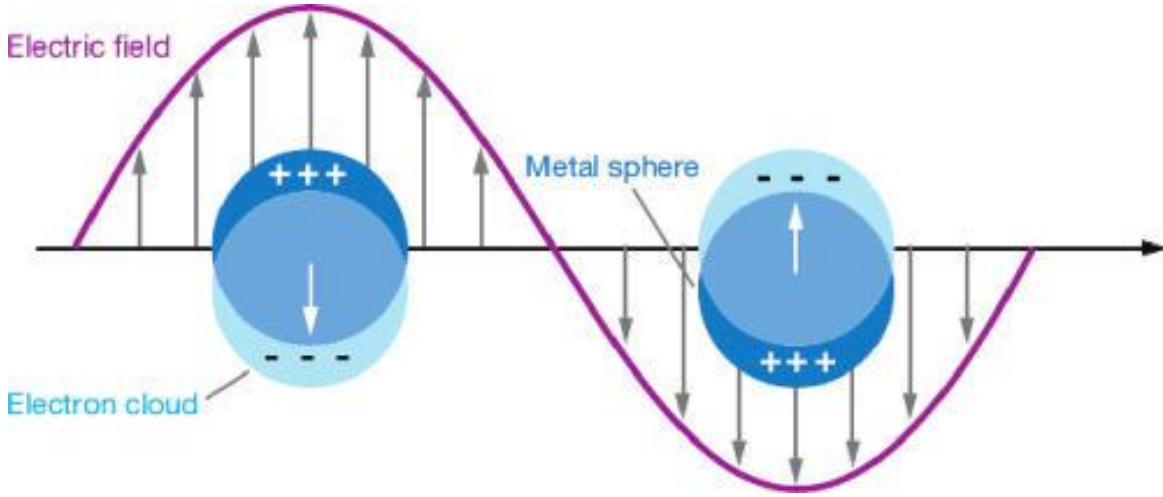


Figure 2.1 Electron delocalization. A surface plasmon is characterized as a surface charge density wave at a metal surface. © (2007) Annual Reviews.

A fascinating aspect of plasmonic nanoparticles is that their optical properties are strongly affected by structural parameters such as size, shape, material composition and the surrounding dielectric environment[10, 11]. The origin of surface plasmon resonance come from the coherent collective oscillations of conduction electrons upon interaction with incident light (an electromagnetic radiation)[34]. The simplest metal nanostructure is single spherical nanoparticles. Gustav Mie was the first to develop theoretical understanding of SPR of metal nanoparticles, which can predict the plasmonic properties of spherical metallic nanoparticles as a function of size and dielectric environments [9]. According to Mie theory, the extinction cross-section,  $C_{\text{ext}}$ , for the scattering of a metallic nanosphere is given by[4]:

$$c_{\text{ext}}(\omega, R) = 12\pi \frac{\omega R^3 \varepsilon_m^{3/2}}{c} \frac{\varepsilon_2(\omega, R)}{[\varepsilon_1(\omega, R) + 2\varepsilon_m]^2 + \varepsilon_1(\omega, R)^2} \quad (4)$$

where  $R$  is the radius,  $c$  is the speed of light,  $\varepsilon_m$  is the dielectric constant of the surrounding medium (assumed to be frequency-independent),  $\omega$  is the frequency

## Chapter 2

and  $\varepsilon(\omega, R) = \varepsilon_1(\omega, R) + i\varepsilon_2(\omega, R)$ , such that  $\varepsilon_1(\omega, R)$  and  $i\varepsilon_2(\omega, R)$  are the real and complex parts of the material dielectric constant, respectively.

Evidently, from this equation, size and dielectric properties of both the material and environment are the factors that determine plasmonic signatures of spherical metal nanoparticles. Based on this insight, tuning the size of corresponding nanoparticles is one feasible way to engineer the position and strength of plasmonic resonance bands[35]. The Mie theory is a simple and efficient model to describe the optical response of sphere nanoparticles. But this theory does not conclude the condition that when the nanoparticles size over since the electrons do not undergo a homogenous electric field. Inhomogeneous electric field causes a dephasing of the conduction electrons and a retardation of the dipolar field. The retardation effect decreasing excitation energy results in a red shift of the plasmon resonance spectrum for larger nanoparticles. What is more, particle size getting larger follow with broadens of plasmon band and reduces the intensity.

The shape of the nanoparticles also strongly affects spectral position of the plasmon resonance. Spherical nanoparticles with high symmetry only possess one dipolar resonance, but when the shape is modified and the particles become more asymmetric, multiple dipolar modes can arise which makes the optical response more complex (Figure 2.2) [36]. The dipolar resonance not only depends on the aspect ratio of nanoparticles but also on the actual size of nanoparticles. Nanorods belonging elongated type nanoparticles display both a transverse and a longitudinal localized surface plasmon mode that shows two distinct plasmon resonance peaks at different spectral positions. Several other

## Chapter 2

geometrical features in addition to elongation, affects the plasmon frequency. More complex geometry structure of nanoparticles can result in red shift of the optical response. Especially, the nanoparticles containing the sharper edges and tips produce significant red shift, which is caused by high surface charge density localized at the particles edges and tips. Thus, the optical response of particles originates from the plasmonic response and lightning rod effect at the sharp area of particles. When metal nanoparticles dispersed in a dielectric medium, the repulsive force of nanoparticles reduces by the screening from the medium. So when the plasmonic energy decreases, the spectrum wavelength shifts. This shift applies in the sensing by measuring the dielectric function of the nanoparticles surrounding.

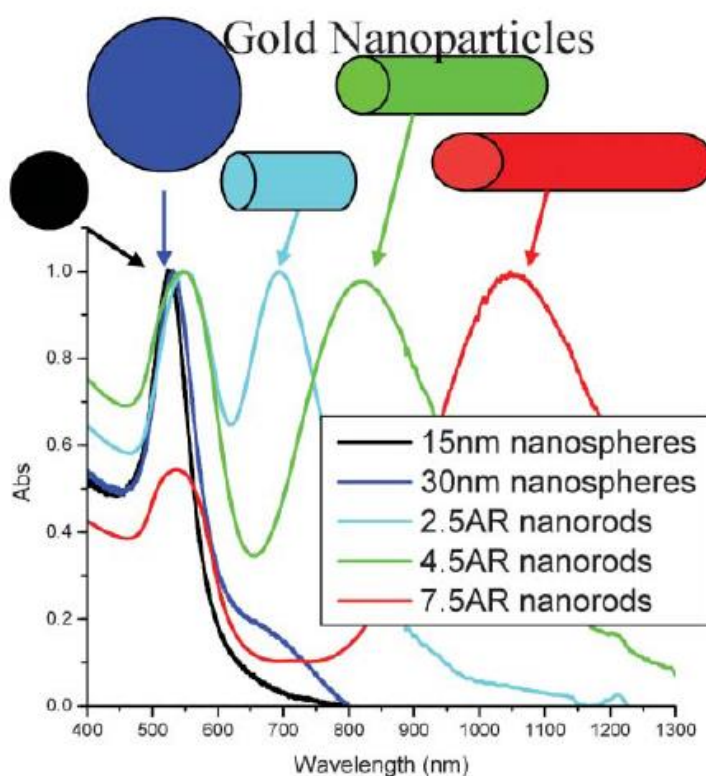


Figure 2.2 Gold nanoparticles – absorption of various sizes and shapes. © (2005)

Royal Society of Chemistry

## Chapter 2

Plasmonic resonance frequencies has the following properties, which can use as a general qualitative design principle,

- Plasmonic resonance frequencies of spherical nanoparticles red-shift with increasing peak intensities as particle size increases;
- The resonance frequencies of non-spherical particles red-shift with increasing corner sharpness and particle anisotropy, and the intensity of the resonance peak increases if charges separate with mirror symmetry;
- The resonance modes increases with the number of ways that the particle can be polarized.

Those general properties of plasmonic nanoparticles are extremely useful to designing desired plasmonic nanostructures for various applications.

The optical response from nanoparticles of different shape, size, and material can be modelled by various numerical methods in both the near- and far- field regions. Computational simulation techniques are important for increasing the knowledge of the physics behind plasmonics and verifying and explaining experimentally results. Computational methods were pioneered by Purcell and Pennypacker using the discrete dipole approximation (DDA) to simulate complex structures, but this did not widely apply until 20 years ago[37]. DDA calculations are based on an array of polarizable dipolar elements considered as point dipoles. This simulation is solutions of the electric field in response to an incident electric field. The polarization of each dipole element caused by the interaction with the local electromagnetic field produced by all other dipole elements plus the external electric field. Later, the new methods rapid gain progress in understanding and control of the response of small metal particles to light, such

## Chapter 2

as finite difference in the time domain method (FDTD) and the boundary element method (BEM). FDTD method relies on solving Maxwell's curl equations in a three-dimensional cubic lattice over time. The optical properties of the material are defined in each cell and the electric and magnetic fields are calculated at a given instant of time. FDTD enables simulation of the optical properties of arbitrary geometries nanoparticles, such as gold nanostars. FDTD method requires a larger parametrization volume, which has to contain outside region of the particles where both incident and reflected fields are allowed to propagate. On the positive view, the computational demand of FDTD grows only linearly with the number of parametrization points.

### 2.1.2 Plasmonic Coupling

The intensity of electromagnetic field surrounding a single metal nanoparticles is limited; by tuning the particles shape with more edges and tips is a way to increase the field intensity. There is enhancement up to 10 times at the nearly field close to single metal particles. An effective strategy to further increase the near field is close distance between interparticles. The coulomb interaction of sufficiently closed particles between caused coupling effect that the surface charge densities of interparticles significantly increased to 100 time or more.

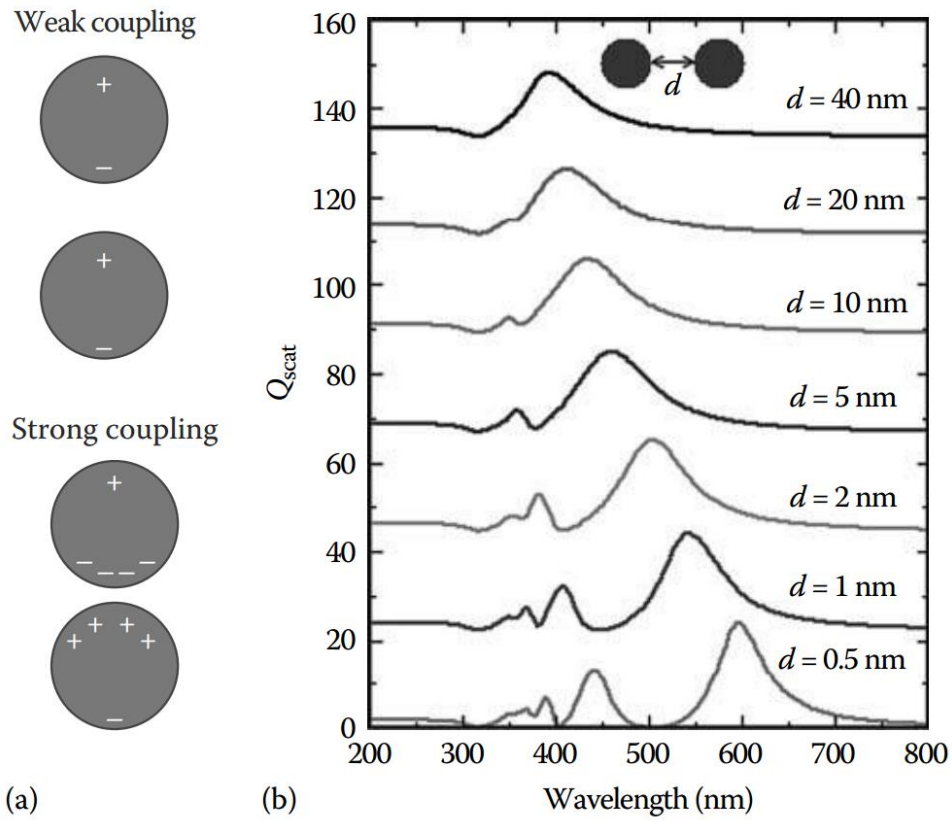
Substantial research efforts have sought to understand interparticle plasmonic coupling using spherical-shaped nanoparticles as a model system[38]. In general, plasmonic coupling does not occur until the edge-to-edge interparticle spacing is less than 2.5 times the particle diameter (that is, the separation-to-diameter ratio,  $\gamma$ , is less than 2.5). Near-field coupling between neighbouring particles results in enhanced electric fields that are confined to small regions

## Chapter 2

between nanoparticles, but it decays quickly with increasing distance. For spherical particles, this typically results in a redshift of the single-particle resonant peak, which decays exponentially with increasing interparticle spacing until the spectrum approaches that of a single particle (Figure 2.3) [39]. ElSayed and co-workers proposed a universal relationship between the exponential decay of the spectral shift with respect to interparticle separation [40]. This relationship is described by the following empirical equation:

$$\frac{\Delta\lambda}{\lambda_0} \approx 0.18 \exp\left[\frac{-(s/D)}{0.23}\right] \quad (5)$$

where  $\Delta\lambda/\lambda_0$  is fractional plasmon shift and  $s/D$  is the separation-to-diameter ratio.



## Chapter 2

Figure 2.3 (a) Schematic of the coupling regimes in particle dimers. (b) Scattering coefficient of a set of sphere dimers of radius 40 nm separated by a distance  $d$ . The incident light is polarized along the axis of the dimer. © (2010) TAYLOR & FRANCIS GROUP LLC

Accordingly, size and shape are the most important parameters among above mentioned points that influence plasmonic properties, and controlling these two parameters is normally sufficient to produce the plasmonic properties required for a given application. Based on all these fundamental theory, the qualitative properties for plasmonic nanoparticles can be summarized as follows[4]. Firstly, the resonance frequencies red-shift and peak intensities increase with increasing diameter of sphere particle; Secondly, for non-spherical particles, the resonance frequencies red-shift with increasing corner sharpness and particle anisotropy, and the intensity of the resonance peak increases if charges separate with mirror symmetry; Finally, the number of resonance peaks increases with the number of ways that the particle can be polarized. Those properties can be further combined with other theoretical predictions and used as guiding line for grouping nanoparticles into well-defined assemblies.

### 2.1.3 Plasmonic Application in SERS Sensing

In term of plasmonic applications, it is critical to select a metal material that offer a strong surface plasmon at the desired resonance wavelength and good stability in ambient condition[41]. For the former request, dielectric function of a metal must own a negative real part,  $\epsilon_r$  and small value of the imaginary part,  $\epsilon_i$  of the dielectric function. Particularly, gold and silver show the higher quality factor across most of the spectrum from 300 to 1200nm [42]. Gold and silver are the

## Chapter 2

most promising, and the most widely used plasmonics materials. One disadvantages of silver is not as stable as gold when exposed to air.

Metal Nanoparticle applied in surface enhanced Raman spectroscopy (SERS) for sensing have taken advantage of facile tunability and plasmonic coupling. SERS is a Raman Spectroscopic technique that provides greatly enhanced Raman signal from Raman-active analyte molecules that have been adsorbed onto certain specially prepared metal surfaces [43]. The Raman molecules are easily attached on the nanoparticles surface and the light intensity can be significantly amplified to  $10^6$ - $10^8$ . This enhancement sufficiently enhanced the sensitivity and even Raman signals large enough to enable single-molecule detection.

There are two mechanisms for Raman signal enhancement. The first mechanism is electromagnetic enhancement which dependent on the presence of the metal nanostructure, the nanoparticles concentrate the resonance between the surface Plasmon of the nanostructure and the excitation and scattered fields in Raman process. Another mechanism is chemical enhancement, when a molecule is places on nanostructure, the excited Plasmon resonances in the nanostructures lead to strongly enhanced scattering signals from the molecules [44-46]. Total enhancement factors obtained in SERS can reach 14 orders of magnitude which electromagnetic enhancement plays a key role in the enhancement, and single molecule enable detected [47-49]. One of the most remarkable study of SERS focus on the order plasmonic arrays to generate more hot spots to enhance the Raman signal [50, 51].

## Chapter 2

The reproducibility and sensitivity of SERS detection could be improved by using novel plasmonic nanoparticles. In a different approach, Lim et al. applied gap-tailorable gold-silver core-shell nanodumbbells (GSNDs) for SERS detection of DNA [52]. In this demonstration, a large gold nanoparticle was functionalized with Raman-active Cys3 dye-tagged DNA with sequences complementary to half of the target DNA; a small gold nanoparticle was functionalized with DNA with sequences complementary to other half of the target DNA. Thus, in the presence of DNA targets, a dimeric structure was formed, which was followed by silver coating for signal enhancement [52]. The significance of this work is that it offers a high-yield synthetic method to produce highly reproducible plasmonic nanostructures for SERS based detection. Due to the signals coming from the single plasmonic nanostructures, this method could be potentially used to detect the single molecules. It was observed that the calculated enhancement factor for the GSND was  $2.7 \times 10^{12}$ , which is large enough for single-molecular detection.

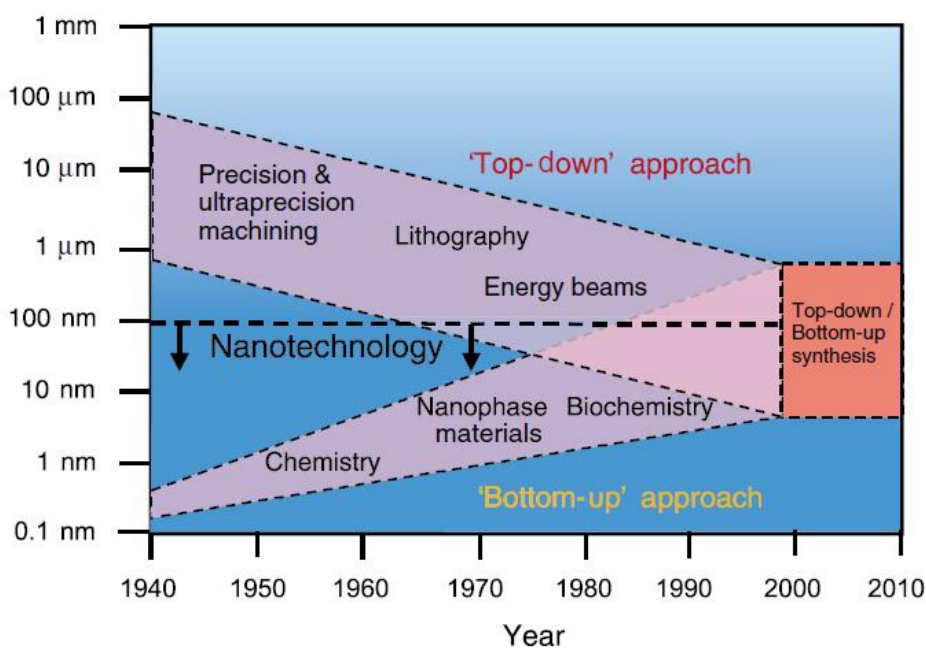
### 2.2 Fabrication of Plasmonic Nanoparticles

Nanofabrication is the methods and processes of generating nanostructure with minimum dimensions lower than 100nm[13]. This technology involves nearly every aspect of nanomaterial research and development of their use for complex multifunctional devices with tremendous application including medicine, sensing, electronics and energy etc. Particularly, the plasmonic nanofabrication shows the unprecedented growth of theoretical knowledge and understanding of their specific characteristics related to various nanostructure, particular application and engineered nanomaterial into multifunctional devices. Correspondingly, the need of nanofabrication techniques approaches are developing with respect to

## Chapter 2

large scale, commercial fabrication, atomic precision control desired structure and the property of mechanical, optical, electronic [53-55].

Generally, the construction of nanomaterial can be divided into two major categories (Figure 2.4): “top-down and bottom up” fabrication according to the process involved in creating nanoscale structures[13]. Top-down fabrication corresponds to utility lithography tool in order to produce a material from larger scale to nanoscale structure with desired features. Whereas, the bottom-up fabrication is novel method for programing of atoms, molecules, and other small components into nanostructure[56]. The major aim of fabrication is development techniques for the controlled fabrication of complex and multicomponent nanomaterial that is needed for advanced functional applications. In this part of review, the developed technology of top-down fabrication and bottom-up fabrication will be described, their advantages and shortages will be also systematically point out as well.



## Chapter 2

Figure 2.4 The fabrication approach of top-down and bottom-up. © (2001). ROYAL ACADEMY OF ENGINEERING.

### 2.2.1 Top-Down Fabrication

The benefits of this engineering approach enable to produce very regular, well-defined structures. It can produce plasmonic nanostructure with highly controllable size, shape and spacing between nanoparticles[13]. What is more, it enables the fabrication of patterned substrate with tuneable plasmonic property which applied widely in the SERS sensing[57]. Top down method is frequently used for making objects out of stable engineering materials and applied for the fabrication of microstructures in the semiconductor industry. However, it has problems building complex three-dimensional structures, the high cost is also another problem needed to be considered.

Two main strategies of lithography exist: parallel and serial patterning. The parallel pattern fabricate the whole patterned in one mask, while, the serial patterning method generate individual features. Parallel patterning methods are high throughput and an inexpensive alternative. However, the resolutions of this strategy is low caused by the mask related issues and intrinsic limitations of the radiation source. Comparing with parallel patterning strategy, serial patterning methods yield the very high resolutions, although the writing process is slow and the high cost [58].

There are four main steps of pattern transferred into the underlying substrate: (1) etching: the substrate is firstly coated with a sacrificial layer and a resist layer, into which the pattern is generated by lithography. The exposed areas of the sacrificial layer are etched and the resist removed in a processes generally

## Chapter 2

referred to as lift-off, generating recessed features. (2) re-growth: the areas unprotected by the resist are regrown and the resist is removed, generating elevated structures. (3) Doping: the substrate areas exposed through the resist are chemically modified through doping by diffusion or implantation and the resist removed, generating a flat structure. (4) lift-off: metal is deposited into the holes of the resist generated by lithography and the resist is removed, yielding elevated features[59].

Lithography technique generate pattern on a thin polymer film that resist or sensitive to various of radiation, such as photo, electrons or X-rays electrons, ions, and neutral atoms[13]. Although different expose radiation sources used in various method of lithography, the basic mechanism and general process is similar. The detail information various method of lithography will be reviewed in the flowing paragraphs.

### 2.2.1.1 Photolithography

Photolithography is the most widely used technique in the semiconductor industry, which using a radiation source with wavelength in the visible spectrum, so it is also called optical lithography. The basic process of photolithography concludes (Figure2.5) [60] : first, a semiconductor wafers substrate is coated with photoresist material that is an organic, light-sensitive film. Depending on the chemical nature of the resist material, the photoresist has two types: positive and negative type. After the substrate is exposed to light through the mask, for positive resists material, underlying material is to be removed in the developing solutions and the exposed regions are dissolved; In contrast, in the case of a negative resist material, the unexposed areas are etched away in the developing

## Chapter 2

solutions and this leads to the production of a negative tone image of the shadow mask[61].

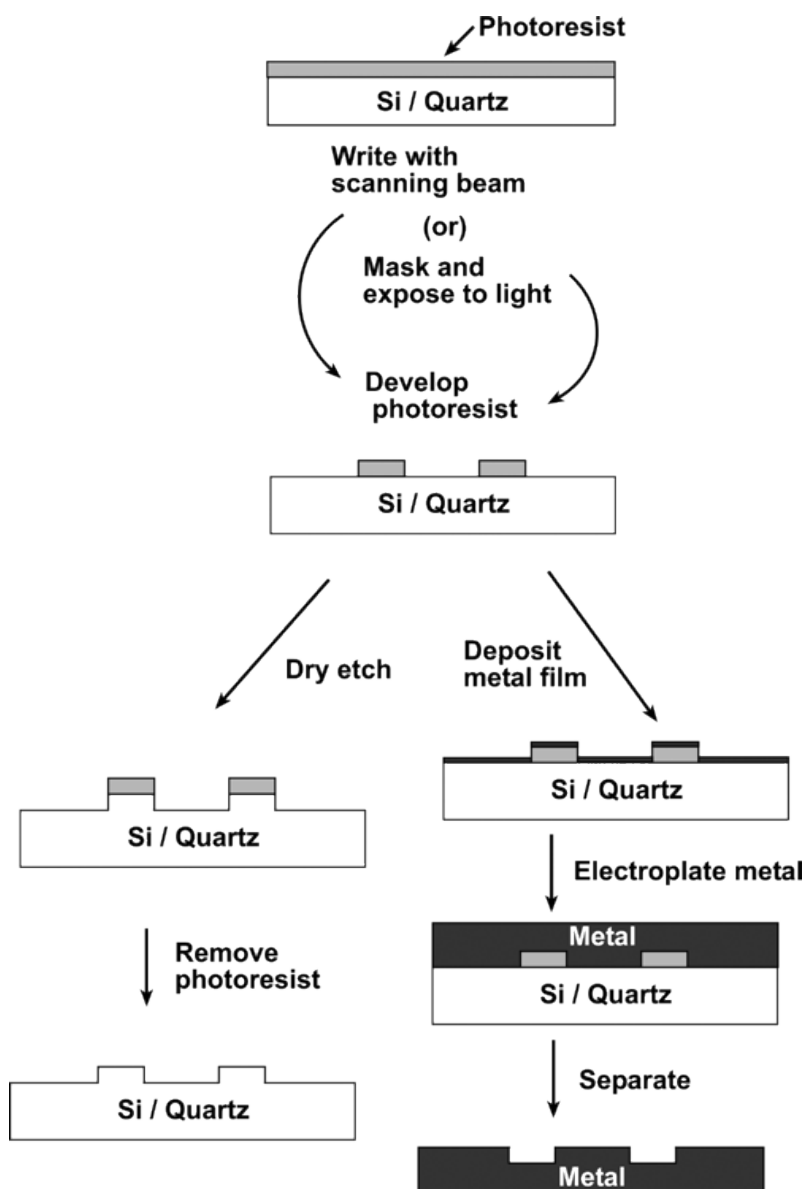


Figure 2.5 Schematic illustration of the fabrication process of topographically patterned surfaces on semiconductor wafers substrate by conventional photolithography and electroplating. © (2005) American Chemical Society.

## Chapter 2

Although conventional photolithography are technical simplicity and parallel processing, it is restricted by the limited resolution which reaches 1  $\mu\text{m}$  using light of 400 nm [61, 62]. The low resolution of fabrication is resulted in the diffraction limit of the light used. To achieve a better resolution, the first vital parameter is lens numerical aperture, defined in Equation (6)

$$N_A = n \sin \theta \quad (6)$$

where  $n$  is the refractive index of the medium through which the light travels and  $\theta$  is the angle of light collected at the focal point [61].

From the Rayleigh criterion, the relation of the minimum distance and  $N_A$  can be given by Equation (7)

$$L_{\min} = k \frac{\lambda}{N_A} \quad (7)$$

where  $L_{\min}$  is the minimum feature line width,  $\lambda$  is the radiated light wavelength and  $k$  is dimensionless scaling factor, which depend on the resist material, process technology and image formation technique[63].

From the above equation, the feature resolution can be improved by either using a short light wavelength or increasing  $N_A$ [64]. The former improvement example is UV lithography that developed in the semiconductor industry, and the extreme ultraviolet (EUV) lithography is used as light source, generating the feature sizes blew 30nm[65]. Another improvement is immersion lithography, in which the space between the lens and the substrate is immersed in medium with a relative higher refractive index to gain smaller feature size. The principle of immersion lithography is well known and widely used in biology for microscopy imaging. The development of photo lithography is progressed via the improvement of leis

## Chapter 2

design with low aberration levels and with the advance in process focus control during the chip fabrication. Feature sizes of pattern below 30 nm have been produced with EUV lithography. These techniques are considered as the next generation optical lithography strategies because the instrument is not easily accessible and with tremendous fabrication cost.

### 2.2.1.2 Scanning Beam Lithography

Scanning beam lithography is a serial patterning process with similar stamps with conventional lithography technique. In this technique, beam scans over the substrate to write desired patterns into the resist. Three main categories exist: scanned laser beam ( $\sim 250$  nm resolution); focused electron beam (EBL) system (sub 20 nm resolution) and focused ion beam (FIB) system (sub 50 nm resolution)[66]. Surface of substrate beam scanned coat with a resist changing the polymer solubility depending on the charges. A commonly used resist is poly (methyl methacrylate) (PMMA) that commonly used as a positive resist, but also can be used as negative resists.

By reducing the diameter of the beam is achieved high resolution. However, the disadvantage of high resolution is the requirement of long writing time to generate enough exposure for modify the resist. The type of resist also affect the resolution. The resist requires a high energy does yields high resolutions [58]. The resolution and clarity of features can be improved by developing the resist in a cold solution. A high electron does decrease the writing time and also ensure the bottom of the trenches are clean after exposure.

### 2.2.1.3 Soft Lithography

## Chapter 2

Soft lithography as an alternative of photolithography using soft mould. Three-dimensional structures can be obtained by this technique. The mechanism of soft lithography is transfer a pattern from an elastomeric stamp to a surface. Elastomer is common choose poly (dimethylsiloxane) (PDMS) or silicon rubber. The stamp is prepared by pouring PDMS or silicon rubber into a master mould with desired pattern, and then cured, peeled off, substrate acquired with pattern. Several different techniques exist in soft lithography: microcontact printing, replica molding, Microtransfer Molding, Micromolding in Capillaries and solvent-assisted micromolding [67].

This type of lithography has many benefits, such as simple, low-cost and no diffraction limitations. The stamp can be recycled used generation of patterns. A large scale pattern is obtained in one operation and the flexible stamp allows the mould to be fitted on any curve surface[68]. However, there are still many disadvantages of soft lithography technique. The chance of distortion of the elastomeric stamp would increase due to the deformation of the elastomer, which results in the reproducibility decrease and cannot be competent the industry requirement. The quality and precision of this techniques is still not advanced to match the needed for the sophisticated electronic devices. Soft lithography still need more improvement to require the fabrication processes[67].

### 2.2.1.4 Nanoimprint

Nanoimprint is a similar technique with soft-lithography, and use a hard mould to transfer the nanoscale pattern to polymer film. This technique can produce features with size around 10 nm. The process of nanoimprint is following: thermoplastic polymer deposited on the surface of substrate and heated over

## Chapter 2

transition temperature. Then the mould with pattern is pressed against the substrate facing the polymer fill into the mould. After the temperature of polymer down and solidified, the mould removed. If any polymer left in the feature areas it is removed with wet or dry etching. The benefits of nanoimprint technique are a parallel process and high resolution. The main problem in nanoimprinting is the lift time of mould. Under the stress of mould result in easy damage during the print cycles. Nanoimprint and soft lithography are both belong to non-conventional lithography techniques and face many challenges.

### 2.2.2 Bottom-Up Fabrication

An alternative approach of fabrication has emerged, 'bottom-up' nanotechnology, to build up complex entities by using the self-assembling properties of molecular systems. This is more like a chemical or biological approach, also called wet chemical technique. It provides potential to fabricate complex 3-D structures cheaply and in large quantities. However, this fabrication method has disadvantages of irregularity and repeatability.

High-quality metallic nanoparticles with tailorable plasmonic signatures have been synthesized through bottom up fabrication [69]. Careful optimization of synthesis conditions allows rational control over nanoparticle sizes and morphologies[70]. Figure 2.6 highlights the substantial progress in the synthesis of metallic nanoparticles as a periodic table of 'artificial atoms'[4]. Each row exhibits a different level of dimensionality and complexity, ranging from spherical and rod-like shapes, two-dimensional (2D) polygonal shapes, three-dimensional (3D) polyhedral shapes, to branched structures and more complex structures. In

## Chapter 2

each row, the geometric order of the structures (in terms of aspect ratio, number of sides and facets, or number of branches) increases from left to right.

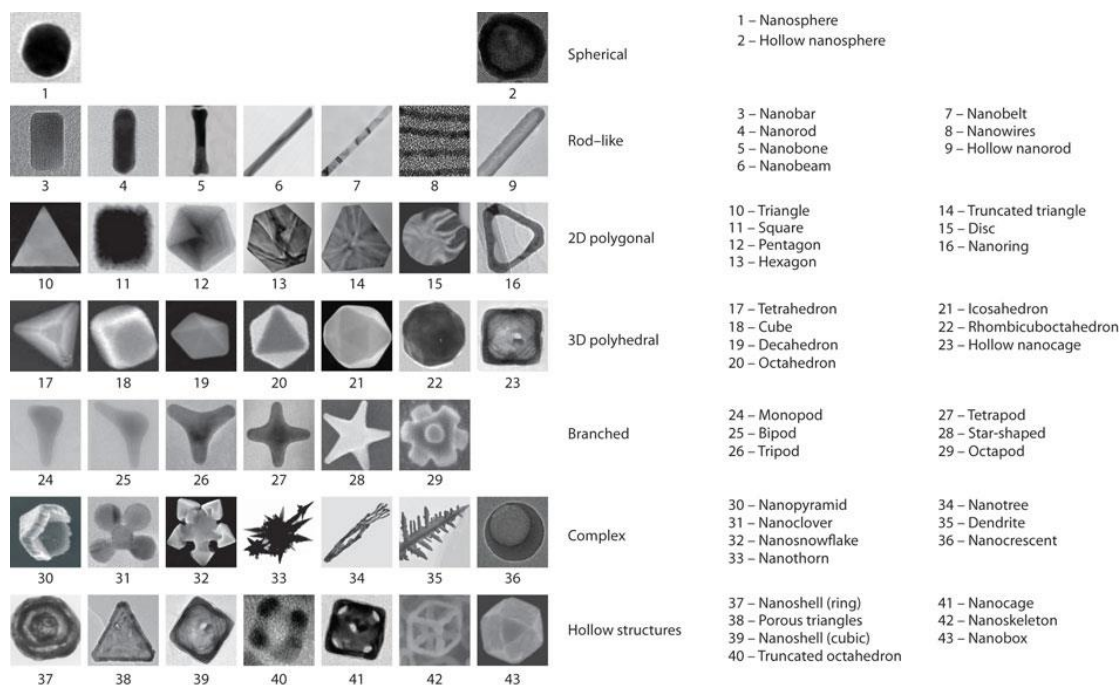


Figure 2.6 A 'periodic table' of plasmonic atoms showed various geometrical parameters of plasmonic nanoparticles. © (2011) Rights Managed by Nature Publishing Group.

As a model building-block, gold nanosphere represents thermodynamically lowest energy state due to the highest surface-to-volume ratio among all shapes. Chemical reduction of gold chloride was firstly conducted by using sodium borohydride and sodium citrate, producing particles with size range of 2~10 and 12~100 nm, respectively[71]. It is clearly demonstrated that the size variation of gold nanoparticles by the citrate reduction can be tuneable by simply varying the concentration of sodium citrate (Figure 2.7) [71]. Gold nanoparticles were grown through a fast nucleation process followed by a diffusion controlled growth [72]. Thus, the size and size distribution of nanoparticles are controlled in a way

## Chapter 2

similar to the Lamar model, which is known as “focusing of size distribution” in the field of nonaqueous solution synthesis of nanocrystals under elevated temperatures[73]. In this synthesis approach, the temperature of reaction depends on the reaction kinetics and oxidation potential, so the temperature plays a key role in the nanoparticles formation. The citrate capped gold nanoparticle enable to the further surface functionalization with proteins, DNA and other biomolecules. However, the citrate capped nanoparticles are sensitive to pH, ionic strength and easily to form aggregation.

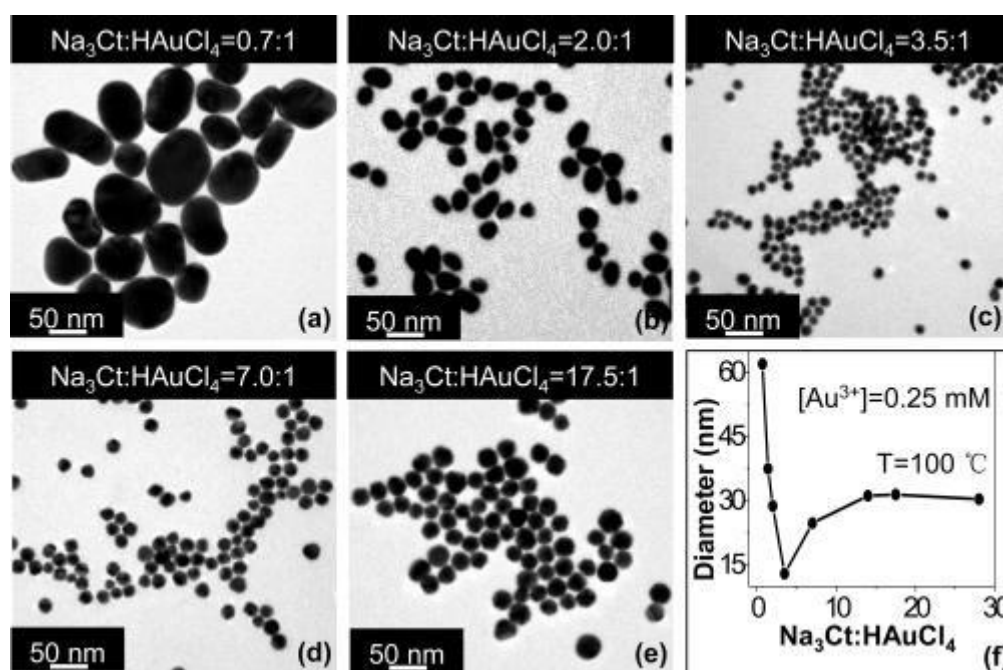


Figure 2.7 (a–e) TEM images and (f) summary of the average sizes of gold nanoparticles synthesized in different  $\text{Na}_3\text{Ct}/\text{HAuCl}_4$  precursor ratios. © (1973). Rights Managed by Nature Publishing Group.

However, such citrate method can only produce quality particles up to  $\sim 50 \text{ nm}$  in diameter, or it will be polydispersed and non-spherical. The synthesis of anisotropic nanoparticles can be achieved by controlling the growth on

## Chapter 2

specific crystal facets. In an alternative way, seed-mediated growth method improved the quality[74]. Firstly, relatively small gold nanoparticles (AuNPs, ~5 nm) were prepared as seeds. Then, larger particles further grow in mild reducing agent. The kinds of capping agents in the further growth solution bind to specific facets of seed, the growth rate reduced at these facts, leading to the growth of nanoparticles into certain geometries. Thus, the shape and size of particles are dependant on the types of agent, concentration of agent and the reaction conditions. The common capping agent in the seed-growth approach is cetyltrimethylammonium bromide (CTAB). This approach successfully restricted the size distribution (~10-15 %) of the resulted products, but a substantial secondary population of smaller nanoparticles is formed apart from growth of the seeds. This could be overcome with an agent capable of selectively reducing gold only when in proximity to particle seeds. In a typical method, hydroquinone is used as reducing agent and improved monodispersity and shape consistency in the 50-175 nm size range[75]. Furthermore, large nanoparticles with diameters of >200 nm can also be fabricated, which has developed the synthesized AuNPs into a greater size range and better size and shape dispersion.

Similarly, anisotropic AuNPs such as gold nanorods (AuNRs) is also fabricated through ligand-limiting nucleation and growth process [69, 70]. Seed-mediated growth represents the most efficient and reproducible approach to synthesize monodispersed AuNRs with the adjustable size, shape, and aspect ratio[76]. It was found that the crystalline structures of the seeds and the presence/absence

## Chapter 2

of  $\text{AgNO}_3$  influence the nucleation and growth. Owing to the high yield (~99%), preparation of AuNRs from single-crystal seeds has received most attraction[77].

Except nanorods, there are other three main groups of anisotropic nanoparticle: platonic, nanoplates and branched. Platonic nanoparticles include five shapes of nanoparticles: tetrahedral, hexahedra, octahedral, dodecahedra and icosahedra. The final shape of nanoparticles can be tuneable by the surfactant or reductant. These nanoparticles are conducted by seed-mediated method with either nanosphere or nanorods as seed to further growth. Due to the sharp corners of triangular and hexagonal nanoparticles, they are interesting in application of surface enhanced Raman scattering (SERS). Synthesis of triangular shaped gold nanoprisms is gradually been well developed, which could be further used as seed particles for larger triangular shaped gold nanoprisms[78]. The final nanoparticles structure is controlled by the reactants in the growth solution. The synthesis of branched nanoparticles is similar with nanoplates, which can be achieved by adjusting the reductant ratio or changing capping agent to form a more complex structure with numbers of sharp tips.

### 2.3 Plasmonic Nanoparticle Functionalization

In order to enhance the nanoparticles stability and convert them to widely application, they typically need to be modified with some organic materials that can provide them with a desired functionality [79]. When one particles is at close proximity to another, nanoparticles are attracted to each other by van der Waals forces, which results in the nanoparticle aggregate. Modified molecules on the nanoparticles surface counteract the attractive van der Waals forces to promote the stability. According to the material of ligand, the particle functional groups

## Chapter 2

can be divided into four categories, chemical functional groups, polymer, biomolecules and fluorescent dyes and others. This part aims to review different strategies of surface modification and functionalization of nanoparticles with a special focus on the conjugate of DNA capped gold nanoparticles.

### 2.3.1. Chemical Functional Groups

At present, the most popular colloidal gold nanoparticles synthesis protocols is the citrate reduction of  $\text{HAuCl}_4$  [80]. Citrate is reported to play two major roles during this synthesis: one is the reducing agent that reduced Au (III) to Au (0) [71], and another is a protecting agent, controlling the growth of the nanoparticles and preventing their aggregation [81]. The synthesised gold nanoparticles are capped by an electric double layer, consisting of citrate and chloride anions and cations attracted to the chloride ions, which results in an electrostatic repulsion between the particles. Further, it is also found that the concentration of citrate can control the size distribution of gold nanoparticles[82]. The size of gold nanoparticles is tuneable in the citrate reduction by varying the initial molar ratio between sodium citrate and gold precursor. The nucleation ratio of gold nanoparticles increased when the concentration of sodium citrate increased, provided that the precursor concentration was fixed. The moderately citrate capped gold nanoparticle enable to the further surface functionalization with proteins, DNA and other biomolecules. However, the citrate capped nanoparticles are sensitive to pH, ionic strength and easily to form aggregation.

Another commonly used capping agent in the synthesis of noble metal nanoparticles is CTAB that form a bilayer wrapping on each metal nanoparticles. The inner layer is the head groups of CTAB molecules, binding to the surfaces

## Chapter 2

of gold nanoparticles, thus leave the hydrophobic tails into water environment. The van der Waals force cause the CTAB to form a head-out counter-layer in solution. The bilayer of CTAB leads to a net positive charge on the CTAB-coated nanoparticle surface, which is crucial for the stability of nanoparticles in aqueous solution. If the CTAB is removed from solution, the nanoparticle would aggregate [83]. The ratio of CTAB to nanorod concentration determines stability, rather than the CTAB concentration. So the critical concentration of CTAB preventing aggregation depends on the nanorod size [84]. However, the major disadvantage of CTAB as capping agent is that it bind strongly to the nanoparticles surface, which results in the hard functional other capping agents. CTAB is highly cytotoxic, the nanoparticles need to be reduced the cytotoxicity and increased the biocompatibility for bioapplicaitons.

### 2.3.2. Polymer

Polymer used as a stable ligand of gold nanoparticles was first reported by Helcher in 1718. The polymer is soluble in a number of organic polar and apolar solvents, as well as in water where it is heavily hydrated, forming random coils with diameters much larger than proteins of the corresponding molecular weight. Owing to its simple structure and chemical stability, it is a prototype of an inert, biocompatible polymer. Polymer commonly used for stabilization include poly (ethylene glycol) (PEG) [85-87], poly (nvinylpyrrolidone) (PVP) [88, 89], poly (4-vinylpyridine) [90, 91], poly(vinyl alcohol) (PVA) [92, 93], poly(vinyl methyl ether) (PVME) [94, 95], polyethyleneimine (PEI) [96, 97], poly(diallyl dimethylammonium chloride) (PDDA) [98, 99], poly(methyl methacrylate) (PMMA) [100, 101] and poly(N-isopropylacrylamide) (PNIPam) [102, 103].

## Chapter 2

There are three approaches widely used for capping polymer on gold nanoparticles[104]. First, “grafting to” approach is thiol-terminated polymer used to synthesis gold nanoparticles and generally produces a sparser coverage [105, 106]. Second, particles synthesis can already be carried out in the presence of polymer[107, 108]. This approach obtains a high dense polymer brush. Third, “Post-modification of pre-formed gold nanoparticles”[109, 110]. In this method, gold nanoparticles are generated in the first stage through conventional methods, followed by the exchange or modification with polymers. Fourth, physisorption on gold nanoparticles by block copolymer micelles, water-soluble polymers, or star block copolymers [111, 112].

PEG is a linear polymer consisting of repeated units of  $-\text{CH}_2-\text{CH}_2-\text{O}-$  and the number of units is dependant on the molecular weight. The non-toxic and inertness properties of PEG give rise to a number of applications in medicine[113], chemistry[114, 115] or biotechnology[116]. PEG-modified particles exhibits remarkable resistance against nonspecific protein adsorption[117], much lower toxicity[118, 119], and longer in vivo circulation time in blood[120]. PEG chain is a hydrophilic polymer with high flexibility, and could assemble into dense palisades of tethered chains to achieve unique properties. When bound to surfaces [121], PEG is against other molecules by steric effects; the incoming molecule is not attracted by electrostatic force and cannot penetrate the hydrated PEG layer. This results in inert hydrophilic surfaces with less ‘stickiness’. The biocompatibility of PEG was result from the dense outer surface, which enables the micelle with a concealment character in the blood compartment, achieving a long circulation.

## Chapter 2

PVP is an organic polymer. In the molecular structure of PVP, the polyvinyl backbone serves as a tail group (hydrophobic) whereas the pyrrolidone group serves as a head group (hydrophilic). Thus, PVP molecules exhibit an amphiphilic feature. The head groups of PVP can interact with surfaces of Au and Ag nanoparticles whereas tail groups can tune the distances among adsorbed head groups. As a result, the surface coverage of Au or Ag nanoparticles can be well controlled by PVP molecules.

### 2.3.3. Biomolecules

Bioapplications of gold nanoparticles are widely spread due to easy synthesis, optical plasmonic properties and very good oxidation resistance. The biomolecules own complex structure and different composition and size, which essentially differ from nanoparticles. Biomolecules used conjugate with nanoparticles including biotin, lipids, peptides, proteins, enzymes, DNA and RNA. There are four strategies of modified biomolecules on the nanoparticles. First, binding to the surface of metal nanoparticles by chemisorption like thiol group. Second, via electrostatic adsorption of negatively charged nanoparticles to the positively charged biomolecules. Third, covalent binding by chemistry[122]. Fourth, non-covalent, affinity-based receptor-ligand systems.

Biotin is a small molecule containing one free carboxylic group, and could be modified with groups, such as  $-NH_2$  or  $-NHS$ , which covalently bound to the nanoparticle surface by conjugation chemistry[122, 123] or binding to the nanoparticles according to the connected ligands[124]. In this kind of conjugate, the properties focus on the solubility and charge of biotin molecule rather than the biological functionality of biotin.

## Chapter 2

DNA is a unique genetic material which virtually exists in almost all known living organisms and viruses. A DNA strand contains a phosphate-deoxyribose backbone and four types of bases: adenine (A), thymine (T), cytosine (C) and guanine (G). The programmability of DNA molecules originates from highly-specific Watson-Crick base-pairing interactions, namely A binds to T by forming two hydrogen bonds and C binds to G by forming three hydrogen bonds. Thus, when two DNA strands have complementary sequences, a duplex with a helix structure will form under right conditions. This process is reversible, double stranded DNA (dsDNA) can be denatured into two single-stranded DNA (ssDNA) typically by heating or exposure to high pH. Because G-C pairing is stronger than A-T pairing, dsDNA with more G-C pairings are more stable against heating and pH[125]. Structurally, dsDNA has a width of about 2 nm, with a base separation of 0.34 nm and helical periodicity of 3.5 nm per turn.

Beyond its traditional role in biology as genetic information carrier, DNA is emerging as a unique building material at the nanoscale. This led to the birth of DNA nanotechnology. SsDNA is very flexible with a persistence length of 0.7 nm, however, dsDNA has a persistence length of about 50 nm. Thus, the rigidity and flexibility of DNA can be easily tailored[126]. Programmable structure design can be performed by controlling the rigidity and flexibility by a combination of ssDNA and dsDNA. For example, the rigid dsDNA can be linked by relatively flexible ssDNA strands to form stable motifs. DNA can be made even more rigid by forming double-crossover (DX) tiles[127, 128], triplecrossover (TX) tiles[129], and paranemic-crossover (PX) tiles[130]. Indeed, structural DNA design has been established with aid of computer program. In particular, 'DNA origami' [131] can

## Chapter 2

be designed by folding hundreds of short staple strands into almost arbitrary microscale topological 2D and 3D shapes[132].

Apart from the structural design, a rich toolkits are available for precise manipulation and modification of DNA. For example, replication of DNA can be achieved via the polymerase chain reaction, an amplification technology that exponentially increases the amount of a specific DNA sequence. DNA strands can be cut at desire sites by using endonucleases function and exonucleases function. By using other enzymes, covalent connection, elongation and degradation of DNA can all be achieved.

Combination of novel properties of nanomaterials and unique properties of DNA provides an exciting route to design multifunctional self-assembled materials for various applications[133]. This requires precise synthetic strategy to make DNA-nanoparticle conjugates as well as development of highly-ordered assemblies. Various approaches synthesis DNA-capped nanoparticles.

Synthesis of DNA-capped nanoparticles dates back to the pioneering work reported by Alivisatos and Mirkin in 1996. However, the fundamental synthesis methods for the basic building blocks are notably different: the former focus on mono-DNA conjugate, whereas the later focus on multi-DNA conjugate. As reported by Alivisatos and co-workers, the assembly of spatially defined dimer and trimer structures was mainly conducted by mono-conjugation with careful rational design and substantial purification techniques [23]. In this method, sulphydryl terminated ssDNA was coupled with an excess of monomaleimido functionalized gold nanoparticles. Although mono-conjugates can be produced in this process, the yield is generally very low (<30%). Further purification of the

## Chapter 2

DNA-AuNPs conjugates by gel electrophoresis or HPLC is required. Hence, the mobility of DNA-AuNPs conjugates was thoroughly studied by analysing critical role of the surface charge of nanoparticles[134]. It was found that the properties of particle dominated the electrophoretic mobility, and well-defined conjugates (1-5 DNA ligands per nanoparticle) can be achieved by gel electrophoresis [135]. In addition, the length of DNA stand and size of nanoparticles can also affect mobility.

Multiple DNA strands could be attached to specific sites on nanoparticle surfaces, leading to the formation of site-specific DNA-nanoparticle conjugates. Such conjugates are more likely to be used as functional building blocks to construct anisotropic nano-assemblies such as satellite, cat paw, and dendrimer-like heterostructures. In one example, the asymmetric DNA-AuNPs conjugation was achieved by using magnetic microparticles as geometric restriction templates[136]. In this method, the microparticle facilitated the separation and purification of the anisotropically functionalized nanoparticles. In addition, site-specific DNA-nanoparticle conjugates can also be formed by utilizing a solid support with a stepwise surface-encoding strategy[137]. This method proved higher efficiency and yield of dimers than the conventional solution-based reactions. Through repeated assembly and disassembly at surface, well-defined dimer clusters and Janus nanoparticles could be generated remarkably high yields (70-83%).

DNA strands can also be attached in a site-specific manner to gold nanorods. For the original gold nanorods, cetyltrimethylammonium bromide (CTAB) molecules is preferentially bound on the sides rather than to the ends of the

## Chapter 2

nanorods[138]. Consequently, thiolated DNA are more likely to attach exclusively to the ends of nanorods where CTAB concentrations are low. Apart from the mono-conjugation and site-specific conjugation, multiple DNA strands can be covalently attached to a single nanoparticle, which can be termed as multi-DNA conjugates. The synthesis of multi-DNA conjugates require rational design the DNA sequences, ligand density, ionic strength, and hybridization temperatures [139].

### 2.3.4. Fluorescent Dyes and Others

Apart from the above mentioned functionalization, nanoparticles have also been functionalized with other groups, like fluorescent dyes. This fluorescent modified conjugates used for energy transfer and labelling of non-fluorescent particles. Normally, the fluorescent dyes quenched by the gold nanoparticles via resonant energy and/or electron transfer processes[140]. The quenching is resulted from not only by an increased non-radiative rate but by a sharp decrease in the dye's radiative rate. The change of the radiative and non-radiative molecular decay rates with distance is determined using time-resolved photoluminescence spectroscopy. Remarkably, the distance dependent quantum efficiency is almost exclusively governed by the radiative rate. [141].

### 2.4 Self-Assembly of Plasmonic Nanoparticles

The plasmonic property of nanoparticles can be controlled by the achievement of tuning the size and shape of nanoparticles. The precise and order arrangement of nanoparticles is a new attention field to exploit interesting and potentially useful plasmonic coupling properties. In the particular case of gold nanoparticles, assemblies display collective plasmon resonances resulting from

## Chapter 2

plasmon coupling that gives rise to intense and highly localized electromagnetic fields. It is expected that the ability to assemble these elementary nanoparticles into well-defined assemblies such as “artificial molecules”, “artificial polymers” or “supercrystals” will further impact the way materials are synthesized and devices are fabricated. This part focuses on the gold nanoparticle assembly because the gold nanoparticles own the many benefits, such as high chemical stability, facile surface functionalization and available kinds of shape. The following review is according to the assembly strategies divided by the types of functionalised nanoparticles to cause the nanoparticle assembly.

### 2.4.1 Chemical Directed Self-Assembly

Chemically directed assembly is the most common and powerful strategy for the nanoparticles assembly. The surface modified building block with the specific ability to govern the balance of repulsive and attractive force between interparticles. So the assemblies would be more complexities and with more functions and flexibilities. The functionalized molecules can not only be used as surface stabilizer of nanoparticles, but also introduce anisotropy, directionality and complexity to the system.

The interaction force including repulsive and attractive forces enable to the building block to close enough to packing in the self-assembly process. Attractive force driving the nanoparticles assembly include electrostatic attraction, hydrogen or covalent bonding, depletion force or dipole-dipole interaction. The noble nanoparticle surface modified with small molecules with opposite charges formed of binary supercrystals of AuNPs and AgNPs (Figure 2.8) [142]. The size of two particles is similar around 5 nm. AuNPs surface modified with negatively

## Chapter 2

charged 11-mercaptoundecanoic acid (MUA) and AgNPs surface modified with positively charged Tetramethylammonium chloride (TMA). After two kinds of opposite charges nanoparticles mixed together, non-dense packing and diamond-like sphalerite supercrystals were formed and in which each nanoparticles surround by four another kind particles. Supercrystals were assembly by screening charge of electrostatic between two kinds of opposite particles. An extension of this method is that assembled charged nanoparticles act as the surfactants, and adsorbed onto the crystals' surface to form microcrystals[143].

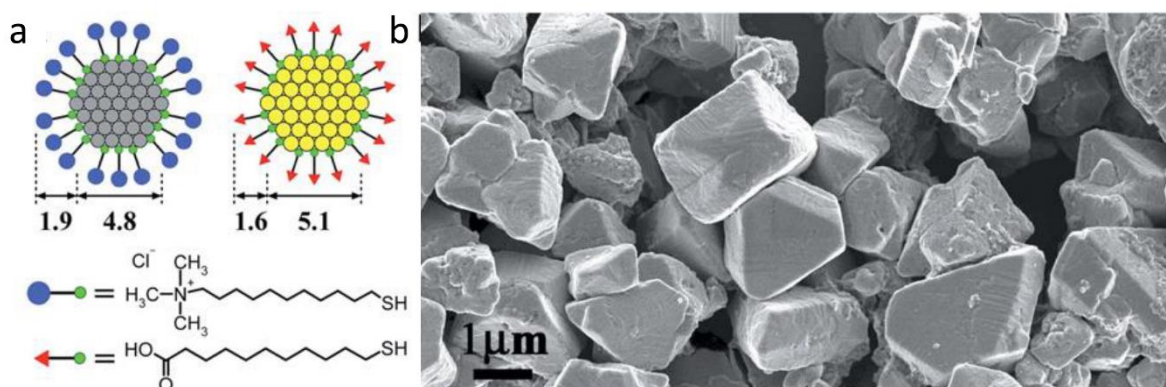


Figure 2.8 (a) Scheme and average dimensions (in nm) of AuMUA and AgTMA nanoparticles used as the model system. (b) Large-area SEM image of binary crystals obtained from AuMUA/AgTMA precipitates. © (2006) American Association for the Advancement of Science.

The interparticles repulsive force can be controlled by modulating ambient conditions, such as the solvent polarity, temperature and pH. In this case, the nanoparticles assembly can be achieved by modification with polymer and reversible hydrogen bonding between polymer and gold nanoparticles. The gold nanoparticles are fully functionalised with triphenylenes that is a class of organic

## Chapter 2

molecules and can form liquid crystals. The gold nanoparticles the self-assembled structure could be controlled either form spaced hexagonal or one-dimensional nanochain just by altering the ratio of methanol to toluene in the solvent[144]. Hydrophobic effects can be used to produce one-dimensional arrays and two dimensional superlattices. Gold nanoparticles are coated with amphiphilic block copolymers, in a mixture of water/tetrahydrofuran, amphiphilic gold nanoparticles assembled into various superstructures, including unimolecular micelles, clusters and vesicles, depending on the lengths of polymer tethers and the sizes of gold nanoparticle cores [145].

### 2.4.2 DNA Direct Assembly

#### 2.4.2.1 Assemblies through DNA Hybridization

Highly-specific Watson-Crick base-pairing forces allow for programming materials synthesis at the nanoscale. Mono-DNA-conjugated nanoparticles have opened a powerful pathway to heterodimeric and heterotrimeric nanostructures[146]. By carefully designing of the complementary ssDNA sequences, the relative spatial arrangement of AuNPs could be controlled through Watson-Crick base-pairing interactions. The product was generally needed to be purified using gel electrophoresis to improve the yield.

Multi-component nanoassemblies could also be constructed by the hybridization strategy. For example, high-yield fabrication for ultra-sensitive SERS-active Au-Ag core-shell nanodumbbells was obtained, and the interparticle spacing were able to be controlled [147]. In conjunction with polymerase chain reaction (PCR), structurally complex assemblies could be obtained by adjusting the density of

## Chapter 2

primer DNA molecules on the nanoparticle surface and the number of PCR cycles [148].

Multi-DNA conjugated nanoparticles can be used to construct three-dimensional super-assemblies [30, 31]. The DNA sequences substantially affected the crystallization process, leading to different lattice structures including face-centred-cubic or body-centred-cubic crystal structures as revealed by Synchrotron-based small angle X-ray scattering (SAXS). This clearly indicates synthetically programmable colloidal crystallization is possible. Temperature programming played a critical role in forming highly-ordered 3D assemblies and the crystalline assemblies formed reversibly during heating and cooling cycles as revealed by SAXS studies. Furthermore, basic design rules were formulated in guiding the design of DNA-programmed nanoparticle assembly, which can predict crystallographic symmetry, and interparticle distances [149, 150]. Remarkably, by applying hollow DNA nanostructures as 3D spacer, voids could be selectively placed into a lattice structure. This led to a diverse lattice structures such as AB<sub>2</sub> type, simple hexagonal, graphite type, AB<sub>6</sub> type, 'lattice X' [151]. This includes the lattice not existing in nature.

Due to the structural plasticity of DNA and the reversibility of their conjugations, a distance-dependent plasmonic response[152], and in situ conformational changes using molecular stimuli could be achieved[153]. Specifically, controllable switching of interparticle distances (in the range of 15-25%) can be realized by using a reconfigurable DNA device that acts as an interparticle linkage[24].

## Chapter 2

Besides the synthetically tuneable length and programmable properties of DNA, the shapes of nanoparticle also strongly influenced the crystallization of DNA-capped nanoparticles. By using anisotropic building blocks, multi-dimensional assemblies including 1D lamellar assemblies of gold nanoprisms, 2D assemblies of vertical-aligned gold nanorods and 3D crystals of gold rhombic dodecahedra can be constructed[29]. These structures were not observed with spherical particles, which provides fundamental insights into shape-dependent DNA hybridization effects on the superlattice dimensionality, crystallographic symmetry and phase behaviour.

### 2.4.2.2 Assemblies through Dry-DNA-Ligand Mediation

Using Watson-Crick base pairing to program materials synthesis is a major research activity. However, the use of DNA strands can go beyond specific hybridization. In a different route, DNA has been used in a drying-mediated self-assembly process to guide the assembly of free-standing monolayered DNA-nanoparticle superlattice membranes (Figure 2.9)[154]. Such free-standing structures have not been achieved with base-pairing-based strategy. This process involved the spatial confinement of a holey substrate fabricated by top-down lithography and highly-ordered nanoparticle arrays formed under unusually low ionic strength without the requirement of specific Watson-Crick base-pairing. Compared to alkyl ligands, molecular lengths of DNA ligands can be controlled over a much large size regime, enabling tailoring of both structural (inter-particle spacing) and functional properties (plasmonic and mechanical) over a wide window. Remarkably, these plasmonic coupling properties were not easily achieved with base-pairing-based strategy in which particle-to-particle spacing is generally too large and ordered domains are limited to small area.

## Chapter 2

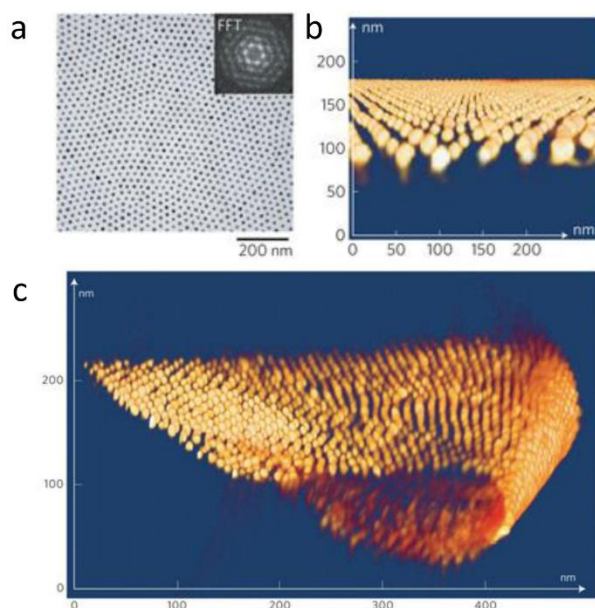


Figure 2.9 DNA as entropic ligands in drying-mediated self-assembly. © (2009) Rights Managed by Nature Publishing Group.

Dry DNA ligand-based approach can be combined with top-down lithography to obtain nanoscale structures with micrometer-sized moulds [155]. In addition, this combined top-down and bottom-up strategy is able to rationally control over the local nucleation and growth of the nanoparticle superlattices, leading to a versatile structures with high degrees of internal order, such as single particle-width corrals, single particle-thickness microdiscs and submicrometre-sized ‘supra-crystals’. Notably, these patterned superlattices can be addressed by micropatterned electrode arrays, suggesting potential applications in bottom-up nanodevices.

Different from the base-pairing forces driving the crystallization of DNA-capped nanoparticles, the drying-mediated crystallization of DNA-capped nanoparticles is entropy driven [32]. During water evaporation, the forces exerted on the DNA

## Chapter 2

corona gradually increase and resulted in a smooth and uniform deformation of the DNA corona. By synchrotron-based SAXS, a general entropic spring model for the drying-mediated crystallization of DNA-capped nanoparticles was established. In addition, the crystallization time in the soft-crystallization process is programmable by taking advantage of the fine and wide tunability of DNA length. In an extended fundamental study, the crystalline Gibbs monolayers of DNA-capped nanoparticle were found to form at the air/water interface[156]. The spatial crystallization was characterized by grazing-incidence SAXS in specific configurations, and predicted the interparticle spacing programmability by adjusting both ionic strength and DNA sequence length.

### 2.4.2.3 Assemblies through DNA Template

The emerging structural DNA nanotechnology provides a rich toolkit on synthesizing rigid DNA structures, such as DNA tiles/frames, and origami, which can be used to template the assembly of nanoparticles. Generally speaking, the design is based on the following two steps: (1) design the DNA tiles/origami with capture strands at predetermined locations; (2) hybridization of DNA-capped nanoparticles with capture strands at the designed sites[157]. As an example, 3D tubular assemblies of gold nanoparticles including stacked rings, single spirals, double spirals, and nested spiral tubes have been achieved with DNA tile-templated self-assembly[158]. The different conformations of tubular structure and chiralities could be controlled by size-dependent steric repulsions among nanoparticles. Four different DNA double-crossover tiles have been used to template the DNA-modified nanoparticles into closely packed rows with precisely defined regular inter-row spacing [159]. By using the similar method, 2D periodic pattern and rhombic lattice arrangement were realized[160].

## Chapter 2

By careful sequence design of DNA geometries, various nonlinear structures could form and were used to control the placement of nanoparticles. In particular, pyramidal plasmonic assemblies were reported [161], in which the tetrahedral symmetry of DNA pyramids enabled the formation of chiral nanostructures with four different sized nanoparticle at each tip. Gel electrophoresis purification was used to separate the pyramids and further confirmed by transmission electron microscope (TEM).

Unlike interweaving various DNA chains into a rigid scaffold, dynamic DNA templates can be created with functional single-stranded and cyclic form[162]. This template guided the selective attachment of mono-DNA conjugated nanoparticles with different diameters on the complementary arms of DNA templates. Interestingly, post-assembly named 'write/erase' method is shown by selectively removing one particle from triangles of three AuNPs clusters, followed by replacement of another nanoparticles onto the specific site.

By using DNA origami folding technique[132] or rationally designed DNA geometries[163], more complex nanostructures could be obtained. DNA origami has attracted much attention to the field of DNA nanotechnology since the landmark work established by Rothemund[131]. Different from the conventional crossover strategy that using single building blocks to construct larger structures in a 'two-step' process, DNA origami provides a versatile and simple 'one-pot' method to create fully addressable DNA nanostructures by using short staple DNA strands to fold a single-stranded genomic DNA into geometrically desired nanopatterns[157]. Multiple clusters and Ag-Au heterodimers have been obtained by DNA origami templated assembly [157]. More complex structures

## Chapter 2

such as helical plasmonic assemblies could be obtained from origami method. Apart from symmetrical spheres, positioning of gold nanorods was also achieved forming discrete, well-ordered assemblies.

The assembly property of DNA-capped nanoparticles could be combined with top-down lithography. The versatile method for integrating top-down lithography with bottom-up DNA-programmed self-assembly is a potential future nanofabrication strategy for plasmonic circuitry, data storage, diagnostic assays, and optoelectronics[155]. Various lithographic techniques are proved to be efficient in patterning and depositing plasmonic nanocrystals on DNA-functionalized surfaces [51, 156-158], also including patterning of DNA tiles and origami as templates to guide the assembly of plasmonic nanocrystals. In a typical method, repeated patterning of large-area arrays of ssDNA-capped gold nanoparticle was achieved by a soft-lithographic subtraction printing process[159]. Spatially ordered 2D arrays were constructed by large-area patterning of DNA-capped nanoparticles through the site-selective deposition of triangular DNA origami onto lithographically patterned substrates[160]. Precise binding of AuNPs to each DNA structure was achieved and formed macroscopic arrays with characteristic length scales ranging from a few to several hundreds of nanometers. In addition, different patterns, such as multiple triangles with alternating left and right orientations, was also formed and suggested a new way to rationally create not just periodic arrays but complex networks[161].

### 2.4.3 Template Assisted Self-Assembly

The above introduced strategies are based on the bottom up techniques. The primary limitation of bottom up methods is precisely control the nanoparticles

## Chapter 2

position on a surface at the nanoscale. This issue can be managed by the combination of the top down fabrication techniques. The combination can magnify the advantages of these two techniques and reach the high level of fabrication control.

Top-down strategy can fabricate the template with defined geometrical structure. The template with geometrical structure has the ability to confine the nanoparticles precisely into uniform aggregates with well-controlled sizes, shapes, and structures. When colloidal particles dewet from a surface that had been patterned with appropriate structures, the particles are trapped by the recessed regions and assembled into aggregates whose structures were depend on the geometric confinement provided by the templates. Single gold particles are selectively assembled by lithographically defined template according to nanoparticles shape and size, over several micrometers, using microcontact printing to transfer the particle monolayer onto a substrate of interest. What is more, templates allow to immobilize dimers control over particle orientation within pair structures by capillary force [162]. Another example is assembled monodispersed spherical colloids into complex, zigzag aggregates with well-defined internal structures and tightly controlled lengths by the combination of liquid dewetting, physical confinement, and attractive capillary forces[163]. This method enable to produce a rich variety of polygonal, polyhedral, spiral and hybrid aggregates. The structure of aggregates could be controlled by changing the shape and dimension of the template[164].

The above examples obtain assembles nanoparticles trapped in the patterned substrates, next assembles are transfer from the templates or remove template.

## Chapter 2

3D patterns of micro and nanoparticle assembly via evaporative self-assembly based on the coffee-ring effect of an evaporating suspension. The building block of assemblies varies size of microparticles (Silica), metal oxide nanoparticles ( $\text{TiO}_2$ ,  $\text{ZnO}$ ), and metallic nanoparticles (Ag) [165]. More complex assemblies structure can be formed assisted by template. A new template-assisted method based on the stamping of colloidal particles for the large-area fabrication of organized pyramidal supercrystal periodical arrays[166]. The assembly films can be transferred to many surfaces, including glass, silicon wafers, and double-sided tape.

Expect the nanoparticles can be trapped the pattern silicon templates, the nanoparticles are also can assembly onto non-patterned silicon substrates by the assisted patterned PDMS substrates. Densely packed arrays of gold nanoparticles assembly in PDMS templates in lines. Then template as printing plate transfer the assembled nanoparticles onto a non-patterned silicon substrate[167]. Later, hierarchical self-assembly of gold nanoparticles are achieved by an elastomeric template made of PDMS displaying arrays of micron-sized cavities that help to regulate the evaporation[168]. the self-assembly of a variety of building blocks into crystalline superstructures takes place upon solvent evaporation, and their precise placement over millimeter scale areas is induced by confinement of the colloidal suspension in micron-sized cavities. It can be obtained a high control over assemblies morphology and tuned the topography of the patterned substrate with the millimeter scale. In this way the pattern can be reusable.

## Chapter 2

### 2.5 References

1. Tan, S.J., et al., *Building plasmonic nanostructures with DNA*. Nat Nano, 2011. **6**(5): p. 268-276.
2. Schuller, J.A., et al., *Plasmonics for extreme light concentration and manipulation*. Nat Mater, 2010. **9**(3): p. 193-204.
3. Shipway, A.N., E. Katz, and I. Willner, *Nanoparticle Arrays on Surfaces for Electronic, Optical, and Sensor Applications*. ChemPhysChem, 2000. **1**(1): p. 18-52.
4. Ozbay, E., *Plasmonics: Merging Photonics and Electronics at Nanoscale Dimensions*. Science, 2006. **311**(5758): p. 189-193.
5. Anker, J.N., et al., *Biosensing with plasmonic nanosensors*. Nat Mater, 2008. **7**(6): p. 442-453.
6. Maier, S.A., et al., *Local detection of electromagnetic energy transport below the diffraction limit in metal nanoparticle plasmon waveguides*. Nat Mater, 2003. **2**(4): p. 229-232.
7. Lal, S., S.E. Clare, and N.J. Halas, *Nanoshell-Enabled Photothermal Cancer Therapy: Impending Clinical Impact*. Accounts of Chemical Research, 2008. **41**(12): p. 1842-1851.
8. Yavuz, M.S., et al., *Gold nanocages covered by smart polymers for controlled release with near-infrared light*. Nat Mater, 2009. **8**(12): p. 935-939.
9. Alivisatos, A.P., et al., *Organization of 'nanocrystal molecules' using DNA*. Nature, 1996. **382**(6592): p. 609-611.
10. Maye, M.M., et al., *Switching binary states of nanoparticle superlattices and dimer clusters by DNA strands*. Nature Nanotechnol., 2010. **5**: p. 116-120.
11. Nie, Z., et al., *Self-assembly of metal-polymer analogues of amphiphilic triblock copolymers*. Nature Materials, 2007. **6**(8): p. 609-14.
12. Liu, K., et al., *Step-growth polymerization of inorganic nanoparticles*. Science, 2010. **329**(5988): p. 197-200.
13. Pileni, M.-P., *Self-assembly of inorganic nanocrystals: fabrication and collective intrinsic properties*. Accounts of Chemical Research, 2007. **40**(8): p. 685-693.

## Chapter 2

14. Heitsch, A.T., et al., *GISAXS characterization of order in hexagonal monolayers of FePt nanocrystals*. J. Phys. Chem. C, 2010. **114**(34): p. 14427-14432.
15. Jones, M.R., et al., *DNA-nanoparticle superlattices formed from anisotropic building blocks*. Nat Mater, 2010. **9**(11): p. 913-917.
16. Park, S.Y., et al., *DNA-programmable nanoparticle crystallization*. Nature, 2008. **451**: p. 553-556.
17. Nykypanchuk, D., et al., *DNA-guided crystallization of colloidal nanoparticles*. Nature, 2008. **451**: p. 549-552.
18. Cheng, W.L., et al., *Probing in real time the soft crystallization of DNA-capped nanoparticles*. Angewandte Chemie International Edition, 2010. **49**: p. 380-384.
19. Willets, K.A. and R.P. Van Duyne, *Localized surface plasmon resonance spectroscopy and sensing*. Annu. Rev. Phys. Chem., 2007. **58**: p. 267-297.
20. Liz-Marzán, L.M., *Tailoring Surface Plasmons through the Morphology and Assembly of Metal Nanoparticles*. Langmuir, 2005. **22**(1): p. 32-41.
21. Kelly, K.L., et al., *The Optical Properties of Metal Nanoparticles: The Influence of Size, Shape, and Dielectric Environment*. The Journal of Physical Chemistry B, 2002. **107**(3): p. 668-677.
22. Mulvaney, P., *Surface Plasmon Spectroscopy of Nanosized Metal Particles*. Langmuir, 1996. **12**(3): p. 788-800.
23. Mie, G., *Beiträge zur Optik trüber Medien, speziell kolloidaler Metallösungen*. Ann. Phys., 1908. **330**(3): p. 377-445.
24. Link, S. and M.A. El-Sayed, *Size and Temperature Dependence of the Plasmon Absorption of Colloidal Gold Nanoparticles*. The Journal of Physical Chemistry B, 1999. **103**(21): p. 4212-4217.
25. Zhang, J. and C. Noguez, *Plasmonic Optical Properties and Applications of Metal Nanostructures*. Plasmonics, 2008. **3**(4): p. 127-150.
26. Purcell, E.M. and C.R. Pennypacker, *Scattering and absorption of light by nonspherical dielectric grains*. The Astrophysical Journal, 1973. **186**: p. 705-714.

## Chapter 2

27. Wiley, B.J., et al., *Maneuvering the Surface Plasmon Resonance of Silver Nanostructures through Shape-Controlled Synthesis*. The Journal of Physical Chemistry B, 2006. **110**(32): p. 15666-15675.
28. Javier, A. and W.B. Garnett, *Coupling in Metallic Nanoparticles*, in *Handbook of Nanophysics*. 2010, CRC Press. p. 1-18.
29. Jain, P.K., W. Huang, and M.A. El-Sayed, *On the Universal Scaling Behavior of the Distance Decay of Plasmon Coupling in Metal Nanoparticle Pairs: A Plasmon Ruler Equation*. Nano Letters, 2007. **7**(7): p. 2080-2088.
30. Lal, S., S. Link, and N.J. Halas, *Nano-optics from sensing to waveguiding*. Nat Photon, 2007. **1**(11): p. 641-648.
31. Le Ru, E. and P. Etchegoin, *Principles of Surface-Enhanced Raman Spectroscopy: and related plasmonic effects*. 2008: Elsevier.
32. Moskovits, M., *Surface-enhanced Raman spectroscopy: a brief retrospective*. Journal of Raman Spectroscopy, 2005. **36**(6-7): p. 485-496.
33. Weaver, M.J., S. Zou, and H.Y.H. Chan, *Peer Reviewed: The New Interfacial Ubiquity of Surface-Enhanced Raman Spectroscopy*. Analytical Chemistry, 2000. **72**(1): p. 38 A-47 A.
34. Otto, A., *Surface-enhanced Raman scattering: "Classical" and "Chemical" origins*, in *Light Scattering in Solids IV*, M. Cardona and G. Güntherodt, Editors. 1984, Springer Berlin Heidelberg. p. 289-418.
35. Champion, A. and P. Kambhampati, *Surface-enhanced Raman scattering*. Chemical Society Reviews, 1998. **27**(4): p. 241-250.
36. Kneipp, J., H. Kneipp, and K. Kneipp, *SERS-a single-molecule and nanoscale tool for bioanalytics*. Chemical Society Reviews, 2008. **37**(5): p. 1052-1060.
37. Stockman, M.I., et al., *Enhanced Raman scattering by fractal clusters: Scale-invariant theory*. Physical Review B, 1992. **46**(5): p. 2821-2830.
38. Schatz, G., M. Young, and R. Van Duyne, *Electromagnetic Mechanism of SERS*, in *Surface-Enhanced Raman Scattering*, K. Kneipp, M. Moskovits, and H. Kneipp, Editors. 2006, Springer Berlin Heidelberg. p. 19-45.
39. Rycenga, M., et al., *Generation of Hot Spots with Silver Nanocubes for Single-Molecule Detection by Surface-Enhanced Raman Scattering*. Angewandte Chemie, 2011. **123**(24): p. 5587-5591.

## Chapter 2

40. Cialla, D., et al., *Surface-enhanced Raman spectroscopy (SERS): progress and trends*. Analytical and Bioanalytical Chemistry, 2012. **403**(1): p. 27-54.
41. Lim, D.K., et al., *Nanogap-engineerable Raman-active nanodumbbells for single-molecule detection*. Nature Materials, 2010. **9**(1): p. 60-67.
42. Biswas, A., et al., *Advances in top-down and bottom-up surface nanofabrication: Techniques, applications & future prospects*. Advances in Colloid and Interface Science, 2012. **170**(1-2): p. 2-27.
43. Mailly, D., *Nanofabrication techniques*. The European Physical Journal Special Topics, 2009. **172**(1): p. 333-342.
44. Yaman, M., et al., *Arrays of indefinitely long uniform nanowires and nanotubes*. Nat Mater, 2011. **10**(7): p. 494-501.
45. Liddle, J.A. and G.M. Gallatin, *Lithography, metrology and nanomanufacturing*. Nanoscale, 2011. **3**(7): p. 2679-2688.
46. Stewart, M.E., et al., *Unconventional methods for forming nanopatterns*. Proceedings of the Institution of Mechanical Engineers, Part N: Journal of Nanoengineering and Nanosystems, 2006. **220**(3): p. 81-138.
47. Abu Hatab, N.A., J.M. Oran, and M.J. Sepaniak, *Surface-Enhanced Raman Spectroscopy Substrates Created via Electron Beam Lithography and Nanotransfer Printing*. ACS Nano, 2008. **2**(2): p. 377-385.
48. Gates, B.D., et al., *New approaches to nanofabrication: molding, printing, and other techniques*. Chemical reviews, 2005. **105**(4): p. 1171-1196.
49. Chen, Y. and A. Pepin, *Nanofabrication: Conventional and nonconventional methods*. Electrophoresis, 2001. **22**(2): p. 187-207.
50. Dammel, R., *Diazonaphthoquinone-based Resists (Tutorial Texts in Optical Engineering Vol. TT11)(Tutorial Texts in Optical Engineering, Vol Tt 11)*. 1993.
51. Gates, B.D., et al., *New Approaches to Nanofabrication: Molding, Printing, and Other Techniques*. Chemical Reviews, 2005. **105**(4): p. 1171-1196.
52. Hashioka, S., et al., *Metal nanogap devices fabricated by conventional photolithography and their application to deoxyribose nucleic acid analysis*. Journal of Vacuum Science & Technology B, 2003. **21**(6): p. 2937-2940.

## Chapter 2

53. Brunner, T.A., *Why optical lithography will live forever*. Journal of Vacuum Science & Technology B, 2003. **21**(6): p. 2632-2637.
54. Ito, T. and S. Okazaki, *Pushing the limits of lithography*. Nature, 2000. **406**(6799): p. 1027-1031.
55. Silverman, P.J., *Extreme ultraviolet lithography: overview and development status*. Journal of Micro/Nanolithography, MEMS, and MOEMS, 2005. **4**(1): p. 011006-011006-5.
56. Nalwa, H.S., *Handbook of Nanostructured Materials and Nanotechnology, Five-Volume Set*. Vol. 3. 1999: Academic Press.
57. Xia, Y. and G.M. Whitesides, *Soft lithography*. Annual review of materials science, 1998. **28**(1): p. 153-184.
58. Biswas, A., et al., *Advances in top-down and bottom-up surface nanofabrication: Techniques, applications & future prospects*. Advances in Colloid and Interface Science, 2012. **170**(1): p. 2-27.
59. Grzelczak, M., et al., *Shape control in gold nanoparticle synthesis*. Chemical Society Reviews, 2008. **37**(9): p. 1783-1791.
60. Xia, Y., et al., *Shape-Controlled Synthesis of Metal Nanocrystals: Simple Chemistry Meets Complex Physics?* Angewandte Chemie International Edition, 2009. **48**(1): p. 60-103.
61. Frens, G., *Controlled Nucleation for the Regulation of the Particle Size in Monodisperse Gold Suspensions*. Nature, Phys. Sci., 1973. **241**: p. 20.
62. Turkevich, J., P.C. Stevenson, and J. Hillier, *A study of the nucleation and growth processes in the synthesis of colloidal gold*. Discussions of the Faraday Society, 1951. **11**(0): p. 55-75.
63. Peng, X., J. Wickham, and A. Alivisatos, *Kinetics of II-VI and III-V colloidal semiconductor nanocrystal growth: "focusing" of size distributions*. Journal of the American Chemical Society, 1998. **120**(21): p. 5343-5344.
64. Jana, N.R., L. Gearheart, and C.J. Murphy, *Seeding Growth for Size Control of 5–40 nm Diameter Gold Nanoparticles*. Langmuir, 2001. **17**(22): p. 6782-6786.
65. Perrault, S.D. and W.C.W. Chan, *Synthesis and Surface Modification of Highly Monodispersed, Spherical Gold Nanoparticles of 50–200 nm*. Journal of the American Chemical Society, 2009. **131**(47): p. 17042-17043.

## Chapter 2

66. Nikoobakht, B. and M.A. El-Sayed, *Preparation and Growth Mechanism of Gold Nanorods (NRs) Using Seed-Mediated Growth Method*. Chemistry of Materials, 2003. **15**(10): p. 1957-1962.
67. Busbee, B.D., S.O. Obare, and C.J. Murphy, *An Improved Synthesis of High-Aspect-Ratio Gold Nanorods*. Advanced Materials, 2003. **15**(5): p. 414-416.
68. Millstone, J.E., et al., *Observation of a Quadrupole Plasmon Mode for a Colloidal Solution of Gold Nanoprisms*. Journal of the American Chemical Society, 2005. **127**(15): p. 5312-5313.
69. Kumar, C.S.S.R., *Biofunctionalization of nanomaterials*. 2005, Weinheim: Wiley-VCH.
70. Turkevich, J., G. Garton, and P. Stevenson, *The color of colloidal gold*. Journal of colloid Science, 1954. **9**: p. 26-35.
71. Kimling, J., et al., *Turkevich Method for Gold Nanoparticle Synthesis Revisited*. The Journal of Physical Chemistry B, 2006. **110**(32): p. 15700-15707.
72. Ji, X., et al., *Size control of gold nanocrystals in citrate reduction: the third role of citrate*. Journal of the American Chemical Society, 2007. **129**(45): p. 13939-13948.
73. Liao, H. and J.H. Hafner, *Gold Nanorod Bioconjugates*. Chemistry of Materials, 2005. **17**(18): p. 4636-4641.
74. Betty, C.R.-K., et al., *The stabilization and targeting of surfactant-synthesized gold nanorods*. Nanotechnology, 2009. **20**(43): p. 434005.
75. Oh, E., et al., *One-Phase Synthesis of Water-Soluble Gold Nanoparticles with Control over Size and Surface Functionalities*. Langmuir, 2010. **26**(10): p. 7604-7613.
76. Tracy, J.B., et al., *Poly(ethylene glycol) Ligands for High-Resolution Nanoparticle Mass Spectrometry*. Journal of the American Chemical Society, 2007. **129**(21): p. 6706-6707.
77. MacLeod, M.J. and J.A. Johnson, *PEGylated N-Heterocyclic Carbene Anchors Designed To Stabilize Gold Nanoparticles in Biologically Relevant Media*. Journal of the American Chemical Society, 2015. **137**(25): p. 7974-7977.

## Chapter 2

78. Meguro, K., et al., *The Preparation of Colloidal Precious Metal Particles Using Copolymers of Vinyl Alcohol-*N*-Vinylpyrrolidone*. Bulletin of the Chemical Society of Japan, 1988. **61**(2): p. 347-350.
79. Seoudi, R., A.A. Fouda, and D.A. Elmenshawy, *Synthesis, characterization and vibrational spectroscopic studies of different particle size of gold nanoparticle capped with polyvinylpyrrolidone*. Physica B: Condensed Matter, 2010. **405**(3): p. 906-911.
80. Li, D., et al., *Fabrication of pH-Responsive Nanocomposites of Gold Nanoparticles/Poly(4-vinylpyridine)*. Chemistry of Materials, 2007. **19**(3): p. 412-417.
81. Kim, K., H. Ryoo, and K.S. Shin, *Adsorption and Aggregation Characteristics of Silver Nanoparticles onto a Poly(4-vinylpyridine) Film: A Comparison with Gold Nanoparticles*. Langmuir, 2010. **26**(13): p. 10827-10832.
82. Mbhele, Z.H., et al., *Fabrication and Characterization of Silver-Polyvinyl Alcohol Nanocomposites*. Chemistry of Materials, 2003. **15**(26): p. 5019-5024.
83. PØrez-Juste, J., et al., *Optical Control and Patterning of Gold-Nanorod±Poly (vinyl alcohol) Nanocomposite Films\**. polymer, 2005. **21**: p. 22.
84. Bhattacharjee, R.R., M. Chakraborty, and T.K. Mandal, *Reversible Association of Thermoresponsive Gold Nanoparticles: Polyelectrolyte Effect on the Lower Critical Solution Temperature of Poly(vinyl methyl ether)*. The Journal of Physical Chemistry B, 2006. **110**(13): p. 6768-6775.
85. Huang, H. and X. Yang, *Synthesis of Chitosan-Stabilized Gold Nanoparticles in the Absence/Presence of Tripolyphosphate*. Biomacromolecules, 2004. **5**(6): p. 2340-2346.
86. Song, W.J., et al., *Gold nanoparticles capped with polyethyleneimine for enhanced siRNA delivery*. Small, 2010. **6**(2): p. 239-246.
87. Sun, X., S. Dong, and E. Wang, *One-step synthesis and characterization of polyelectrolyte-protected gold nanoparticles through a thermal process*. Polymer, 2004. **45**(7): p. 2181-2184.
88. Chen, H., et al., *One-step preparation and characterization of PDDA-protected gold nanoparticles*. Polymer, 2006. **47**(2): p. 763-766.

## Chapter 2

89. Gole, A. and C.J. Murphy, *Polyelectrolyte-Coated Gold Nanorods: Synthesis, Characterization and Immobilization*. Chemistry of Materials, 2005. **17**(6): p. 1325-1330.
90. Yilmaz, E. and S. Suzer, *Au nanoparticles in PMMA matrix: In situ synthesis and the effect of Au nanoparticles on PMMA conductivity*. Applied Surface Science, 2010. **256**(22): p. 6630-6633.
91. Meli, L. and P.F. Green, *Aggregation and coarsening of ligand-stabilized gold nanoparticles in poly (methyl methacrylate) thin films*. ACS nano, 2008. **2**(6): p. 1305-1312.
92. Shan, J., et al., *Amphiphilic gold nanoparticles grafted with poly (N-isopropylacrylamide) and polystyrene*. Macromolecules, 2005. **38**(7): p. 2918-2926.
93. Shan, J., et al., *Two phase transitions of poly (N-isopropylacrylamide) brushes bound to gold nanoparticles*. Langmuir, 2004. **20**(11): p. 4671-4676.
94. Saha, K., et al., *Gold Nanoparticles in Chemical and Biological Sensing*. Chemical Reviews, 2012. **112**(5): p. 2739-2779.
95. Wuelfing, W.P., et al., *Nanometer Gold Clusters Protected by Surface-Bound Monolayers of Thiolated Poly(ethylene glycol) Polymer Electrolyte*. Journal of the American Chemical Society, 1998. **120**(48): p. 12696-12697.
96. Corbierre, M.K., N.S. Cameron, and R.B. Lennox, *Polymer-Stabilized Gold Nanoparticles with High Grafting Densities*. Langmuir, 2004. **20**(7): p. 2867-2873.
97. Ohno, K., et al., *Synthesis of Gold Nanoparticles Coated with Well-Defined, High-Density Polymer Brushes by Surface-Initiated Living Radical Polymerization*. Macromolecules, 2002. **35**(24): p. 8989-8993.
98. Nuß, S., et al., *Gold nanoparticles with covalently attached polymer chains*. Angewandte Chemie International Edition, 2001. **40**(21): p. 4016-4018.
99. Corbierre, M.K., et al., *Polymer-Stabilized Gold Nanoparticles and Their Incorporation into Polymer Matrices*. Journal of the American Chemical Society, 2001. **123**(42): p. 10411-10412.

## Chapter 2

100. Kang, Y. and T.A. Taton, *Core/shell gold nanoparticles by self-assembly and crosslinking of micellar, block-copolymer shells*. *Angewandte Chemie*, 2005. **117**(3): p. 413-416.
101. Ah, C.S., et al., *Size-Controlled Synthesis of Machinable Single Crystalline Gold Nanoplates*. *Chemistry of Materials*, 2005. **17**(22): p. 5558-5561.
102. Salvati, R., et al., *UV-vis spectroscopy for on-line monitoring of Au nanoparticles size during growth*. *Applied Surface Science*, 2005. **248**(1-4): p. 28-31.
103. Kohler, N., G.E. Fryxell, and M. Zhang, *A bifunctional poly (ethylene glycol) silane immobilized on metallic oxide-based nanoparticles for conjugation with cell targeting agents*. *Journal of the American Chemical Society*, 2004. **126**(23): p. 7206-7211.
104. Otsuka, H., Y. Nagasaki, and K. Kataoka, *PEGylated nanoparticles for biological and pharmaceutical applications*. *Advanced drug delivery reviews*, 2012. **64**: p. 246-255.
105. Oh, E., et al., *Colloidal stability of gold nanoparticles coated with multithiol-poly (ethylene glycol) ligands: importance of structural constraints of the sulfur anchoring groups*. *The Journal of Physical Chemistry C*, 2013. **117**(37): p. 18947-18956.
106. Niidome, T., et al., *PEG-modified gold nanorods with a stealth character for in vivo applications*. *Journal of Controlled Release*, 2006. **114**(3): p. 343-347.
107. Gan, D. and L.A. Lyon, *Synthesis and protein adsorption resistance of PEG-modified poly (N-isopropylacrylamide) core/shell microgels*. *Macromolecules*, 2002. **35**(26): p. 9634-9639.
108. van Vlerken, L.E., T.K. Vyas, and M.M. Amiji, *Poly (ethylene glycol)-modified nanocarriers for tumor-targeted and intracellular delivery*. *Pharmaceutical research*, 2007. **24**(8): p. 1405-1414.
109. Zhang, X.-D., et al., *Size-dependent in vivo toxicity of PEG-coated gold nanoparticles*. *International journal of nanomedicine*, 2011. **6**: p. 2071.
110. Ogris, M., et al., *PEGylated DNA/transferrin-PEI complexes: reduced interaction with blood components, extended circulation in blood and potential for systemic gene delivery*. *Gene therapy*, 1999. **6**(4): p. 595-605.

## Chapter 2

111. Zareie, H.M., et al., *Temperature-responsive self-assembled monolayers of oligo (ethylene glycol): control of biomolecular recognition*. *Acs Nano*, 2008. **2**(4): p. 757-765.
112. Aslan, K., C.C. Luhrs, and V.H. Pérez-Luna, *Controlled and reversible aggregation of biotinylated gold nanoparticles with streptavidin*. *The Journal of Physical Chemistry B*, 2004. **108**(40): p. 15631-15639.
113. Skaff, H. and T. Emrick, *The use of 4-substituted pyridines to afford amphiphilic, pegylated cadmium selenide nanoparticles*. *Chem. Commun.*, 2003(1): p. 52-53.
114. Pinaud, F., et al., *Bioactivation and cell targeting of semiconductor CdSe/ZnS nanocrystals with phytochelatin-related peptides*. *Journal of the American Chemical Society*, 2004. **126**(19): p. 6115-6123.
115. Yang, D., et al., *Novel DNA materials and their applications*. *Wiley Interdisciplinary Reviews: Nanomedicine and Nanobiotechnology*, 2010. **2**(6): p. 648-669.
116. LaBean, T.H. and H. Li, *Constructing novel materials with DNA*. *Nano Today*, 2007. **2**(2): p. 26-35.
117. Winfree, E., et al., *Design and self-assembly of two-dimensional DNA crystals*. *Nature*, 1998. **394**(6693): p. 539-544.
118. Reishus, D., et al., *Self-Assembly of DNA Double-Double Crossover Complexes into High-Density, Doubly Connected, Planar Structures*. *Journal of the American Chemical Society*, 2005. **127**(50): p. 17590-17591.
119. Liu, Y., et al., *Aptamer-Directed Self-Assembly of Protein Arrays on a DNA Nanostructure*. *Angewandte Chemie International Edition*, 2005. **44**(28): p. 4333-4338.
120. Yan, H., et al., *A robust DNA mechanical device controlled by hybridization topology*. *Nature*, 2002. **415**(6867): p. 62-65.
121. Rothmund, P.W.K., *Folding DNA to create nanoscale shapes and patterns*. *Nature*, 2006. **440**(7082): p. 297-302.
122. Han, D., et al., *DNA Origami with Complex Curvatures in Three-Dimensional Space*. *Science*, 2011. **332**(6027): p. 342-346.
123. Luo, D., *The road from biology to materials*. *Materials Today*, 2003. **6**(11): p. 38-43.

## Chapter 2

124. Zanchet, D., et al., *Electrophoretic and Structural Studies of DNA-Directed Au Nanoparticle Groupings*. The Journal of Physical Chemistry B, 2002. **106**(45): p. 11758-11763.
125. Zanchet, D., et al., *Electrophoretic Isolation of Discrete Au Nanocrystal/DNA Conjugates*. Nano Letters, 2000. **1**(1): p. 32-35.
126. Xu, X., et al., *Asymmetric Functionalization of Gold Nanoparticles with Oligonucleotides*. Journal of the American Chemical Society, 2006. **128**(29): p. 9286-9287.
127. Maye, M.M., et al., *Stepwise surface encoding for high-throughput assembly of nanoclusters*. Nat Mater, 2009. **8**(5): p. 388-391.
128. Nie, et al., *"Supramolecular" Assembly of Gold Nanorods End-Terminated with Polymer "Pom-Poms": Effect of Pom-Pom Structure on the Association Modes*. Journal of the American Chemical Society, 2008. **130**(11): p. 3683-3689.
129. Mirkin, C.A., et al., *A DNA-based method for rationally assembling nanoparticles into macroscopic materials*. Nature, 1996. **382**(6592): p. 607-609.
130. Dulkeith, E., et al., *Fluorescence Quenching of Dye Molecules near Gold Nanoparticles: Radiative and Nonradiative Effects*. Physical Review Letters, 2002. **89**(20): p. 203002.
131. Dulkeith, E., et al., *Gold nanoparticles quench fluorescence by phase induced radiative rate suppression*. Nano Letters, 2005. **5**(4): p. 585-589.
132. Kalsin, A.M., et al., *Electrostatic self-assembly of binary nanoparticle crystals with a diamond-like lattice*. Science, 2006. **312**(5772): p. 420-424.
133. Kowalczyk, B., et al., *Charged nanoparticles as supramolecular surfactants for controlling the growth and stability of microcrystals*. Nat Mater, 2012. **11**(3): p. 227-232.
134. Yamada, M., Z. Shen, and M. Miyake, *Self-assembly of discotic liquid crystalline molecule-modified gold nanoparticles: control of 1D and hexagonal ordering induced by solvent polarity*. Chemical Communications, 2006(24): p. 2569-2571.
135. He, J., et al., *Self-Assembly of Amphiphilic Plasmonic Micelle-Like Nanoparticles in Selective Solvents*. Journal of the American Chemical Society, 2013. **135**(21): p. 7974-7984.

## Chapter 2

136. Loweth, C.J., et al., *DNA-Based Assembly of Gold Nanocrystals*. Angewandte Chemie International Edition, 1999. **38**(12): p. 1808-1812.
137. Lim, D.-K., et al., *Nanogap-engineerable Raman-active nanodumbbells for single-molecule detection*. Nat Mater, 2010. **9**(1): p. 60-67.
138. Chen, W., et al., *Nanoparticle Superstructures Made by Polymerase Chain Reaction: Collective Interactions of Nanoparticles and a New Principle for Chiral Materials*. Nano Letters, 2009. **9**(5): p. 2153-2159.
139. Macfarlane, R.J., et al., *Establishing the Design Rules for DNA-Mediated Colloidal Crystallization*. Angewandte Chemie International Edition, 2010. **49**(27): p. 4589-4592.
140. Macfarlane, R.J., et al., *Nanoparticle Superlattice Engineering with DNA*. Science, 2011. **334**(6053): p. 204-208.
141. Auyeung, E., et al., *Synthetically programmable nanoparticle superlattices using a hollow three-dimensional spacer approach*. Nat Nano, 2012. **7**(1): p. 24-28.
142. Sonnichsen, C., et al., *A molecular ruler based on plasmon coupling of single gold and silver nanoparticles*. Nat Biotech, 2005. **23**(6): p. 741-745.
143. Sebba, D., T. LaBean, and A. Lazarides, *Plasmon coupling in binary metal core–satellite assemblies*. Applied Physics B, 2008. **93**(1): p. 69-78.
144. Cheng, W.L., et al., *Free-standing nanoparticle superlattice sheets controlled by DNA*. Nature materials, 2009. **8**(6): p. 519-525.
145. Cheng, W.L., et al., *Nanopatterning self-assembled nanoparticle superlattices by moulding microdroplets*. Nat Nano, 2008. **3**(11): p. 682-690.
146. Campolongo, M.J., et al., *Crystalline Gibbs Monolayers of DNA-Capped Nanoparticles at the Air–Liquid Interface*. ACS Nano, 2011. **5**(10): p. 7978-7985.
147. Pal, S., et al., *DNA-Origami-Directed Self-Assembly of Discrete Silver-Nanoparticle Architectures*. Angewandte Chemie International Edition, 2010. **49**(15): p. 2700-2704.
148. Sharma, J., et al., *Control of Self-Assembly of DNA Tubules Through Integration of Gold Nanoparticles*. Science, 2009. **323**(5910): p. 112-116.

## Chapter 2

149. Le, J.D., et al., *DNA-Templated Self-Assembly of Metallic Nanocomponent Arrays on a Surface*. Nano Letters, 2004. **4**(12): p. 2343-2347.
150. Zheng, J., et al., *Two-Dimensional Nanoparticle Arrays Show the Organizational Power of Robust DNA Motifs*. Nano Letters, 2006. **6**(7): p. 1502-1504.
151. Mastroianni, A.J., S.A. Claridge, and A.P. Alivisatos, *Pyramidal and Chiral Groupings of Gold Nanocrystals Assembled Using DNA Scaffolds*. Journal of the American Chemical Society, 2009. **131**(24): p. 8455-8459.
152. Aldaye, F.A. and H.F. Sleiman, *Dynamic DNA Templates for Discrete Gold Nanoparticle Assemblies: Control of Geometry, Modularity, Write/Erase and Structural Switching*. Journal of the American Chemical Society, 2007. **129**(14): p. 4130-4131.
153. Pinheiro, A.V., et al., *Challenges and opportunities for structural DNA nanotechnology*. Nat Nano, 2011. **6**(12): p. 763-772.
154. Pal, S., et al., *DNA Directed Self-Assembly of Anisotropic Plasmonic Nanostructures*. Journal of the American Chemical Society, 2011. **133**(44): p. 17606-17609.
155. Hung, A.M., H. Noh, and J.N. Cha, *Recent advances in DNA-based directed assembly on surfaces*. Nanoscale, 2010. **2**(12).
156. Perl, A., D.N. Reinhoudt, and J. Huskens, *Microcontact Printing: Limitations and Achievements*. Advanced Materials, 2009. **21**(22): p. 2257-2268.
157. Salaita, K., Y. Wang, and C.A. Mirkin, *Applications of dip-pen nanolithography*. Nat Nano, 2007. **2**(3): p. 145-155.
158. Maune, H.T., et al., *Self-assembly of carbon nanotubes into two-dimensional geometries using DNA origami templates*. Nat Nano, 2010. **5**(1): p. 61-66.
159. Noh, H., et al., *50 nm DNA Nanoarrays Generated from Uniform Oligonucleotide Films*. ACS Nano, 2009. **3**(8): p. 2376-2382.
160. Hung, A.M., et al., *Large-area spatially ordered arrays of gold nanoparticles directed by lithographically confined DNA origami*. Nat Nano, 2010. **5**(2): p. 121-126.

## Chapter 2

161. Kershner, R.J., et al., *Placement and orientation of individual DNA shapes on lithographically patterned surfaces*. Nat Nano, 2009. **4**(9): p. 557-561.
162. Zhou, Y., et al., *Shape-Selective Deposition and Assembly of Anisotropic Nanoparticles*. Nano Letters, 2014. **14**(4): p. 2157-2161.
163. Yin, Y., Y. Lu, and Y. Xia, *Assembly of monodispersed spherical colloids into one-dimensional aggregates characterized by well-controlled structures and lengths*. Journal of Materials Chemistry, 2001. **11**(4): p. 987-989.
164. Duan, H. and K.K. Berggren, *Directed self-assembly at the 10 nm scale by using capillary force-induced nanocohesion*. Nano letters, 2010. **10**(9): p. 3710-3716.
165. Choi, S., et al., *Coffee-ring effect-based three dimensional patterning of micro/nanoparticle assembly with a single droplet*. Langmuir, 2010. **26**(14): p. 11690-11698.
166. Alba, M., et al., *Macroscale Plasmonic Substrates for Highly Sensitive Surface-Enhanced Raman Scattering*. Angewandte Chemie International Edition, 2013. **52**(25): p. 6459-6463.
167. Kraus, T., et al., *Nanoparticle printing with single-particle resolution*. Nat Nano, 2007. **2**(9): p. 570-576.
168. Hamon, C., et al., *Hierarchical Self-Assembly of Gold Nanoparticles into Patterned Plasmonic Nanostructures*. ACS Nano, 2014. **8**(10): p. 10694-10703.

## Chapter 2

---

## **Chapter 3. Probing Soft Corona Structures of DNA-Capped Nanoparticles by Small Angle Neutron Scattering**

---

## Chapter 3

## Chapter 3

### 3.1 Introduction

Since 1996, DNA-capped nanoparticles have demonstrated a plethora of exciting applications including advanced materials[1, 2], biodiagnostics[3, 4] and drug delivery[5]. It has been shown that they may be exploited to detect trace amounts of DNA[6], protein[7, 8], small molecules[9] and metal ions[10-13] as well as nanocarriers of nucleic acids for gene regulation[5, 14]. In addition, DNA-capped nanoparticles are promising building blocks for novel plasmonic metamaterials and nanodevices[2, 6, 15]. They can be employed to build highly-ordered superstructures with precise periodicity and complexity[16], forming well-defined assemblies (“artificial molecules”[17, 18], “superacrystals”[19-21]).

For any particular application, the key parameters affecting DNA corona structures such as DNA sequence, length and number density and ionic strength require a high degree of control and selection [15, 19, 22, 23]. For example, it has been found that DNA density directly affects the cellular uptake efficiency of nanoparticles[24]. The DNA density on gold nanoparticle surfaces also influences the hybridization kinetics[25]: in the low density ( $<3 \times 10^{12}$  molecules/cm<sup>2</sup>) regime, almost all the DNA can be hybridized, and the kinetics of binding are faster, however, at a high density ( $<5 \times 10^{12}$  molecules/cm<sup>2</sup>), the extent of hybridisation reduces by 10% and the kinetics are much slower.

In principle, DNA molecules are polyelectrolytes which can form a brush-like polymer conformation on nanoparticles, with mushroom, crossover and highly stretched regimes depending on the grafting number densities[26]. Dynamic light scattering has shown that highly stretched DNA brush heights correspond to the length of single-stranded DNA[15]. The microcantilever technique has also

## Chapter 3

indicated the pH-dependent changes of DNA conformation occur, revealing the effects of hydration and electrostatic forces on DNA hybridization[27]. In addition, curvature of the particle surface can affect DNA loading capacity and DNA hybridization[28]. Smaller nanoparticles show a higher probe-loading capacity than the larger ones and, when particle diameter increases to 60 nm, DNA packing is similar to that of a planar metal surface[29]. Classical density functional theory and molecular dynamics simulations have been utilized to develop a cell model to predict the ion cloud around spherical nanoparticles affected by DNA densities, bulk ionic concentrations and the sizes of nanoparticles and chains[30].

Despite these advances, complex DNA corona structures remain elusive. Recent advances in synchrotron-based X-ray techniques have revealed the crystalline structures of DNA-capped nanoparticle assemblies under various conditions[15, 19, 23, 31] but provided no information on the DNA corona since the scattering signals mainly arise from the electron-dense nanoparticle cores.[32] However, it is possible to manipulate the signal from the DNA corona using small angle neutron scattering (SANS) combined with solvent contrast variation and this forms the motivation for the present investigation.

### 3.2 Methods and Materials

#### 3.2.1 Materials

Gold (III) chloride trihydrate ( $\text{HAuCl}_4 \cdot 3\text{H}_2\text{O}$ , 520918) and trisodium citrate dehydrate ( $\text{C}_6\text{H}_5\text{Na}_3\text{O}_7 \cdot 2\text{H}_2\text{O}$ , S1804) were purchased from Sigma (St. Louis, MO, USA). Thiolated DNA oligonucleotides were purchased from Integrated DNA Technologies (Coralville, IA, USA).

## Chapter 3

### 3.2.2 Synthesis of DNA-Capped AuNP Conjugates

The citrate-gold nanoparticle colloid solution was synthesized by a modified citrate reduction procedure that was first pioneered by Turkevich et al. [33] and further refined by Frens [34]. Briefly, 170 mL Milli-Q water and 2 mL HAuCl<sub>4</sub> (25mM) are heated to boiling in an oil bath and citrate solution 6 mL (34 mM) is added to reduce Au<sup>3+</sup> ions into gold atoms under vigorous stirring. The colloid color changed from yellow to wine red during heating for 10 min. The heat source is removed and the sample cooled to room temperature and stored in the fridge at 4 °C for future use.

DNA-capped nanoparticle synthesis followed Michael's salt-aging protocol with some modifications [31]. Briefly, thiolated oligonucleotides were de-protected using dithiothreitol and incubated with gold nanoparticle solutions at a DNA-to-nanoparticle mole ratio of 250:1. After 12 hour incubation, sodium chloride was added to a final concentration of 1 M, the mixture was then aged for 24 hours at room temperature. The mixture was subsequently centrifuged and washed in D<sub>2</sub>O, the pellets were redispersed in 10 mM Tris-HCl buffer (pH 7.2) with varying NaCl concentration in D<sub>2</sub>O, and the supernatant collected for further UV measurement.

### 3.2.3 UV Measurement

The number loading of single strand DNA (ssDNA) on AuNPs was calculated by UV measurement. The amount of unattached ssDNA after DNA-cap reaction was determined by centrifuging the supernatant of the salt ageing reaction solution. The supernatant was measured by UV spectrophotometer (NanoDrop™). The amount of ssDNA on the AuNPs was calculated by

## Chapter 3

subtraction of the unattached ssDNA from the initially added ssDNA which was also measured by NanoDrop™. The number of gold nanoparticles was measured using an Agilent 8453 UV-Vis Spectrophotometer following the DNA capping of the gold nanoparticles.

### 3.2.4 Dynamic Light Scattering Measurement

Dynamic Light Scattering (DLS) measurements of conjugate size distribution were performed on a Zetasizer Nano ZS (Malvern) at the Melbourne Centre for Nanofabrication (MCN), Clayton, Victoria, Australia. Each sample was prepared in 10 mM Tris-HCl buffer (pH 7.6) with varying NaCl concentration. Aliquots of 1 mL per sample were loaded into polystyrene cuvettes for analysis. The instrument used a 633 nm He-Ne laser with a scattering angle of 173°. Each measurement was performed in quintuplicate at a temperature of 22°C.

### 3.2.5 Small-Angle Neutron Scattering

Small-angle neutron scattering (SANS) experiments were performed on the QUOKKA instrument at the Australian Nuclear Science and Technology Organization (ANSTO). All the samples contained a volume fraction of gold,  $\phi \approx 1.4 \times 10^{-4}$ , and were loaded into 1 mm path length quartz cuvettes held in a temperature stabilized rack at the desired temperature. SANS data were collected at three sample-to-detector (1.2 m, 8 m, and 20 m) distances to provide a  $q$  range from 0.004 to 0.72 Å<sup>-1</sup> with a neutron wavelength of  $\lambda = 4.91$  Å, and a resolution of  $\Delta\lambda/\lambda = 10\%$  [35]. An empty beam background, empty cell background, sample transmission, sample thickness and detector sensitivity were accounted for during data reduction. The reduced scattering intensities on an absolute scale,  $I(q)$ , were fitted as a function of the scattering vector,  $q$  where

## Chapter 3

$q = 4\pi \sin(\theta)/\lambda$ , and  $2\theta$  is defined as the scattering angle. Indirect Fourier Transform of the SANS data was performed using GNOM 4.6 [36]. Other methods for SANS scattering data analysis were performed using Igor Pro 6.34A software and models provided by National Institute of Standards and Technology (NIST, US) [37].

### 3.2.6 Small-Angle X-Ray Scattering

Small-angle X-ray scattering (SAXS) experiments were performed on a Bruker Nanostar instrument at ANSTO using a Cu K $\alpha$  source with a wavelength of 1.54 Å enabling an accessible  $q$  range from 0.005 Å<sup>-1</sup> to 0.35 Å<sup>-1</sup>. SANS and SAXS experiments were performed on the same samples.

### 3.2.7 SANS and SAXS Data Analysis

SANS intensity  $I(q)$  as a function of scattering vector for a dispersion of nanoparticles can be written as

$$I(q) = \phi P(q) S(q) \quad (1)$$

where,  $\phi$  is the particle volume fraction,  $P(q)$  is the form factor,  $S(q)$  is the structure factor.  $S(q)$  depends on the spatial arrangement of the particles. As the system under study concerns particles at a low concentration (volume fraction  $\phi \approx 1.4 \times 10^{-4}$ ), the structure factor is assumed to be unity, thus  $S(q) = 1$ . The form factor,  $P(q)$ , depends on the particle shape and size. In our system DNA-capped AuNP conjugate may be considered as a core-shell structure, the core-shell form factor is defined as the following formula (2) [38].

$$P(q) = \frac{\text{scale}}{V_s} \left[ 3V_c(\rho_c - \rho_s) \frac{[\sin(qr_c) - qr_c \cos(qr_c)]}{(qr_c)^3} + 3V_s(\rho_s - \rho_{\text{solv}}) \frac{[\sin(qr_s) - qr_s \cos(qr_s)]}{(qr_s)^3} \right]^2 \quad (2)$$

## Chapter 3

where scale is the scale factor,  $V_s$  is the volume of the outer shell,  $V_c$  is the volume of the core,  $r_s$  is the radius of the shell,  $r_c$  is the radius of the core,  $\rho_c$ ,  $\rho_s$  and  $\rho_{\text{solv}}$  is the scattering length density of the core, shell and solvent respectively.

In the polydisperse core-shell model fitting process, the parameters describing the gold core radius and polydispersity were determined from fitting the SAXS scattering data to a Schulz sphere model. Since X-ray scattering lengths increase linearly with the atomic number of the atom, the SAXS scattering intensity is mainly determined by the gold core. In this study the gold core mass density is equivalent to a solid gold, whose scattering length density  $1.25 \times 10^{-4} \text{ \AA}^{-2}$ . The neutron scattering is isotopically dependent and, here, is strongly influenced by the presence of hydrogenous material in the shell that may be contrasted with respect to the deuterated solvent. Therefore, the SAXS data yields information of the gold core while SANS provides details concerning the DNA corona information. The scattering length densities (SLD) used in the small angle scattering data analysis are described in Table 3.1[39]. The DNA sequence for T15 and T7-8 are different as are the molecular weights; in addition, the number of exchangeable hydrogens in DNA is also accounted in the calculation due to DNA-NP conjugates being dispersed in  $D_2O$  yielding an influence on neutron scattering length.

## Chapter 3

Table 3.1 R<sub>g</sub> values obtained from IFT and Guinier fitting of SANS scattering data of T15 and T7-8 conjugates at varies salt concentrations. R<sub>H</sub> values obtained from DLS measurement.

sample	Salt concentration(M)	R <sub>g</sub> from IFT (Å)	R <sub>g</sub> from Guinier fitting (Å)	R <sub>H</sub> from DLS(Å)
T15-AuNP	0	88.0	90.6	112.0
T15-AuNP	0.5	83.4	87.0	101.5
T15-AuNP	1	81.4	82.3	102.4
T7-8-AuNP	0	87.9	90.3	111.1
T7-8-AuNP (aggregated)	0.5	132.1	108.8	168.2

To obtain the information on shape and size of the DNA-capped Au nanoparticle, Indirect Fourier Transformation (IFT) of the data was also employed and analysed using the program GNOM [36]. The evaluation of the small-angle scattering data using IFT leads to the determination of the pair distance distribution function  $p(r)$  containing information on shape and size [40]. For an isotropic solution  $p(r)$  and  $I(q)$  are related via the Fourier transform:

$$I(q) = 4\pi \int_0^\infty p(r) \frac{\sin qr}{qr} dr \quad (3)$$

The single particle radius of gyration ( $R_g$ ) can be calculated from the  $p(r)$  function by integrating the function with  $r^2$  over all values of  $r$ .

$$R_g^2 = \frac{\int_0^{D_{\max}} r^2 p(r) dr}{2 \int_0^{D_{\max}} p(r) dr} \quad (4)$$

## Chapter 3

Besides IFT functions, another model-independent method, Guinier analysis, has also been applied. In the low  $q$  region, Guinier analysis with a straight-line fit can readily provide the radius of gyration ( $R_g$ ), using

$$I(q) = I_0 \exp\left(-\frac{q^2 R_g^2}{3}\right) \quad (5)$$

### 3.2.9 Properties of DNA Corona from Models

The scattering length of T15 and T7-8 were calculated from their chemical composition taking into account liable hydrogens exchangeable with  $D_2O$  [41]. The total scattering length of the DNA corona was calculated using parameters in Table 3.4 as

$$SL_{\text{shell}} = V_{\text{shell}} \cdot SLD_{\text{shell}} \quad (6)$$

As the DNA corona was composed of DNA molecules and solvent (with or without salt), the following two equations were used to calculate the number of solvent molecules in the corona, solvent, and the molecular volume of DNA,  $V_{\text{DNA}}$

$$SL_{\text{shell}} = n_{\text{DNA}} SL_{\text{single DNA}} + n_{\text{solvent}} SL_{\text{single solvent}} \quad (7)$$

$$V_{\text{shell}} = n_{\text{DNA}} V_{\text{DNA}} + n_{\text{solvent}} V_{\text{single solvent}} \quad (8)$$

where the number of DNA per particles,  $n_{\text{DNA}}$ , was determined by UV measurements, and the volume of solvent  $V_{\text{single solvent}}$  was calculated from solvent density taking into account contribution from NaCl.

The volume fraction of DNA in the corona was then calculated as

$$\text{Volum fraction}_{\text{DNA}} = \frac{n_{\text{DNA}} V_{\text{DNA}}}{V_{\text{shell}}} \quad (9)$$

## Chapter 3

### 3.3 Results and Discussion

As a model system, two thiolated 15mer single stranded DNA (ssDNA) strands were selected. The first one has non-base-pairing poly thymine sequence (5'-SH-T<sub>15</sub>-3', denoted as T15) while the second one comprises a segment of 7 thymine bases at the 5' end followed by a palindromic segment with 8 sequences (5'-SH-T<sub>7</sub>-CTCATGAG-3', denoted as T7-8). Following the previous protocol [15], the two types of DNA strands were conjugated to spherical ~13 nm gold nanoparticle surfaces with nearly highest number density. The as-prepared conjugates are stable at high ionic strength and a wide range of temperatures without forming permanent aggregates.

#### 3.3.1 Salt Effects on Conjugates Size

By combined small angle X-ray scattering (SAXS) and SANS, the effects of salt concentration on the two types of DNA coronas at 22 °C were first examined (Figures 3.1 and 3.2). While the scattering curves of T15-AuNP have similar shapes in 10 mM Tris buffer (pH 7.2) under different salt concentrations (Figure 3.1b and 3.2a), there are significant changes in the scattering curves for T7-8-AuNP at increased salt concentration (Figure 3.1c, b). Particularly, a peak in the low  $q$  region emerged when the salt concentration increased to 1 M. Model-independent analysis via Indirect Fourier Transform (IFT) shows that T15-AuNP and T7-8-AuNP have almost identical symmetric bell-shaped pair-distance distribution,  $p(r)$ , functions, suggesting these two DNA sequences give the same spherical shape as the conjugates in the absence of salt.[36] In accord with their similar  $p(r)$  functions, IFT yielded particles of a similar radius of gyration,  $R_g$  (88.0 Å for T15-AuNP and 87.9 Å for T7-8). Although the  $R_g$  values from Guinier analysis are slightly higher than those from IFT, T15-AuNP and T7-8-AuNP have

## Chapter 3

similar values (90.6 and 90.3 Å, respectively). Also, both particles have similar hydrodynamic radius (DLS measurements, Table 3.1) in the absence of salt.

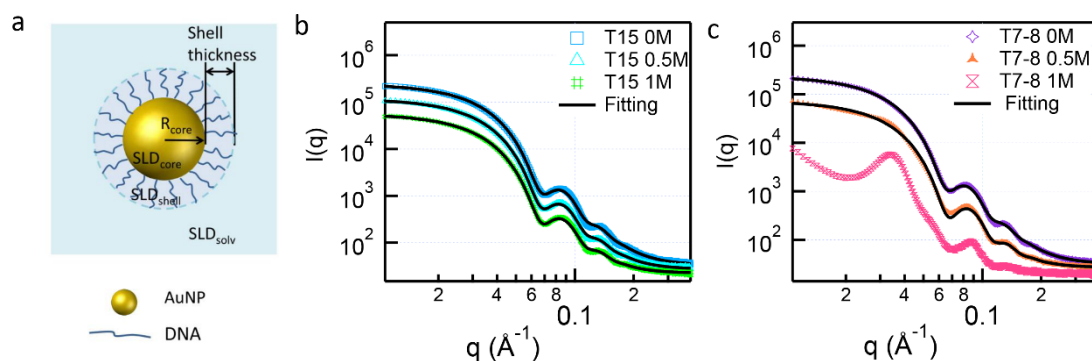


Figure 3.1 (a) Schematic of DNA-Au conjugate in the polycore-shell model. SAXS scattering data of T15 (b) and T7-8(c) at various salt concentrations (0M, 0.5M, and 1M). Solid lines show the fits by Schulz distribution of spheres.

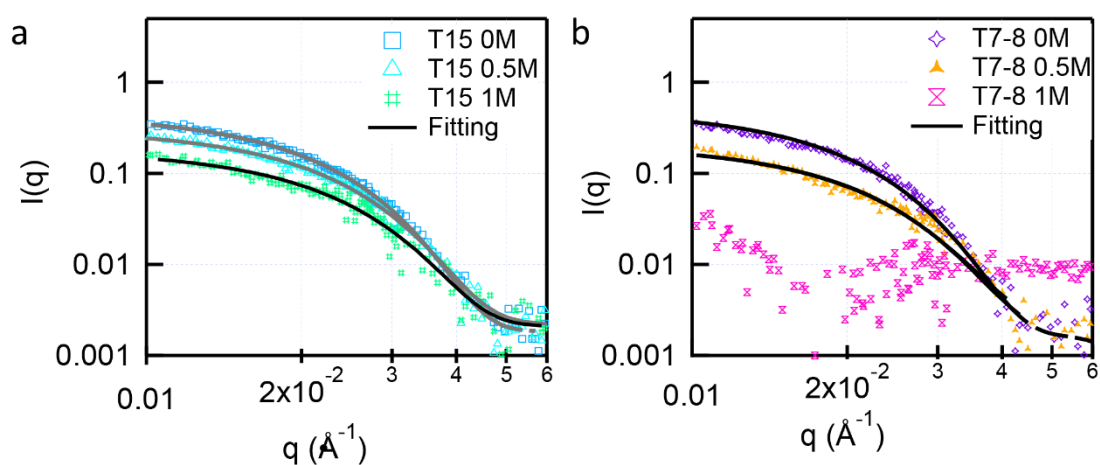


Figure 3.2 SANS scattering data of T15(a) and T7-8(b) at various salt concentrations (0M, 0.5M, 1M). Solid lines show the fits by poly core-shell model.

### 3.3.2 Salt Effects on Conjugates Shape

However, T15-AuNP and T7-8 AuNP show significant differences in both  $R_g$  and  $p(r)$  functions at higher salt concentrations. While the  $R_g$  value of T15-AuNP

## Chapter 3

decreases from 88.0 Å to 83.4 Å (0.5 M NaCl) and 81.4 Å (1 M NaCl), the  $R_g$  value of T7-8-AuNP increases from 87.9 Å to 132.1 Å (0.5 M NaCl). As shown in Figure 3.3a, there is a slight decrease in maximum diameter ( $D_{max}$ ) in the  $p(r)$  function for T15-AuNP at higher salt concentration and the T15 conjugate retains a bell-shape  $p(r)$ . This suggests that the shape of the T15 conjugate remains largely the same although its size is smaller.

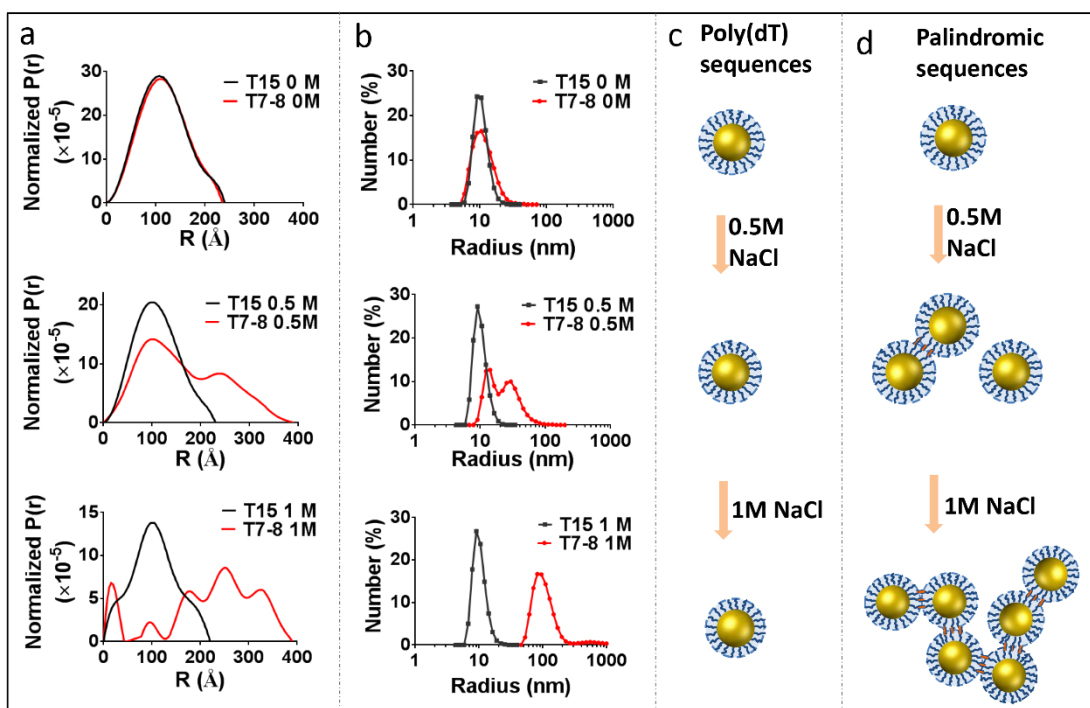


Figure 3.3 (a)  $p(r)$  function and (b) size distribution of T15 and T7-8 conjugates at various salt concentrations obtained from IFT analysis and DLS measurements respectively. (c) and (d) represent a scheme for the salt effect on poly(dT) DNA and palindromic DNA.

In contrast, there are two peaks in the distribution function for the T7-8 conjugate in 0.5 M salt, suggesting that the palindromic DNA hybrid possibly forms a dimer structure (Figure 3d). The first peak shows the same position as T15, corresponding to the remaining monomers of T7-8. The second peak is an

## Chapter 3

indication of dimer formation. In consistence with IFT data, DLS data also shows two peaks for T7-8 at 0.5 M. With further salt increase to 1M, the T7-8 conjugate aggregated to form a larger-scale cluster; the oscillations in the  $p(r)$  function are a result of data truncation due to the aggregates being larger than the inverse of minimum  $q$ . As a result both  $D_{\max}$  and  $R_g$  cannot be reliably determined for T7-8-AuNP at 1M NaCl concentrations due to the polydisperse nature of the aggregated system and the limit of  $q_{\min}$ . Nevertheless, the SANS data reflects the aggregation of T7-8-AuNP at high salt concentrations. Aggregation was also confirmed by DLS measurements (Figure 3.3b). The different effects of salt on poly (dT) sequenced T15-AuNP and palindromic sequenced T7-8-AuNP are schematically presented in Figures 3c and 3d. For T7-8-AuNPs, their palindromic sequences hybridise at high ionic strength, resulting in the observed large aggregates. For T15-AuNPs, the DNA corona was compressed at higher salt concentration without the formation of aggregates.

Further analysis of the small-angle scattering data has been carried out by model-dependent fitting. Since the X-ray signal from the gold core vastly dominates that from the DNA, a model using a Schulz distribution of spheres is sufficient to describe the SAXS data (Figure 3.1b and 3.1C). In the absence of salt, the fitting gives the radius of the gold core as 63.8 Å and 65.7 Å for T15-AuNP and T7-8 conjugates with a small polydispersity value of 0.128 and 0.126, respectively. To fit the SANS data, a core-shell model was used that accounts for the contributions both from the gold core and the DNA corona (Figure 3.2). The values from the SAXS fits are used to constrain the core parameters (size and polydispersity) in the SANS fitting. As the scattering length density of the solution and gold core can be determined from their mass density and chemical

## Chapter 3

composition (Table 3.2), only the thickness and scattering length density of the shell are refinable parameters for the fitting of SANS data. The resultant parameters for the core-shell models at different salt concentrations are summarized in Table 3.3. Note that no model fitting has been attempted for T7-8-AuNP at 0.5M and 1 M due to the aggregation.

Table 3.2 Neutron and X-ray scattering length densities used in the analysis.

Material	$\rho(\text{g}/\text{cm}^3)$	SLD( $\text{\AA}^{-2}$ ) in SAXS	SLD( $\text{\AA}^{-2}$ ) in SANS
Gold	19.3	$1.25 \times 10^{-4}$	$4.5 \times 10^{-6}$
10mM Tris buffer in D <sub>2</sub> O	1.1	$9.37 \times 10^{-6}$	$6.34 \times 10^{-6}$
0.5 M NaCl, buffer in D <sub>2</sub> O	1.118	$9.51 \times 10^{-6}$	$6.31 \times 10^{-6}$
1 M NaCl,buffer in D <sub>2</sub> O	1.136	$9.66 \times 10^{-6}$	$6.29 \times 10^{-6}$

Table 3.3 Fit parameters from SAXS and SANS data using Schulz sphere distribution and poly core shell model respectively.

sample	Salt concentration (M)	SAXS		SANS				
		AuNP core radius ( $\text{\AA}$ )	Polydispersity	Shell thickness ( $\text{\AA}$ )	SLD of shell ( $\times 10^{-6} \text{\AA}^{-2}$ )	Shell volume ( $\times 10^6 \text{\AA}^3$ )	DNA molecular volume ( $\times 10^3 \text{\AA}^3$ )	DNA fraction v/v% in shell
T15 - AuNP	0	63.8	0.128	65.8	6.00	8.06	4.63	11.08
T15- AuNP	0.5	64.0	0.125	60.7	5.97	7.02	4.41	12.05
T15- AuNP	1	64.1	0.120	59.1	5.95	6.73	4.31	12.31
T7-8- AuNP	0	65.7	0.126	65.2	5.96	8.21	4.78	13.80

### 3.3.3 DNA Corona Configuration

The different input ratios of DNA: nanoparticle in the initial reactions were used and the self-assembly process of thiolated DNA followed the expected Langmuir adsorption isotherms (Figure 3.4). Based on the isotherms, under DNA: NP

## Chapter 3

molar ratio of 250:1 preparation conditions, there are  $192 \pm 8$  oligonucleotides per particle ( $3.7 \pm 0.15 \times 10^{13}$  oligos/cm<sup>2</sup>) for T15 and  $237 \pm 13$  oligonucleotides/particle ( $4.6 \pm 0.25 \times 10^{13}$  oligos/cm<sup>2</sup>) for T7-8. The slightly higher value of surface coverage for T7-8 might be attributed to the potential of the self-complementary strand to hybridize with another strand via hydrogen bonding. The chosen conditions give the surface coverages of both T15 and T7-8 of around 50% of their maximum coverage. This moderate coverage value is the most representative condition and is expected to allow DNA molecules to be flexible on Au particle surfaces while giving sufficient signals for neutron scattering measurements.

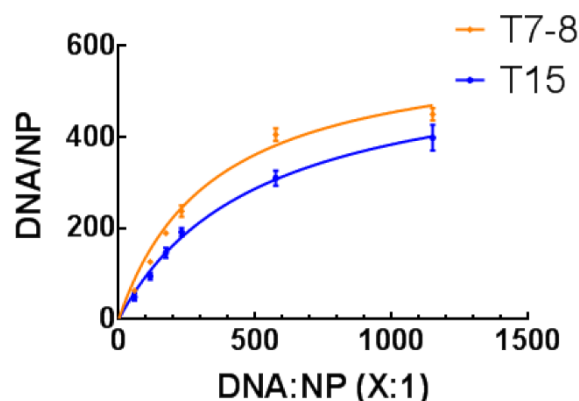


Figure 3.4 DNA adsorption curves of different initial DNA: AuNP ratios. The dots show the number of moles of DNA adsorbed per nanoparticle; the error bars represent the standard deviation of six independent measurements. Solid lines correspond to the fits calculation.

In the absence of salt, the thickness of the T7-8 corona ( $65.2 \text{ \AA}$ ) is similar to the T15 corona ( $65.8 \text{ \AA}$ ) while its SLD ( $5.96 \times 10^{-6} \text{ \AA}^{-2}$ ) is slightly smaller than the T15 corona ( $6.00 \times 10^{-6} \text{ \AA}^{-2}$ ). Note that the T15 molecule has a smaller scattering

## Chapter 3

length ( $1.517 \times 10^{-10}$  cm) and hence a higher contrast than T7-8 ( $1.715 \times 10^{-10}$  cm) with respect to  $D_2O$  (Table 3.4). On the other hand, there are fewer oligomers on T15-AuNP ( $192 \pm 8$  oligonucleotides per particle) than T7-8 ( $237 \pm 13$  oligonucleotides/particle) as determined from the DNA adsorption curve (Figure 3.4). These two opposing effects result in similar shell scattering length density for both particles. Despite the difference in their surface coverage, the T15 corona and T7-8 corona have similar values of shell thickness, suggesting that both DNAs extend from the gold particle surface in a similar configuration. In fact, the  $p(r)$  functions of T15 and T7-8 share a similar shape (Figure 3.3a), suggesting a similar conformation of T15 and T7-8 in the absence of salt.

Table 3.4 Scattering length of DNA.

DNA	number of exchangeable H	SL ( $\times 10^{-2}$ Å)	SL (after exchanging H with D in $D_2O$ ) ( $\times 10^{-2}$ Å)
T15	29	1.215	1.517
T7-8	39	1.309	1.715

As the palindromic sequence T7-8-AuNP forms aggregates at high salt concentrations, the following discussions on the salt-induced conformation change of DNA are focused on poly (dT) sequences T15-AuNP. Importantly, the increase of the salt concentration does not change the polydispersity of T15-AuNP, confirming that the system is well dispersed even at high salt concentration. Although salt did not affect the shape of the poly(dT) sequenced DNA capped conjugate, the thickness of the DNA corona decreases with salt addition. The shell thickness of the T15 conjugate (from the poly core-shell model) reduced from 65.8 Å (0 M NaCl) to 60.7 Å (0.5 M NaCl) and 59.1 Å (1 M

### Chapter 3

NaCl). As the salt concentration increases, excess cations are anticipated to reduce repulsion along the negatively charged backbone of the DNA, thus resulting in a compaction of the DNA corona. Our findings are consistent with Chen et al. which also showed that length of poly(dT) sequences DNA in free solution decreased with increased salt concentration.[42] It is possible that electrostatic repulsion within the DNA chain is sufficiently depressed at a salt concentration of 0.5M, and further DNA compaction is reduced when salt concentration is increased to 1 M.

A decrease of the shell thickness from 65.8 Å (0 M salt) to 60.7 Å (0.5 M salt) corresponds to a change of shell volume from  $8.06 \times 10^6 \text{ Å}^3$  to  $7.02 \times 10^6 \text{ Å}^3$ . Note that the corona is occupied by DNA and solvent; as a result, the decrease in the shell volume would imply a reduction in proportion of solvent in the corona. Since the SLD of the solvent is greater than that of DNA, decreased solvation would therefore result in a decrease in the corona SLD. However, this is not observed here. In the absence of salt the difference of SLD between the shell ( $6.00 \times 10^{-6} \text{ Å}^{-2}$ ) and the solvent ( $6.34 \times 10^{-6} \text{ Å}^{-2}$ ) is  $0.34 \times 10^{-6} \text{ Å}^{-2}$ ; at a salt concentration of 0.5 M, the contrast between the shell ( $5.97 \times 10^{-6} \text{ Å}^{-2}$ ) and the solvent ( $6.31 \times 10^{-6} \text{ Å}^{-2}$ ) remains as  $0.34 \times 10^{-6} \text{ Å}^{-2}$  i.e. the smaller volume of the DNA corona does not lead to an increase in contrast between the DNA shell and bulk solvent. The observed behavior may arise from either a decrease in volume of the DNA itself, an increase in the physical density of the solvent in the corona (decrease in solvent volume) compared to the bulk or a combination thereof. Further calculations (section 3.2.9) assuming solely the former effect suggest that the molecular volume of DNA decreases from  $4.63 \times 10^3 \text{ Å}^3$  (0 M NaCl) to  $4.41 \times 10^3 \text{ Å}^3$  (0.5 M NaCl) and  $4.31 \times 10^3 \text{ Å}^3$  (1 M NaCl). Thus, the increase of salt

## Chapter 3

concentration does not only result in a decrease in the total volume of the DNA corona but also the volume occupied by individual DNA chains. However, this does not preclude the influence of solvent density increase in the corona. In an analysis of the protein–solvent interface, it is demonstrated that hydration shell around proteins is denser than the bulk solvent.[43]

### 3.3.4 The Temperature Effects on Conjugate Shape

The influence of temperature was also investigated by SANS (Figure 3.5) at fixed salt concentration of 0.5 M by measuring the scattering at an initial 30°C to 46°C, 70°C and then decreasing to 22°C.  $P(r)$  functions are shown in Figure 3.6. The T15 conjugate maintains a bell-shape function as the temperature is changed which indicates that the particle shape is largely conserved (Figure 3.6a). The  $p(r)$  function of the T7-8 conjugate maintains two peaks at 30°C but as the temperature is increased from 30°C to 46°C, the T7-8 conjugate  $p(r)$  function changed from two peaks to a single bell-shape peak (Figure 3.6b) suggesting a dimer to globule transition. Figure 3.6b shows the schematic of the shape change at different temperatures for palindromic sequenced DNA conjugates. DNA de-hybridisation occurs on increasing the temperature to 46°C; this is above melting temperature of 8-base palindromic sequences (35-37°C, at 50 $\mu$ M DNA 0.5M salt condition calculated from IDT OligoAnalyzer). As the temperature is further increased from 46°C to 70°C, the globular structure remains unchanged. However, when the temperature is reduced from 70°C to 22°C, the T7-8 conjugate forms larger-scale clusters (as observed by the data-truncated oscillations in the  $p(r)$  function). The possible explanation for this interesting behaviour is that palindromic sequenced T7-8 reforms to the hybrid state on cooling and annealing enables more DNA strands to hybridise to form clusters.

## Chapter 3

Indeed, in Mirkin and Gang's studies,[19, 20] it was found that slow annealing of DNA-capped gold nanoparticles can lead to particle self-assembly and crystallization to form ordered structures. Interparticle organisation of such crystalline nanostructure could also be investigated by neutron scattering and is subjected to future study.

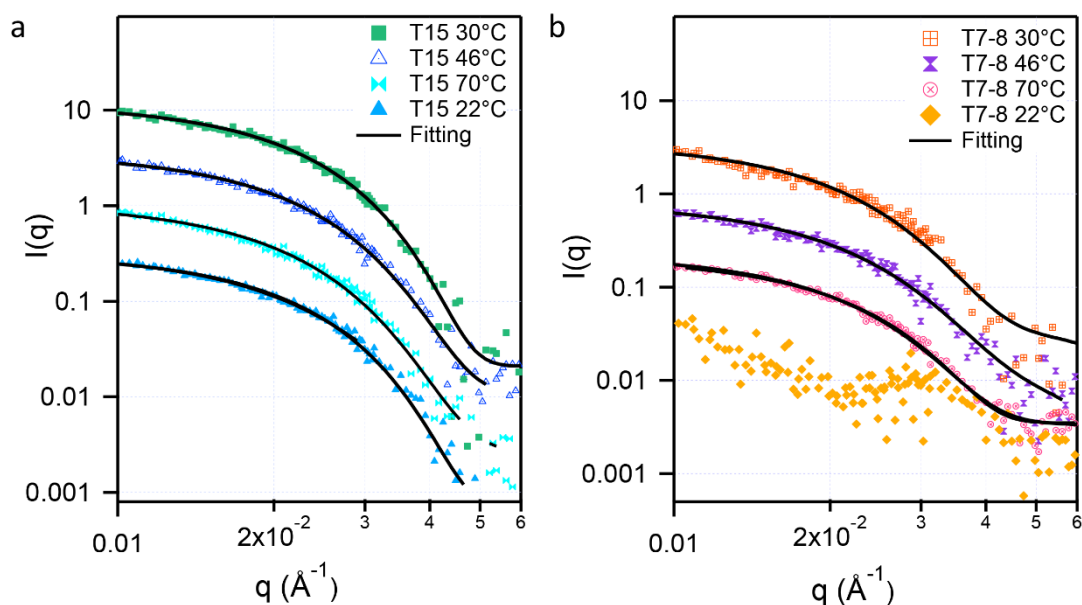


Figure 3.5 SANS scattering data of T15 (a) and T7-8 (b) as a function of temperature. The plotted data are offset for clarity as follows: 10x for T15 70°C and T7-8 46°C; 20x for T15 46°C and T7-8 70°C, 30x for T15 30°C.

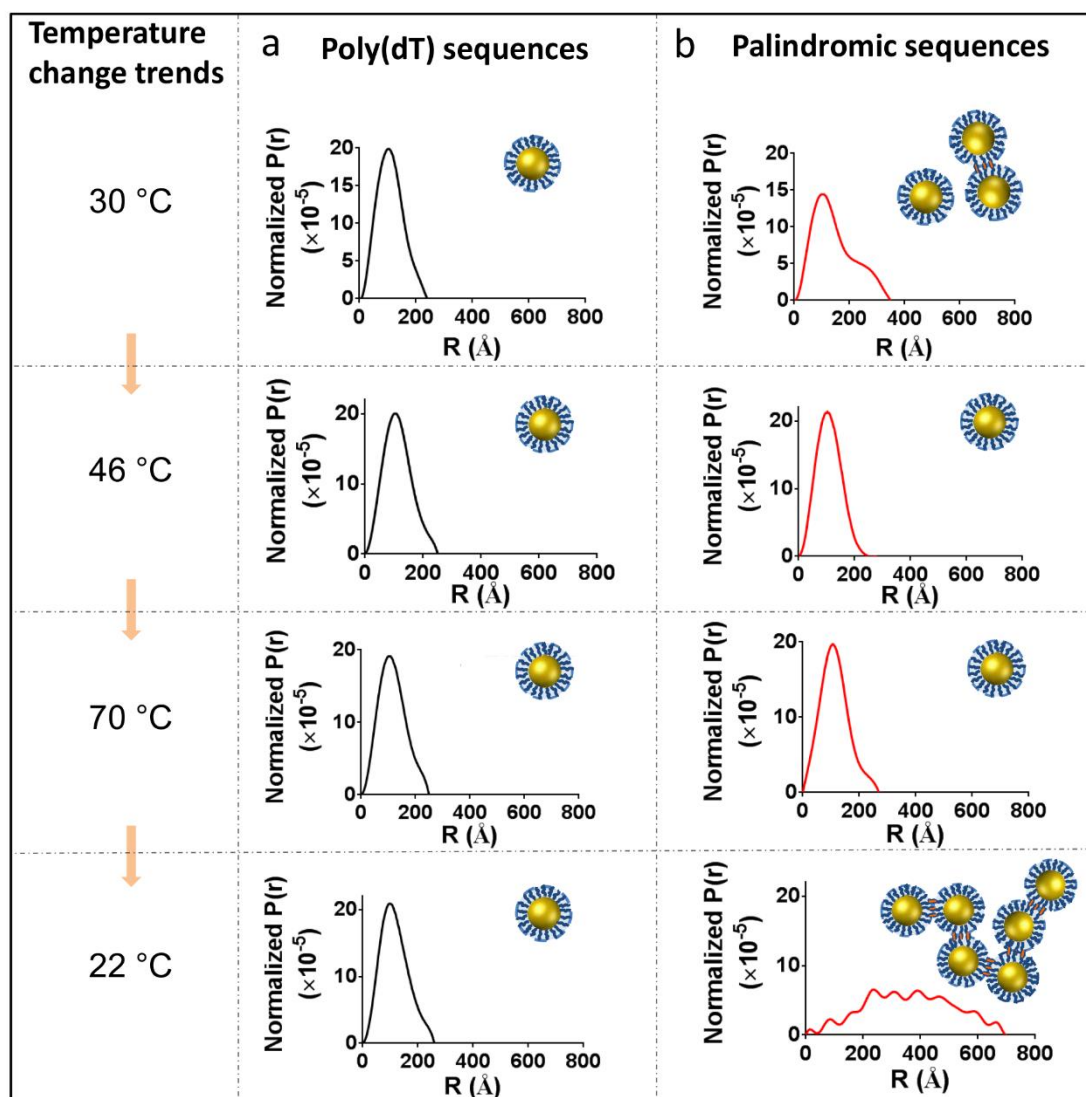


Figure 3.6 (a,b)  $p(r)$  distribution of T15 and T7-8 conjugates computed at various temperatures (30 °C, 46 °C, 70 °C, 22 °C) in 0.5M salt buffer. Insets are scheme of temperature effect on poly (dT) sequenced DNA and palindromic sequenced DNA.

### 3.3.5 The Temperature Effects on Conjugate Size

The corona of the poly (dT) sequenced DNA capped conjugate increased slightly on increasing temperature but appears to be reversible; from Table 3.5, the shell thickness of T15 increased from 60.4 Å (30 °C) to 60.5 Å (46 °C), 65.1 Å (70 °C), and decreased to 60.9 Å at 22 °C. Similarly, the increased and decreased corona

## Chapter 3

thickness resulted in fluctuation of the corona SLD. The DNA corona size change is also confirmed by  $R_g$  values from both IFT and Guinier analysis (Table 3.5). These findings are consistent with Jiang et al. who also showed that ssDNA stretched as temperature was increased.[44]

Table 3.5 Shell thickness and SLD of shell obtained from fitting poly core-shell model of conjugates and  $R_g$  from IFT and Guinier fitting with changing temperature.

DNA	Temperature (°C)	Shell thickness (Å)	SLD of shell (Å <sup>-2</sup> )	$R_g$ from IFT (Å)	$R_g$ from Guinier fitting (Å)
T15-AuNP	30	60.4	5.98	84.0	85.3
T15-AuNP	46	60.5	5.98	87.1	87.0
T15-AuNP	70	65.1	6.00	88.8	90.5
T15-AuNP	22	60.9	5.95	89.0	88.9
T7-8-AuNP	30	66.8	6.01	115.1	112.5
T7-8-AuNP	46	67.3	6.03	87.9	86.9
T7-8-AuNP	70	69.6	6.07	87.8	88.3
T7-8-AuNP	22	aggregated	aggregated	aggregated	aggregated

\*Temperature increased from 30 degree to 70 degree, and then decreased to 22 degree.

### 3.4 Conclusion

Our work has demonstrated that small angle neutron scattering can provide structural insights on DNA-capped gold nanoparticles, and this opens the way to systematically study effects of different factors such as DNA length and type of ions on DNA structure in future.

## Chapter 3

In conclusion, soft DNA corona structures have been investigated in detail by neutron scattering techniques and clearly demonstrate that DNA-capped gold nanoparticle conjugates form globular particles in the absence of salt, regardless of the DNA sequence. However, distinct behaviors were observed for palindromic and non-palindromic DNA sequences. The non-palindromic DNA sequences maintain a globular or sphere-like shape under all the conditions investigated here although their corona heights are responsive to ionic strength and temperature. However, the palindromic DNA corona only maintains a sphere-like shape in the absence of salt and quickly exhibits hand-shaking base-pairing interactions upon addition of salt, leading to dimeric and multimeric aggregates depending on ionic strength. The results shown here may guide the design of tailor-made DNA corona structures for customizable designer materials for versatile applications in a range of arenas including the life sciences and optoelectronics.

### 3.5 References

1. Alivisatos, A.P., et al., Organization of 'nanocrystal molecules' using DNA. *Nature*, 1996. **382**(6592): p. 609-611.
2. Mirkin, C.A., et al., A DNA-based method for rationally assembling nanoparticles into macroscopic materials. *Nature*, 1996. **382**(6592): p. 607-609.
3. Elghanian, R., et al., Selective Colorimetric Detection of Polynucleotides Based on the Distance-Dependent Optical Properties of Gold Nanoparticles. *Science*, 1997. **277**(5329): p. 1078-1081.
4. Dubertret, B., M. Calame, and A.J. Libchaber, Single-mismatch detection using gold-quenched fluorescent oligonucleotides. *Nat Biotech*, 2001. **19**(4): p. 365-370.
5. Rosi, N.L., et al., Oligonucleotide-Modified Gold Nanoparticles for Intracellular Gene Regulation. *Science*, 2006. **312**(5776): p. 1027-1030.

### Chapter 3

6. Li, H.X. and L. Rothberg, Colorimetric detection of DNA sequences based on electrostatic interactions with unmodified gold nanoparticles. *Proceedings of the National Academy of Sciences of the United States of America*, 2004. **101**(39): p. 14036-14039.
7. Pavlov, V., et al., Aptamer-functionalized Au nanoparticles for the amplified optical detection of thrombin. *J Am Chem Soc*, 2004. **126**(38): p. 11768-9.
8. Huang, C.C., et al., Aptamer-modified gold nanoparticles for colorimetric determination of platelet-derived growth factors and their receptors. *Anal Chem*, 2005. **77**(17): p. 5735-41.
9. Liu, J. and Y. Lu, Fast colorimetric sensing of adenosine and cocaine based on a general sensor design involving aptamers and nanoparticles. *Angew Chem Int Ed Engl*, 2005. **45**(1): p. 90-4.
10. Li and L.J. Rothberg, Label-Free Colorimetric Detection of Specific Sequences in Genomic DNA Amplified by the Polymerase Chain Reaction. *Journal of the American Chemical Society*, 2004. **126**(35): p. 10958-10961.
11. Wang, Z.D., J.H. Lee, and Y. Lu, Label-free colorimetric detection of lead ions with a nanomolar detection limit and tunable dynamic range by using gold nanoparticles and DNAzyme. *Advanced Materials*, 2008. **20**(17): p. 3263-3267.
12. Liu, C.-W., et al., Detection of mercury(ii) based on Hg<sup>2+</sup>-DNA complexes inducing the aggregation of gold nanoparticles. *Chemical Communications*, 2008(19): p. 2242-2244.
13. Wang, L., et al., Unmodified gold nanoparticles as a colorimetric probe for potassium DNA aptamers. *Chemical Communications*, 2006(36): p. 3780-3782.
14. Seferos, D.S., et al., Polyvalent DNA Nanoparticle Conjugates Stabilize Nucleic Acids. *Nano Letters*, 2008. **9**(1): p. 308-311.
15. Cheng, W., et al., Free-standing nanoparticle superlattice sheets controlled by DNA. *Nat Mater*, 2009. **8**(6): p. 519-525.
16. Tan, S.J., et al., Building plasmonic nanostructures with DNA. *Nature Nanotechnology*, 2011. **6**: p. 268-276.

### Chapter 3

17. Maye, M.M., et al., Switching binary states of nanoparticle superlattices and dimer clusters by DNA strands. *Nature Nanotechnol.*, 2010. **5**: p. 116-120.
18. Urzhumov, Y.A., et al., Plasmonic nanoclusters: a path towards negative-index metafluids. *Optics Express*, 2007. **15**(21): p. 14129-14145.
19. Nykypanchuk, D., et al., DNA-guided crystallization of colloidal nanoparticles. *Nature*, 2008. **451**: p. 549-552.
20. Auyeung, E., et al., DNA-mediated nanoparticle crystallization into Wulff polyhedra. *Nature*, 2014. **505**(7481): p. 73-77.
21. Cheng, W.L., et al., Probing in real time the soft crystallization of DNA-capped nanoparticles. *Angewandte Chemie International Edition*, 2010. **49**: p. 380-384.
22. Tan, S.J., et al., Crystallization of DNA-Capped Gold Nanoparticles in High-Concentration, Divalent Salt Environments. *Angewandte Chemie International Edition*, 2014. **53**(5): p. 1316-1319.
23. Park, S.Y., et al., DNA-programmable nanoparticle crystallization. *Nature*, 2008. **451**: p. 553-556.
24. Giljohann, D.A., et al., Oligonucleotide Loading Determines Cellular Uptake of DNA-Modified Gold Nanoparticles. *Nano Letters*, 2007. **7**(12): p. 3818-3821.
25. Peterson, A.W., R.J. Heaton, and R.M. Georgiadis, The effect of surface probe density on DNA hybridization. *Nucleic Acids Res*, 2001. **29**(24): p. 5163-8.
26. Brittain, W.J. and S. Minko, A structural definition of polymer brushes. *Journal of Polymer Science Part A: Polymer Chemistry*, 2007. **45**(16): p. 3505-3512.
27. Zhang, J., et al., Optimization of DNA Hybridization Efficiency by pH-Driven Nanomechanical Bending. *Langmuir*, 2012. **28**(15): p. 6494-6501.
28. Demers, L.M., et al., A Fluorescence-Based Method for Determining the Surface Coverage and Hybridization Efficiency of Thiol-Capped Oligonucleotides Bound to Gold Thin Films and Nanoparticles. *Analytical Chemistry*, 2000. **72**(22): p. 5535-5541.

### Chapter 3

29. Hill, H.D., et al., The role radius of curvature plays in thiolated oligonucleotide loading on gold nanoparticles. *ACS Nano*, 2009. **3**(2): p. 418-24.
30. Zwanikken, J.W., et al., Local Ionic Environment around Polyvalent Nucleic Acid-Functionalized Nanoparticles. *The Journal of Physical Chemistry C*, 2011. **115**(33): p. 16368-16373.
31. Campolongo, M.J., et al., Crystalline Gibbs Monolayers of DNA-Capped Nanoparticles at the Air–Liquid Interface. *ACS Nano*, 2011. **5**(10): p. 7978-7985.
32. Von White, G., F.S. Mohammed, and C.L. Kitchens, Small-Angle Neutron Scattering Investigation of Gold Nanoparticle Clustering and Ligand Structure Under Antisolvent Conditions. *The Journal of Physical Chemistry C*, 2011. **115**(38): p. 18397-18405.
33. Turkevich, J., P.C. Stevenson, and J. Hillier, A study of the nucleation and growth processes in the synthesis of colloidal gold. *Discussions of the Faraday Society*, 1951. **11**(0): p. 55-75.
34. Frens, G., Controlled Nucleation for the Regulation of the Particle Size in Monodisperse Gold Suspensions. *Nature*, 1973. **241**(105): p. 3.
35. Gilbert, E.P., J.C. Schulz, and T.J. Noakes, ‘Quokka’—the small-angle neutron scattering instrument at OPAL. *Physica B: Condensed Matter*, 2006. **385–386, Part 2**(0): p. 1180-1182.
36. Svergun, D., Determination of the regularization parameter in indirect-transform methods using perceptual criteria. *Journal of Applied Crystallography*, 1992. **25**(4): p. 495-503.
37. Kline, S., Reduction and analysis of SANS and USANS data using IGOR Pro. *Journal of Applied Crystallography*, 2006. **39**(6): p. 895-900.
38. Guinier, A. and G. Fournet, *Small-angle scattering of X-rays*. 1955: John Wiley and Sons.
39. Sears, V.F., Neutron scattering lengths and cross sections. *Neutron News*, 1992. **3**(3): p. 26-37.
40. Glatter, O., The interpretation of real-space information from small-angle scattering experiments. *Journal of Applied Crystallography*, 1979. **12**(2): p. 166-175.

### Chapter 3

41. Harroun, T.A., G.D. Wignall, and J.K. . Neutron Scattering for Biology., in Neutron Scattering in Biology. 2006, Springer-Verlag Berlin Heidelberg.
42. Chen, H., et al., Ionic strength-dependent persistence lengths of single-stranded RNA and DNA. Proc Natl Acad Sci U S A, 2012. **109**(3): p. 799-804.
43. Svergun, D.I., et al., Protein hydration in solution: Experimental observation by x-ray and neutron scattering. Proceedings of the National Academy of Sciences, 1998. **95**(5): p. 2267-2272.
44. Jiang, H.-R. and M. Sano, Stretching single molecular DNA by temperature gradient. Applied Physics Letters, 2007. **91**(15): p.154104-154106.

## Chapter 3

---

## **Chapter 4. Hairy Gold Micro/Nanostructure: Synthesis, Characterization and Application in Strain Sensors**

---



### **Part 1 Hairy Gold Nanorods: Synthesis, Characterization and Application in Strain Sensors**

#### 4.1 Introduction

Metal nanoparticles have exhibited intriguing size- and shape-dependent optical [1-4], electronic [5-7], catalytical [8-10] and magnetic [11-13] properties different from their corresponding bulk metals. Recently, it has also been demonstrated that percolation conductivities of nanoparticle assemblies are also strongly dependent on nanomorphologies, leading to their uses in transparent electrodes [14, 15] and wearable electronics [16-18]. Driven by these exciting size- and shape-dependent properties, a number of synthetic strategies have been developed over the past about 30 years, leading to the formulation of so-called 'nanoparticle periodic table' [19]. Despite of these encouraging progresses in synthesizing metallic nanoparticles [20-24], we are still far from the capability of constructing any arbitrary nanostructures in a well-controlled manner.

Here, we report on a new type of metallic nanoarchitectures made from hairy ultrathin gold nanowires and rigid gold nanorod core. Previously, seed-mediated growth of gold nanowires have been achieved on macroscopic surfaces such as silicon and trumpet shells [25]. Recently, this approach has also been extended to submicrometer-sized silica nanospheres, showing novel applications in surface enhanced Raman scattering [26] and nonenzymatic electrochemical biosensors [26]. In this work, we further demonstrate that this seed-mediated growth approach can also be extended to plasmonic gold nanorods, leading to formation of hairy gold nanorods (HG NRs).

## Chapter 4

### 4.2 Experimental Methods

#### 4.2.1 Materials

Gold (III) chloride trihydrate ( $\text{HAuCl}_4 \cdot 3\text{H}_2\text{O}$ ,  $\geq 99.9\%$ ), cetyltrimethylammoniumbromide (CTAB), sodium borohydride ( $\text{NaBH}_4$ ), silver nitrate ( $\text{AgNO}_3$ ), L-ascorbic acid (AA), tetraethyl orthosilicate (TEOS), (3-aminopropyl) trimethoxysilane (APTMS), 4-Mercaptobenzoic acid (MBA) were purchased from Sigma Aldrich. Thiol-functionalized polystyrene ( $M_n = 50\,000$  g/mol,  $M_w/M_n = 1.09$ ) was purchased from Polymer Source Inc. Ethanol was obtained from Merck KGaA. Ammonia hydroxide solution (28.0-30%) was purchased from Fisher Scientific). All chemicals were used as received unless otherwise indicated. Deionized water was used in all aqueous solutions, which were further purified with a Milli-Q system (Millipore). All glassware used in the following procedures was cleaned in a bath of freshly prepared aqua regia and rinsed thoroughly in MQ water prior to use. Nitrile rubber was brought from MEDiflex industries. Silver paste was purchased from Sigma Aldrich. Stainless thin conductive thread was purchased from Adafruit Industries.

#### 4.2.2 Methodology of Hairy Plasmonic Nanorods Synthesis

##### 4.2.2.1 Synthesis Gold Nanorods

The gold nanorods were prepared according to reported method [27, 28]. A brownish-yellow seed solution was prepared by mixing CTAB (5.0 mL, 0.2 M) and  $\text{HAuCl}_4$  (5.0 mL, 0.5 mM) followed by adding ice-cold  $\text{NaBH}_4$  (0.6 mL, 0.01 M). The seed solution was aged at 30°C before seeding to growth solution. Then, CTAB (5 mL, 0.20 M) and  $\text{HAuCl}_4$  (5.0 mL, 1.0 mM) were added to (0.2mL 4 mM)  $\text{AgNO}_3$  solution in sequence and with the addition of AA (0.08 mL, 0.08 M), the yellowish mixture became colorless and the growth solution was obtained. To

## Chapter 4

grow nanorod, 12  $\mu\text{L}$  of seed was added into the growth solution and aged at  $30^{\circ}\text{C}$  for two hours. The CTAB capped NRs were collected by centrifugation (7 000 rpm for 10 min) and washed with water twice, redispersed in 1 mL MQ water.

### 4.2.2.2 PEG Functionalization

The stabilization agent, CTAB, on the surface of the gold nanorods was replaced by mPEG-thiol through ligand exchange. An mPEG ( $M_w = 5000$ ) solution (1 mL, 20 mg/mL) was mixed with 1 mL nanorod solution to react 2 h. Then after washing with water 3 times to remove the non-reacting mPEG, the nanorods were redispersed in water (1.2 mL) for next silica coating.

### 4.2.2.3 Silica Coating of PEG Capped Gold Nanorods

A modified Stöber method [29, 30] was used to grow a silica shell of controlled thickness on the PEGylated gold nanorods. Briefly, 1.2 mL of PEG capped gold nanorods was mixed with 8 mL ethanol, and sonicated for 1 min, then 67  $\mu\text{L}$  ammonia solution was added to solution under vigorous stirring, followed by TEOS (8  $\mu\text{L}$ ) in ethanol (1 mL) dropwise added to the mixture. After stirring for 16 hours, the resulting samples were collected by centrifugation, washed with water 3 times and redispersed in 1 mL ethanol for amino functionalization. Functionalizing silica coated nanorod surface with APTMS. The amino-functionalized gold nanorod was prepared by mixing 1 mL silica coated gold nanorod with 4 mL 2% APTMS in ethanol for 1 hour, followed by washing with ethanol 3 times.

### 4.2.2.4 Synthesis Gold Seeds

0.147 mL 34 mM sodium citrate was added into conical flask with 20 mL  $\text{H}_2\text{O}$  under vigorous stirring. After 1 min, 600  $\mu\text{L}$  of ice-cold, freshly prepared 0.1M

## Chapter 4

NaBH<sub>4</sub> solution was added with stirring. The solution turned brown immediately. The solution was stirred for 5 min and then stored at 4 °C until needed.

### 4.2.2.5 Adsorption of Gold Seeds onto APTMS site

Firstly, the amino functionalized nanorod sonicated for 30 seconds and added to 5 mL AuNPs, then sit in room temperature for 6 hours for adsorption. The products were collected by centrifugation and then washed with water once, redispersed in MQ water as the nanorod seeds for nanowire growth.

### 4.2.2.6 Hairy Gold Nanorod Growth

The reaction of ratio at 12.5 of HAuCl<sub>4</sub> to MBA showed as following: 50 µL MBA (6.1mM) was firstly added into the water–ethanol (3:1, v/v) mixed solution under gently stirring. Then, 152 µL HAuCl<sub>4</sub> (25 mM) and 1 mL nanorod seeds were added to the solution in turn. Subsequently, after 1min ingredient mixed completely, AA (22 µL, 0.41 M) was added. Keep the reaction under stirring for 1 min, and take out to sediment down the hairy nanorod for further characterizations.

### 4.2.2 Strain Sensor Fabrication

The strain sensor was fabricated by the following procedure: nitrile rubber was first attached on a glass slide and patterned with polyimide masks (25 × 5 mm<sup>2</sup> rectangular pattern size). Then high concentrated hairy gold nanorod solution (50 µL) was drop casted onto the soft substrates and dried in fume cupboard. After the solution was dried, polyimide masks and glass side were removed. The electrical sheet resistance of hairy nanorod film reached to 59.5±14.4 KΩ sq<sup>-1</sup>. Then silver paste was deposited onto both ends of the hairy nanorod strips connected with flexible conductive threads. After the silver paste was dried (100

## Chapter 4

°C for 10 min on hot plate), polyvinyl alcohol (PVA) glue was deposited on top of silver paste and dried in ambient condition (30 min), which permanently sealed the hairy gold nanorod film to conductive thread.

### 4.2.3 Characterization

UV-Vis absorption spectra were recorded using an Agilent 8453 UV–Vis spectrometer. The shape and morphology of synthesis process were characterized by Scan electron microscopy (SEM) imaging and transmission electron microscopy (FEI Tecnai T20 Twin TEM) imaging. For TEM imaging, a drop of gold nanorod suspension was placed on copper-formvar grids and dry with a filter paper.

To test the strain-sensing characteristics, two ends of the samples were attached to motorized moving stages (THORLABS Model LTS150/M) then uniform stretching/releasing cycles were applied to the samples with a computer-based user interface (Thorlabs APT user).

## 4.3 Results and Discussion

### 4.3.1 Synthesis of HGNRs

In essence, the synthesis of HGNRs went through two seed-mediated growth processes. The first one was the known process for synthesis of monodispersed gold nanorods using soluble gold seeds and weak-binding ligand (cetyltrimethylammonium bromide). The second one was based on the nanorod-immobilized seeds and strong binding ligand (4-mercaptobenzoic acid). We found that HGNRs could form over a wider range of ratios (2.5 to 25) of gold precursor to ligand than that reported in the literature (ratio at 3), and the width of nanowire is dependent on the ratio. Furthermore, the HGNRs with the soft

## Chapter 4

'hairs' and rigid 'core' allowed for the fabrication of patches with controllable percolation conductivity networks, enabling the fabrication of elastic conducting patches as soft strain sensors with high stretchability and durability.

Figure 4.1 illustrates the synthesis of HGNRs. Briefly, CTAB stabilized gold nanorod were first synthesized following the well-known seed-mediated growth method [27, 28]. Next CTAB was partially replaced by thiolated polyethylene glycol (SH-PEG) via ligand exchange, which could promote selective coating of uniform silica shell by sol-gel reaction with tetraethyl orthosilicate (TEOS) the precursor. Then the silica shell was functionalized with amino groups by (3-aminopropyl) trimethoxysilane (APTMS) to enable the attachment of gold seeds by electrostatic forces. Finally, the seeds-tethered to gold nanorods were used to catalyze the growth of ultrathin gold nanowires using 4-mercaptopbenzoic acid as binding ligands and  $\text{HAuCl}_4$ /ascorbic acid as growth solution.

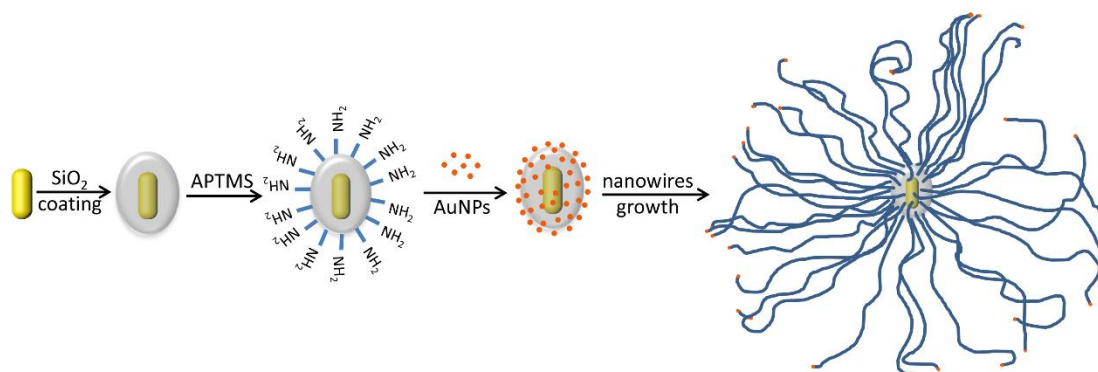


Figure 4.1 Schematic of hairy gold nanorods synthesis process.

The HGNR synthesis process was characterized stepwisely by transmission electron microscope (TEM) as shown in Figure 4.2. The monodispersed gold nanorods with an average length of  $53 \pm 2.1$  nm and width of  $16 \pm 0.4$  nm,

## Chapter 4

corresponding to an aspect ratio of  $3.2 \pm 0.2$ , were obtained (Figure 4.2a). Further sol-gel reactions led to a uniform silica coating of  $42 \pm 3.8$  nm as shown in figure 4.2b. After surface modification with amine moieties by APTMS, citrate-stabilized gold nanoparticle seeds could be tethered to silica shell surfaces (Figure 4.2c). These immobilized seeds could catalyze growth of long gold nanowires (Figure 4.2d).

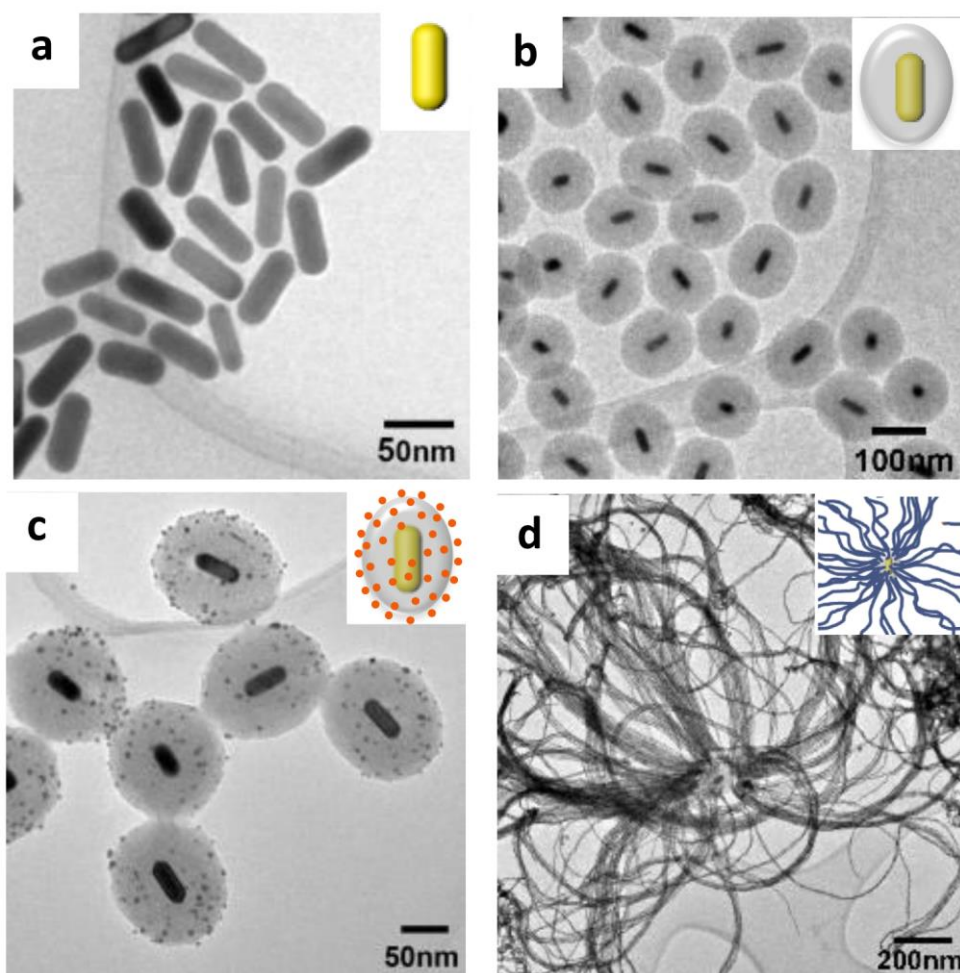


Figure 4.2(a, b, c, d) characterization of morphology of HGNRs synthesis TEM images of Au nanorods and silica coated nanorods.

## Chapter 4

### 4.3.2 UV-Vis Characterization of HGNRs

The evolution of HGNRs led to evident changes of plasmonic spectra (Figure 4.3a). The as-synthesized gold nanorods displayed two distinct localized surface plasmon resonance (LSPR) bands situated at 513 and 684 nm, corresponding to the transversal and longitudinal LSPR modes, respectively. To ensure uniform silica coating, modification of gold nanorods by polyethylene glycol was critical. The roles of PEG ligands are two-fold: to provide sufficient stability for them to be transferred into ethanol; to increase the affinity of silica to the gold surface [31]. The conformal coating of silica led to further red-shift of the longitudinal modes to 701 nm due to the increase of effective refractive index. The attachment of gold seeds caused further red shift of the plasmonic peak to 717 nm, due to the strong surface plasmonic coupling between seeds and nanorods [32, 33].

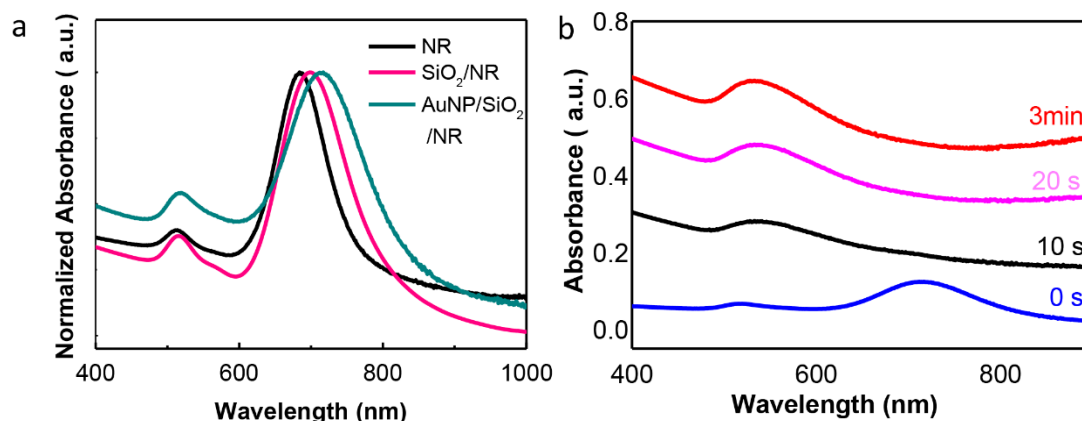


Figure 4.3 (a) UV-Vis spectra in process synthesis of HGNR, (b) Optical evolution and (c) UV-Vis spectra of HGNR growth.

The gold nanowires growth process was recorded in real time by UV-Vis spectra (Figure 4.3b). The blue line in Figure 4.3b is the AuNP/SiO<sub>2</sub>/NR seeds before

## Chapter 4

nanowires growth, which show two UV-Vis spectrum peaks at 518 nm and 717 nm. In the nanowire growth process, the longitudinal LSPR modes disappeared while the transversal LSPR modes become stronger, which can be attributed to the high aspect ratio of nanowires. We can also see that that the gold nanowires growth process was rapidly, within 10 seconds the longitudinal LSPR modes disappeared and transversal LSPR modes becomes the main peak. As growth time increase the transversal LSPR modes increased as well.

### 4.3.3 Morphological Characterization of HGNRs

The unique hairy morphologies of HGNR were confirmed by scanning electron microscope (SEM). Figure 4.4a shows a typical SEM image of HGNR, clearly demonstrating that long nanowires of around 1.5  $\mu\text{m}$  long and about 7.3 nm wide could be firmly tethered to gold nanorod surfaces. The firm attachment (Figure 4.4b) indicates the strong chemical binding interactions between nanowires and silica surfaces. The length of gold nanowires could reach up to  $\sim 15 \mu\text{m}$  long (Figure 4.5) and their number density could reach as high as  $140 \pm 17$  nanowires per nanorod.

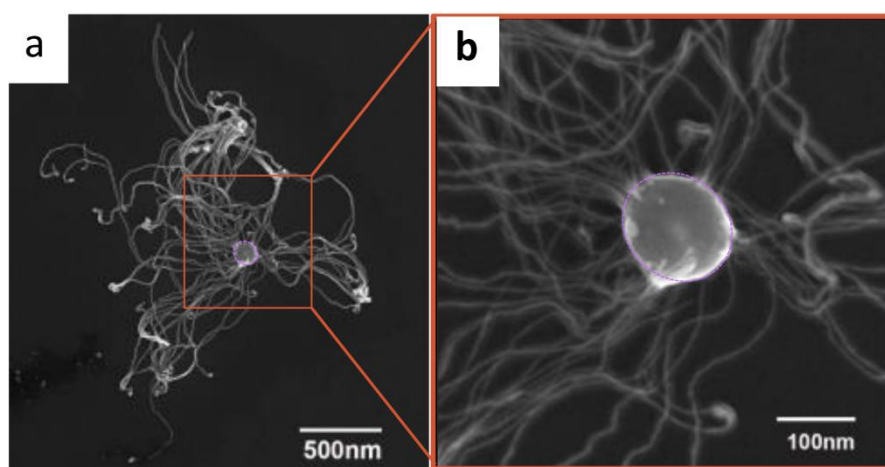


Figure 4.4 SEM images of (a) HGNR, (b) zoom in nanorod core.

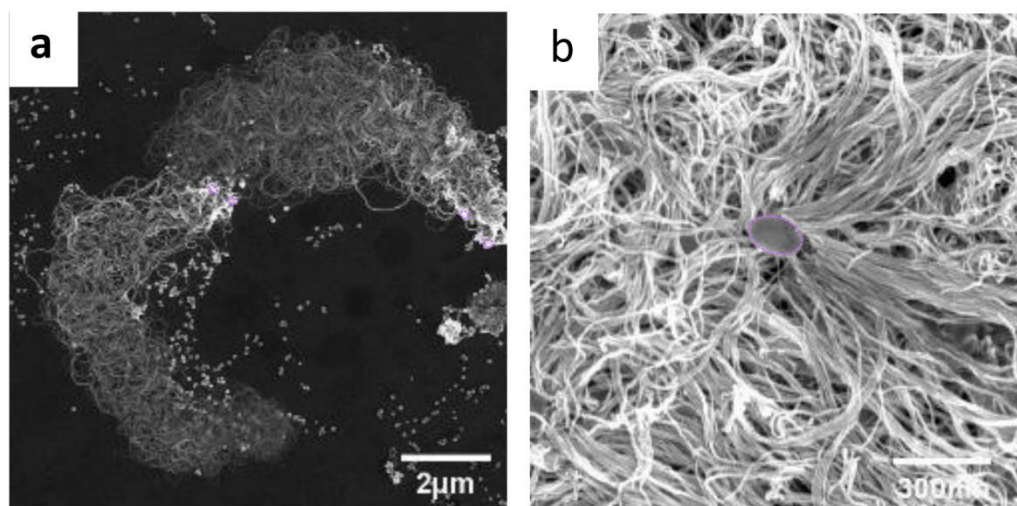


Figure 4.5 SEM images of HGNRs with (a) super long nanowires and (b) high density nanowires.

We further employed high-resolution transmission electron microscopy (HRTEM) to characterize a particular HGNR (Figure 4.6). HRTEM image in Figure 4.4c shows zoom in interface between silica shell and roots of nanowires, giving clear the crystal lattices with d-spacing of 0.235 nm and 0.202 nm corresponding to the (111) and (200) planes of face-centered cubic (FCC) gold the nanowires. The selected area electron diffraction pattern (SAED) of gold nanowires (inset of Figure 4.6c) with four bright rings corresponding to the (111), (200), (220) and (311) planes indicated that the entire nanowires was polycrystalline. The four continuous parts along a gold nanowire are also observed in Figure 4.7.

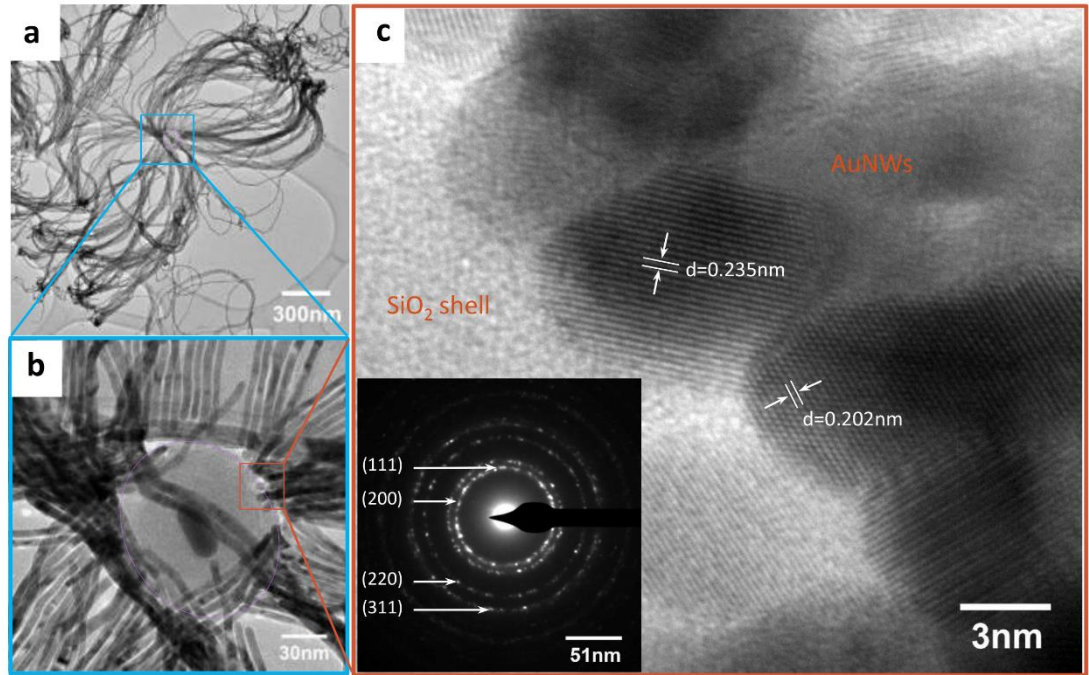


Figure 4.6 TEM images of (a) whole HGNR (b) NR core. (c) HRTEM image of silica shell and nanowire root interface region. Inset is a selected area electron diffraction pattern of HGNR, showing the (111), (200), (220) and (311) reflections of gold.

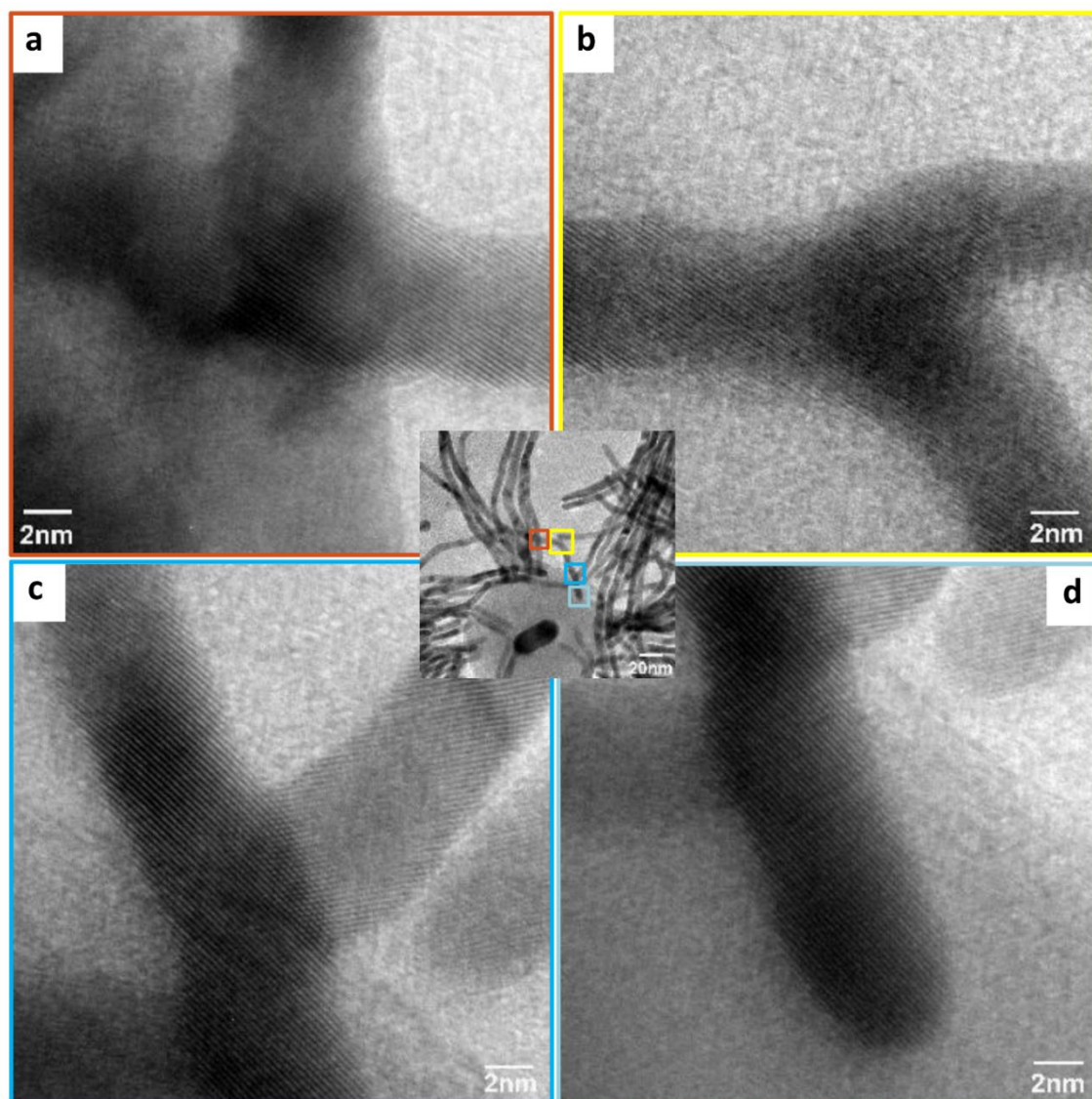


Figure 4.7 (a, b, c, d) HRTEM images of four continuous parts along a typical nanowire started at silica shell. Inset is the whole view of nanowire heightened high resolution parts.

#### 4.3.4 The Tuneable Morphology of HG NRs

In this study the length of nanowires could also be control by adjusting nanorod concentration. Four concentrations of nanorod (at 0.0033nM, 0.0067nM, 0.017nM, 0.034nM) were chose to grow different length hairy nanorod, and all

## Chapter 4

other growth conditions are same. From the SEM images (Figure 4.8 a, b, c and d), we can see that the length of nanowires decreased as the concentration of nanorod increased: the longest length of hairy nanorod is around  $1623 \pm 51$  nm, second length is  $221 \pm 12$  nm, the third one is  $134 \pm 26$  nm and the shortest is  $47 \pm 11$  nm. Interestingly, although the lengths of these nanowires were different, their widths were roughly the same.

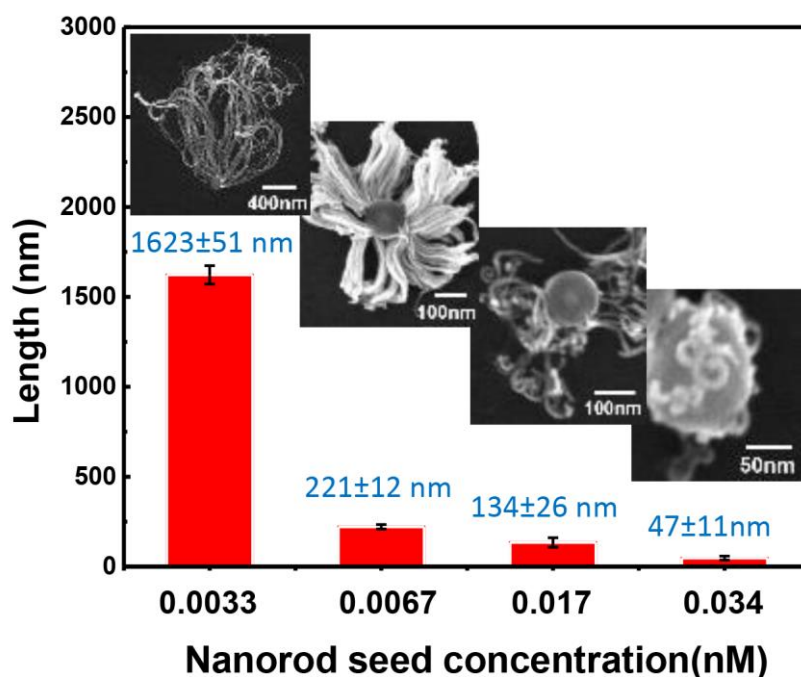


Figure 4.8 The length of nanowire tuned by the concentration of nanorod seed (0.034 nM, 0.017 nM, 0.0067 nM, 0.0033 nM). Insets are the corresponding SEM images of various length nanowires.

For the growth of hairy gold nanowires,  $\text{HAuCl}_4$  was the precursors and 4-Mercaptobenzoic acid (MBA) was the capping ligands. They were in a dynamic competition for the gold deposition and ligand binding[25]. More MBA usually gave thinner nanowires due to the fast ligand binding; in contrast, more  $\text{HAuCl}_4$

## Chapter 4

usually resulted in faster gold deposition speed, leading to the formation of thicker nanowires. An optimum ratio of 3 for  $\text{HAuCl}_4$  and MBA led to nanowires with a width of 6 nm was reported earlier [26]. In this study, we did a series of mole ratio of nanowire growth to investigate the relationship of  $\text{HAuCl}_4$  and MBA. Table 4.1 summarized concentration of gold precursor and ligand and their mole ratio in the growth solution. The red color highlights the ratio that nanowire can be formed, which was in the range of 2.5 to 25 (SEM images in Figure 4.9 b, c), and out of this range the nanowire cannot grow, like ratio at 1.25 and 75 showed in Figure 4.9 a, d. The reason for a limited ratio is mainly because of above dynamic competition theory. Our study also confirmed that the mole ratio determines the width of nanowire. With ratio increased from 2.5 to 3, 12.5 and 25, nanowire width increased from 5 nm, 5.5 nm, 7.3 nm and 9 nm respectively.

Table 4.1 The concentrations of gold precursor ( $\text{HAuCl}_4$ ) and ligand (MBA) and their mole ratios in the growth solution.

$\frac{\text{HAuCl}_4}{\text{MBA}}$ Ratio MBA( $\mu\text{M}$ ) $\text{HAuCl}_4(\text{mM})$	2.4	1.7	0.85	0.43	0.22
340	7	5	2.5	1.25	0.6
170	14	10	5	2.5	1.25
70	35	25	12.5	6.2	3.1
35	70	50	25	12.5	6.25
18	140	100	50	25	12.5

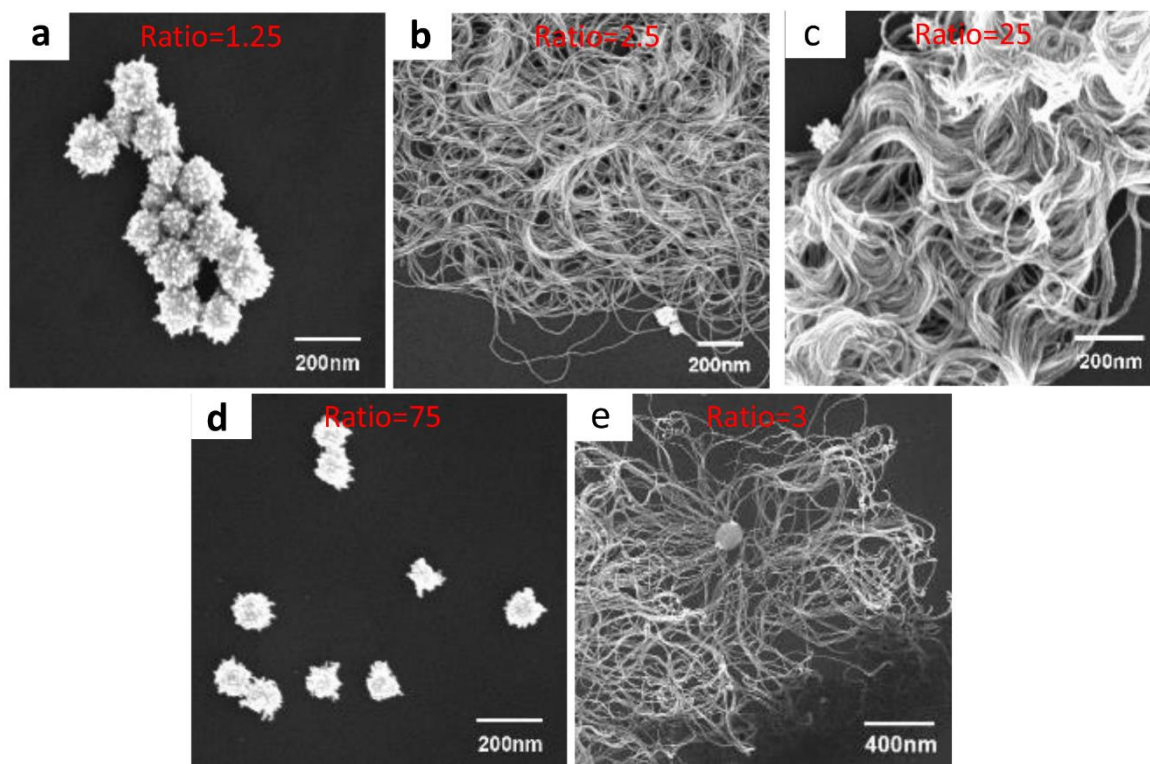


Figure 4.9 SEM images of gold nanowires grown at different mole ratio of  $\text{HAuCl}_4$  to MBA. The molar ratio of  $\text{HAuCl}_4$  and MBA is at (a) 1.25, (b) 2.5, (c) 25, (d) 75 and (e) 3.

In addition to the mole ratio of  $\text{HAuCl}_4$  and MBA, their concentration also played an important role in the growth of HGNRs. In our study we found that even  $\text{HAuCl}_4$  and MBA was in the ratio range of 2.5 to 25, it still could not form nanowires at too low or too high concentrations. The reasonable explanation of this phenomenon is that the concentration of  $\text{HAuCl}_4$  and MBA are not in optimum condition. As table showed, the nanowires can grow at the  $\text{HAuCl}_4$  concentration between 0.43 to 1.7 mM, and the MBA concentration between 35 to 170  $\mu\text{M}$ . Out of these concentrations, even the ratio was in the range, the nanowires still cannot growth. In the report  $\text{HAuCl}_4$  is at 1.7mM and MBA is at 550  $\mu\text{M}$  [25], the reason why the concentration in report is higher than ours is that nanowire

## Chapter 4

formed on the nanoscale colloidal template, the optimum concentration helps the nice HGNR structure formed.

Similar to previous report [25], the presence of silica was critical for the formation of gold nanowires. As shown in Figure 4.10, only 30 nm nanoparticles with worm shape obtained under some conditions with Figure 4.4, and the nanoparticles size around 30nm.

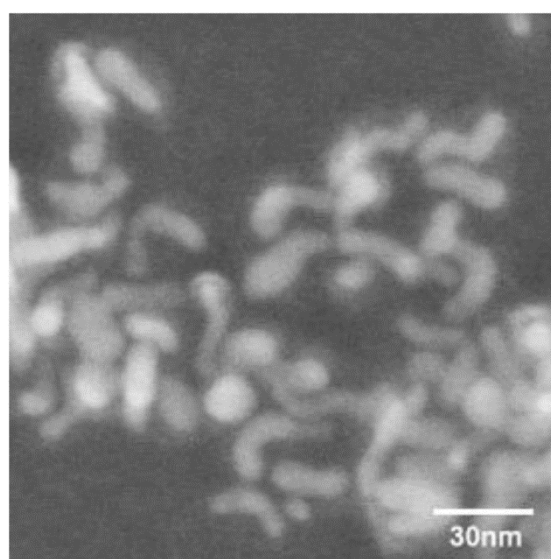


Figure 4.10 SEM image of nanoparticles obtained from seed growth without silica substrate, under otherwise the same reaction conditions as for Figure 4.4.

### 4.3.5 Application of HGNRs in Strain Sensor

The unique soft and elastic nanowires around gold nanorod cores allowed us to use HGNRs as a new conducting building block for stretchable sensors, which require the integration of outstanding electrical conductivity with elastic mechanics. To prove this, we drop casted HGNRs on a thin nitrile rubber sheet substrate to form a dark gold nanopatch. Typically, the nanopatch had a sheet resistance of  $59.5 \pm 14.4 \text{ K}\Omega \text{ sq}^{-1}$  after repeated dip-coating process for 10 times.

## Chapter 4

To assess the ability of sensor as a strain sensor, strain responsive tests were carried out at a current of 1V with varied strain. Figure 4.11b shows strain-induced relative resistance responses over three cycles of applied strain from 1%, 5% and 10%. The overall electrical response increased with increasing strains. HGNR-based sensors also exhibited high durability. Figure 4.11c is the plot of durability test under a cyclic strain of 0%-5%-0% at a frequency of 0.5 Hz. The resistance change curves were recorded for 1,000 cycles, and 50 cycles of data was presented in each 250 cycles recording. The stable and reproducible responds in durability test demonstrated the high durability of HGNR sensors.

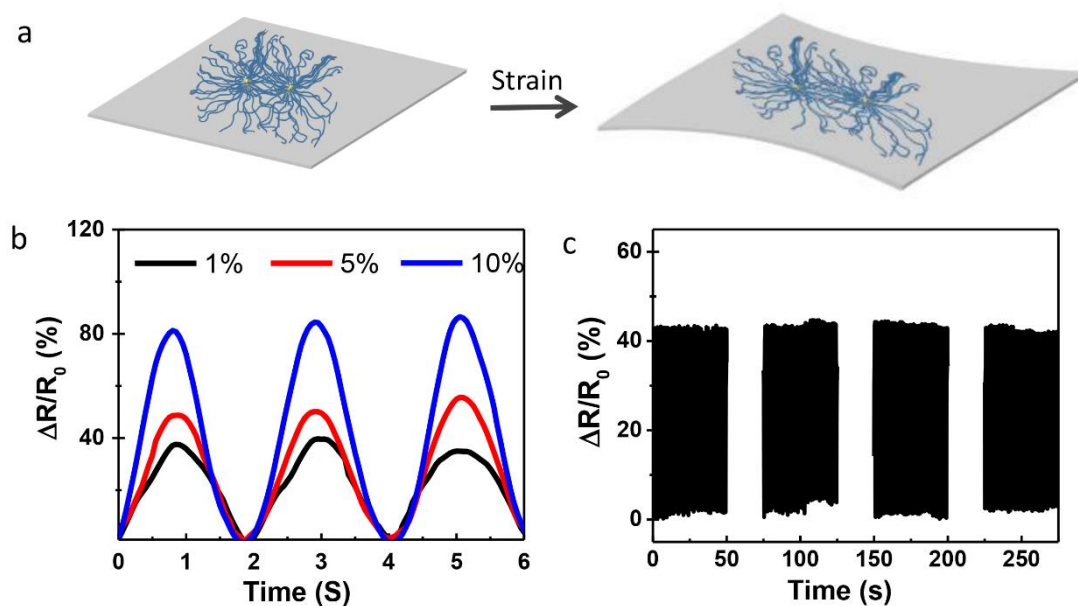


Figure 4.11 (a) possible mechanism of HGNR film before and under strain. (b) Resistance-time characteristics of the sample's stretchability test for three applied strain. (1V, 0.5 Hz) (c) The durability test under a strain of 5% at a frequency of 0.5 Hz.

The excellent performance indicated high elasticity of HGNR film and their strong adhesion to nitrile rubber support. This property is attributed to unique structures

## Chapter 4

of HGNR with nanorod core in middle radical wrapped high aspect ratio of over 200 nanowires crossing at lengthways and transverse direction. Such unique structural features made HGNR films to work as mesh film, exhibiting high elasticity. Furthermore, the stability of the sensor was tested in 30 days. The sensor film was put in a petri dish in ambient condition without any further sealing process, but the resistance did not show any evident fluctuations. The high stable nanowire is attributed by the capping molecules (MBA), which form a compact layer on the metal surface during nanowire growth, and also prevented oxidization at air conditions.

### 4.4 Conclusion

In summary, a new type of metal nanoarchitectures – hairy gold nanorods were successfully obtained by the two-step seed-mediated growth processes. We could obtain hairy gold nanowires with a ratio of  $\text{HAuCl}_4$  to MBA from 2.5 to 25, which is much wider region than literature report. What is more, width of nanowires would be controlled by the ratio, and width changed from 5nm to 9nm in this ratio range. We could control the length of nanowires from 47 nm to 15  $\mu\text{m}$ , simply by adjusting amount of nanorod. The unique hairy high-aspect-ratio gold nanowires tethered to concentric nanorod allowed for constructing flexible and stretchable percolation conductivity network. This conductive network could be used as high performance piezoresistive strain sensors with high stretchability and durability.

### **Part 2 Hairy Gold Bacteria: Synthesis and Characterization**

#### 4.5 Introduction

Building plasmonic structure particles has been a subject of increased interest over the past few years. Variety of morphologies and sizes of plasmonic structures have been synthesized [34]. A fascinating aspect of plasmonic nanoparticles is that their optical properties that are strongly affected by structural parameters such as size and shape, as well as material composition and the surrounding dielectric environment[35, 36]. The origin of surface Plasmon resonance (SPR) is from the coherent collective oscillations of conduction electrons upon interaction with incident light [37].

Hollow structure nanoparticles are novel class of nanostructures with hollow interiors, which can be applied as nanocontainers for drug delivery and catalysis [38, 39]. Due to the hollow property of these materials, hollow structure nanoparticles have the advantages of relatively low densities compared to their bulk material counterparts, which can be applied in fillers [40]. Because of the plasmonic properties of noble metal nanoparticles, hollow structures of these nanoparticles are particularly interested and investigated. Besides the advantages of hollow structures, hollow plasmonic structure also has the properties of plasmonic structures.

In this project a novel plasmonic microparticle was tried to build with capsule structure. However capsule structure plasmonic particles cannot be easily obtained by chemical synthesis process. Biomaterials as an untraditional materials are attractive many attention and intensively study recently decades. Fabrication technique of biomimetic structures cover broad interdisciplinary field

## Chapter 4

including biology, chemistry and materials science. So far an extensive range of cells are being employed in fabrication of requiring surface functionalization, including virus[41, 42], bacteria[43-47], yeast[48-50], human cell lines[51, 52], and even multicellular species[53, 54]. Biological cells own variety of morphologies and sizes, which consider as prefect templates for the deposition of functional nanomaterial. Every kind of biological cell possesses their unique morphologies, which is formed by nature and cannot be replaced by other methods. This template is easily acquired by simply biological method, what's more, the morphology of cells can still keep when they reproduce by million and billion times. As the *E.coli* bacteria have the morphology of capsule structure, therefore bacteria was employed as the template to synthesis the capsule structure plasmonic nanoparticle in the project.

The metal for synthesis plasmonic structure can be Au, Ag, and Cu. In this project Au was choose nanoparticles as the candidature to synthesis the capsule structure plasmonic structure. The reason choosing Au nanoparticles is because it is chemically inert [55], therefore the chemical stability of Au is very good. In addition, Au nanoparticles are biocompatible [56], if successfully synthesized the capsule plasmonic structure, it can be used for drug delivery.

In this project the first question need to be answered is that whether gold nanoparticles can coat on the surface of bacteria. This is the most basic question need to be addressed in this project. If the Au coating is successful, whether Au coating can be controlled? Finally it is needed to understand the fundamental relationships between structures and functions. We will apply this novel

## Chapter 4

plasmonic hairy bacteria for application of surface-enhanced Raman scattering (SERS) sensor and DNA diagnostics and drug delivery.

### 4.6 Experimental Methods

#### 4.6.1 Synthesis of Hairy Plasmonic Bacteria

##### 4.6.1.1 Bacteria Culture

The *E. coli* DH5 $\alpha$  was used in this study that kindly provided by Dr. Charles Ma from School of Biomedical Science, Monash University, Melbourne, Australia. The *E. coli* DH5 $\alpha$  bacteria were grown on sterile Luria–Bertani (LB) agar petri plates at 37°C for colonial growth. After an overnight incubation, single colony of *E. coli* was picked up from the plate and transferred to 25 mL LB liquid media. This culture was incubated at 37°C with shaking. After overnight incubation, bacteria were harvested and measured OD600 to determine the concentration. Then bacteria were washed five times with 0.9 w/v% sterile sodium chloride (NaCl) aqueous solution before coating.

##### 4.6.1.2 Coating *E. coli* Bacteria with SiO<sub>2</sub>

SiO<sub>2</sub> was coated onto the surface of *E. coli* bacteria following the Stöber method [57]. First NaCl solution washed bacteria were suspended in Milli-Q (MQ) water for SiO<sub>2</sub> coating. *E. coli* bacteria, ammonia solution (2.0 M in ethanol, Sigma, USA) and Milli-Q water were added to a conical flask and sonicated briefly (1 min) to disperse the bacteria evenly. Then desired amount of ethanol and tetraethyl orthosilicate (TEOS, Sigma, USA) were added to initiate the SiO<sub>2</sub> growth on the bacteria surface. The reaction was performed at room temperature under continuous agitation. After three days of reaction, the coated bacteria samples were collected by centrifugation, followed by washing with ethanol and

## Chapter 4

finally suspended in ethanol. The total amount of reaction solution was 10mL, and final experimental conditions were [*E. coli* bacteria] =  $8.2 \times 10^8$  cells/mL, [TEOS] = 0.1 mol/L, [NH<sub>3</sub>] = 0.8 mol/L, and [H<sub>2</sub>O] = 1.0 mol/L.

### 4.6.1.3 Functionalization of Bacteria@SiO<sub>2</sub> Surface with APTES

To assemble gold seeds onto the silica shell, the surface of the silica shell need to modified with amino group firstly. Functionalization of Bacteria@SiO<sub>2</sub> Surface with APTES was followed same method as 4.2.2.3.

### 4.6.1.4 Synthesis of Au Nanoparticle Seeds

Synthesis of Au nanoparticle seeds was followed method 4.2.2.4.

### 4.6.1.5 Attachment of Au Nanoparticle Seeds on APTES-Functionalized Bacteria@SiO<sub>2</sub>

0.1 mL of APTES/ SiO<sub>2</sub>/bacteria dispersed in ethanol was added to excess of Au nanoparticles (5 mL Au nanoparticle seeds colloid solution). The mixture solution was stirred for 2 hour. After which the mixture was centrifuged and wash by MQ water to remove the non-attached Au nanoparticles. The Au/APTES/SiO<sub>2</sub>/bacteria were dispersed in MQ water.

### 4.6.1.6 Growth Au Nanowires

The gold nanowires growth was modified from a gold forest method. In this study, 4-Mercaptobenzoic acid (MBA) was employed as a strong binding ligand for the growth of Au nanowires. 5  $\mu$ L desired concentration of MBA was added to a conical flask containing 1.2 mL absolute ethanol with vigorously stirring, followed by addition of 3.2 mL MQ water and 10  $\mu$ L Au/APTES/ SiO<sub>2</sub>/bacteria. After 1 min of mixing, desired amount of HAuCl<sub>4</sub> and reducing agent L-ascorbic acid was

## Chapter 4

added to initiate the growth of Au nanowires. The growth reaction was quick, after 4 min of reaction, samples were centrifuged and washed by MQ water, after which the sample was resuspended in MQ water for characterization.

### 4.6.2 Nanowire Length Control by MBA

Au/APTES/SiO<sub>2</sub>/bacteria were grown in fixed HAuCl<sub>4</sub> (0.425 mM) and L-ascorbic acid (1.025 mM) solution, but in different MBA (binding ligand) concentrations. For the MBA length control study following MBA concentrations was tried: 27.5  $\mu$ M, 11  $\mu$ M, 5.5  $\mu$ M, and 2.75  $\mu$ M. Au nanowire length was characterized by SEM.

### 4.6.3 Nanowire Size Control by HAuCl<sub>4</sub> and L-ascorbic Acid

Au/APTES/SiO<sub>2</sub>/bacteria were grown in fixed MBA solution, but in different concentration of HAuCl<sub>4</sub> and L-ascorbic acid solution. For the Au nanowires size control study growth solution was tried the following three concentration combination of HAuCl<sub>4</sub> and L-ascorbic acid: HAuCl<sub>4</sub> (0.85 mM) and L-ascorbic acid (2.05 mM), HAuCl<sub>4</sub> (0.43 mM) and L-ascorbic acid (1.03 mM), HAuCl<sub>4</sub> (0.21 mM) and L-ascorbic acid (0.51 mM). The Au nanowire length was characterized by SEM.

### 4.6.4 AuNP Seeds Density Control

For the AuNP seeds density control, experiment followed the protocol of 4.1.5. The gold seeds colloid solution used for this study was diluted to  $2.93 \times 10^{14}$ ,  $2.93 \times 10^{13}$ ,  $2.93 \times 10^{12}$ ,  $2.93 \times 10^{11}$  particles/mL. After attachment of Au nanoparticle seeds on APTES/SiO<sub>2</sub>/bacteria, experiment condition was followed the protocol of 4.1.6 for the growth of Au nanowires.

## Chapter 4

### 4.6.5 Growth Time Control

In the time control study, all the other reaction conditions were kept same. Normally the Au nanowires growth reaction is 4 min, here growth reaction time was set at 0, 1, 5, 15 min, and then samples were centrifuged and washed by MQ water, after which the sample was resuspended in MQ water for characterization.

### 4.6.6 Characterization

Synthesized bacteria@SiO<sub>2</sub> was coated with 2 nm thickness of Au in a vacuum atmosphere using sputter coater (K550X). The morphology of uncoated bacteria, bacteria@SiO<sub>2</sub>, Au/APTES/SiO<sub>2</sub>/bacteria, AuNWs/APTES/SiO<sub>2</sub>/bacteria were characterized by optical microscope (Nikon, eclipse Ti-U), scanning electron microscope (SEM, JEOL JSM-840A) and transmission electron microscopy (TEM, Philips CM20). UV-Vis spectra of samples were recorded at room temperature using Agilent 8453 UV-Vis Spectrophotometer.

## 4.7 Results and Discussion

### 4.7.1 Synthesis of Hairy Plasmonic Bacteria

#### 4.7.1.1 Bacteria Culture

In this study, *Escherichia coli* (*E. coli*) DH5 $\alpha$  strain was employed as the biological template. One reason for choosing bacteria as template is because the morphology of bacteria is well-defined, it won't change too much between individuals, so shapes of final products was can be controlled. Another reason for employing *E. coli* for study is that the doubling time for *E. coli* is only 20 minutes, so sufficient biological template can be easily got in a short time. In

## Chapter 4

addition, *E. coli* DH5 $\alpha$  lacks genes for typical *E. coli* pathogenicity factors, so it is safe to be employed as template for study.

### 4.7.1.2 Coating *E. coli* bacteria with SiO<sub>2</sub>

In the coating process, the amount of water is a key factor that determines the success of the coating. In study, it was found when the amount of water is excess in the reaction system, there will be unwanted SiO<sub>2</sub> nanoparticles in the final product (Figure. 4.12). These unwanted SiO<sub>2</sub> nanoparticles will be suspended in the solutions or attached on the surface of SiO<sub>2</sub> shell coated bacteria. This is mainly because that TEOS hydroxylation happens in the presence of water and followed by nucleation, if water is desired amount the nucleation process will happen in the surface of the bacteria. However, if the water amount is excess, the nucleation process will happen in the solution, and unwanted SiO<sub>2</sub> nanoparticles will present in the final product.

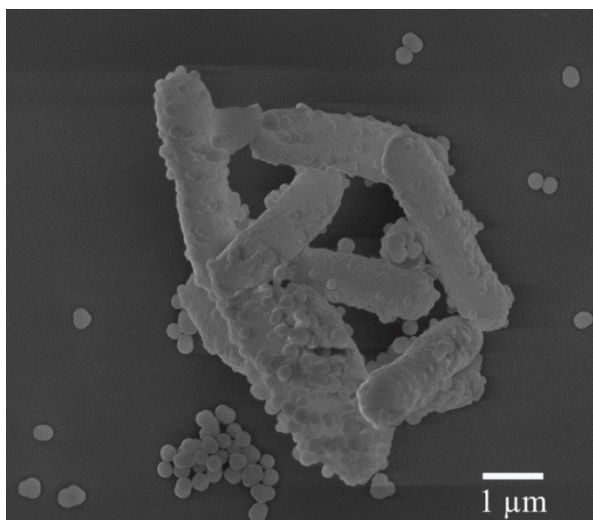


Figure 4.12 When the amount of water is excess in the reaction system, there will be unwanted SiO<sub>2</sub> nanoparticles in the final product.

## Chapter 4

After 72 hour of coating reaction, *E. coli* DH5 $\alpha$  bacteria were coated by SiO<sub>2</sub> shell. The Bacteria@SiO<sub>2</sub> was observed by the SEM. The SEM image (Figure. 4.13) shows that the synthesized particles retained the rod-shaped morphology of the *E. coli* bacterial cells, with a length around 2  $\mu$ m and 0.7  $\mu$ m in diameter. From the SEM image (Figure. 4.13) it is also display that SiO<sub>2</sub> was smoothly coated onto the surface of the bacterial surface. These results demonstrate that the coating of SiO<sub>2</sub> shell on the bacterial surface was successfully.

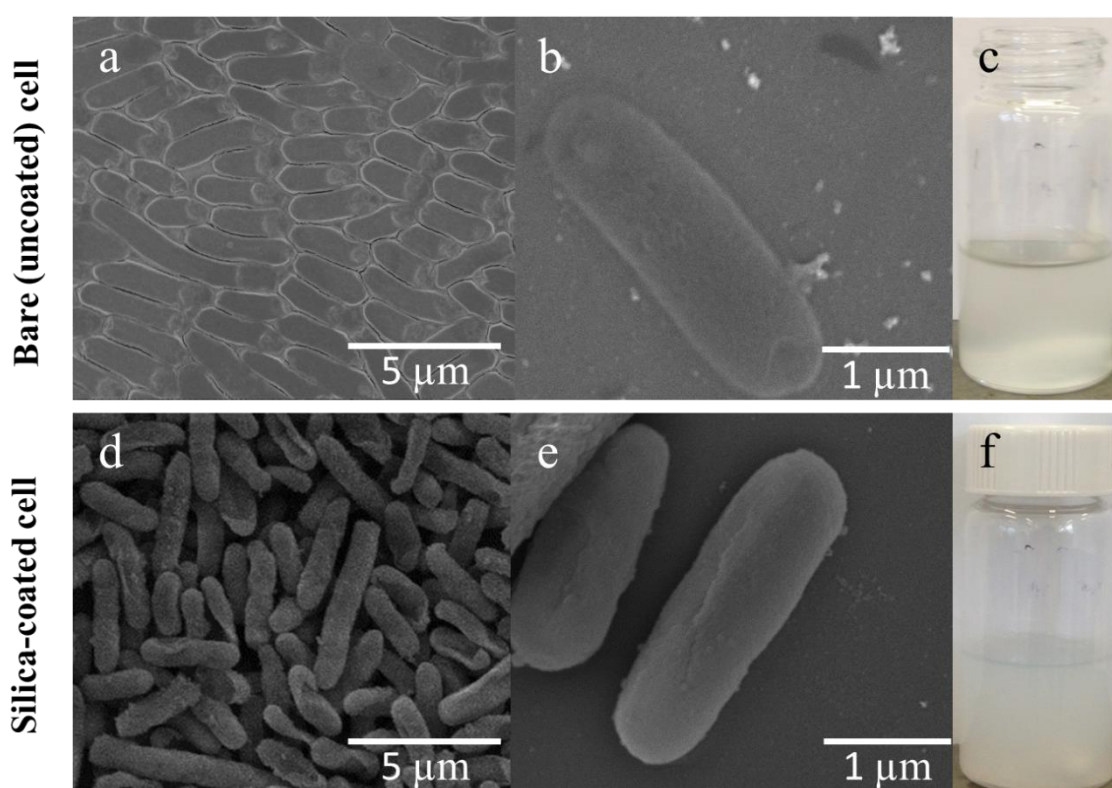


Figure 4.13 *E. coli* cell surface coated with silica. SEM images of: a, b) bare (uncoated), and d, e) silica-coated cell. The corresponding photographs of the coating at the initial and final stage of reaction: c) bare (uncoated), and f) silica-coated cell.

## Chapter 4

Although bacteria itself also have the hollow structure, it cannot preserve for long time. In study, it was found that after 5 days, the uncoated bacteria cell cannot keep intact shape (Figure. 4.14). While silica-coated cell still retained the intact morphology of the *E. coli* bacterial cells. The coating offers a way to preserve the capsule structure of the bacteria.

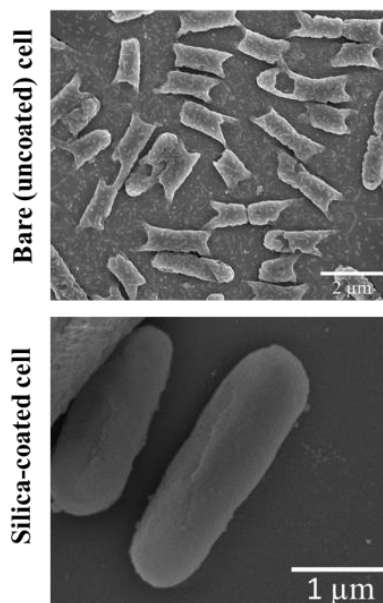


Figure 4.14 SEM images of bare (uncoated) bacteria cell and silica-coated cell after 5 days.

### 4.7.1.3 Functionalization of Bacteria@SiO<sub>2</sub> Surface with APTES

In order to attach Au on the silica surface, APTES serves as a bridge in this study. APTES forms a covalent bond with SiO<sub>2</sub> through the hydroxyl group and leave the SiO<sub>2</sub> surface becomes NH-terminated, which can be served for Au attachment (Figure. 4.15).

## Chapter 4

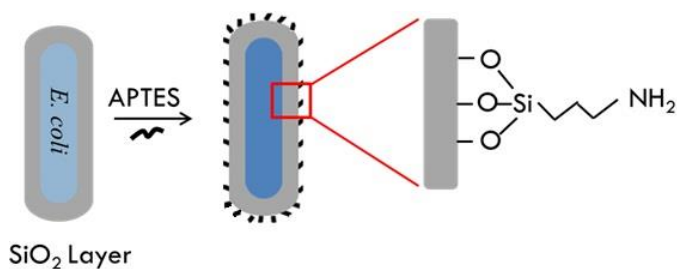


Figure 4.15 Schematic of functionalization bacteria@SiO<sub>2</sub> surface with APTES.

### 4.7.1.4 Synthesis of Au Nanoparticle Seeds

The gold seeds used to assemble on silica surface need to be synthesized fresh. The synthesized Au colloidal nanoparticles were examined by UV-Vis spectrum, which produces a strong surface Plasmon band at 508 nm (Figure. 4.16).

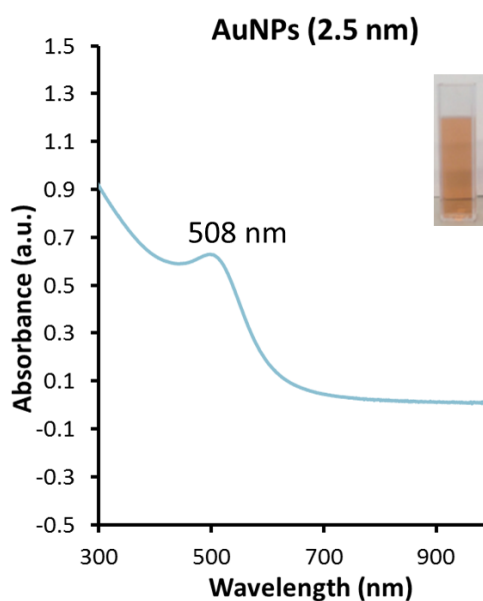


Figure 4.16 UV-Vis spectrum of 2.5 nm Au seed nanoparticle. The corresponding photographs of Au colloidal nanoparticles (inset) confirms UV-Vis spectra results.

## Chapter 4

### 4.7.1.5 Attachment of Au seeds Nanoparticle on APTES-Functionalized Bacteria@SiO<sub>2</sub>

Au NPs was attached on the silica surface by mixture of Au NPs (Figure. 4.17a) and APTES/Silica/Bacteria (Figure. 4.17b). After 2 hour of reaction, the Au/APTES/Silica/Bacteria were obtained by centrifuging (3500 rpm, 5 min). A red-colored pellet was observed at the bottom of the tube (Figure. 4.17c). After washing by MQ water, this pellet was redispersed in water (Figure. 4.17d, e). Since low speed centrifugation cannot spin down 2.5 nm Au NPs. The red color means Au NPs were deposited on the silica shell surface after 2 hour of reaction. From the SEM image (Figure. 4.18) it is also deduce that gold seeds have been attached on the surface of silica shell. Because Au/APTES/Silica/Bacteria can be observed clearly by SEM without coating a conductive layer on the specimen surface whereas APTES/Silica/Bacteria specimen need coating conductive layer to be observed.

In addition, the attachment of Au nanoparticle seeds on APTES/Silica/Bacteria was also confirmed by TEM images. By comparing the TEM images of Silica/Bacteria (Figure. 4.19a) and Au/APTES/Silica/Bacteria (Figure. 4.19b, c), it is clearly see some small round dots on the surface of the Au/APTES/Silica/Bacteria. This suggested that Au nanoparticles were attached on the surface of silica shell.

## Chapter 4

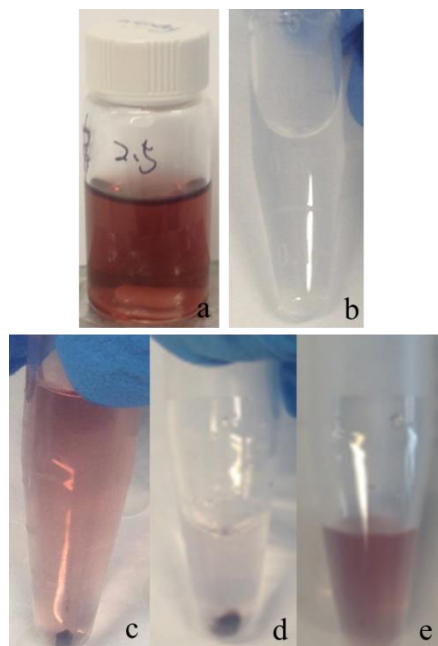


Figure 4.17 Photographs of the process of Au. (a) AuNPs, (b) APTES/Silica/Bacteria. After 2 hour of reaction, the Au/APTES/Silica/Bacteria were obtained by centrifuging (c). This pellet was redispersed in water (d, e).

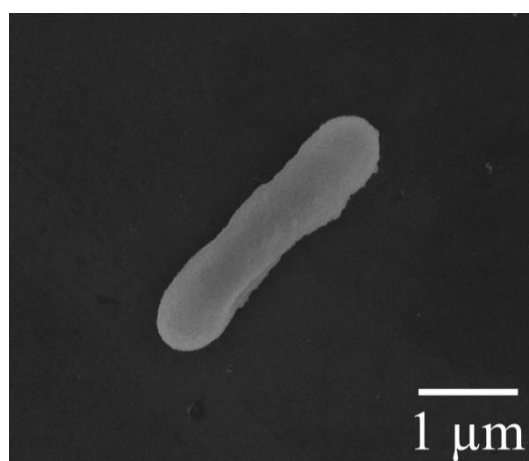


Figure 4.18 SEM image of Au/APTES/Silica/Bacteria.

## Chapter 4

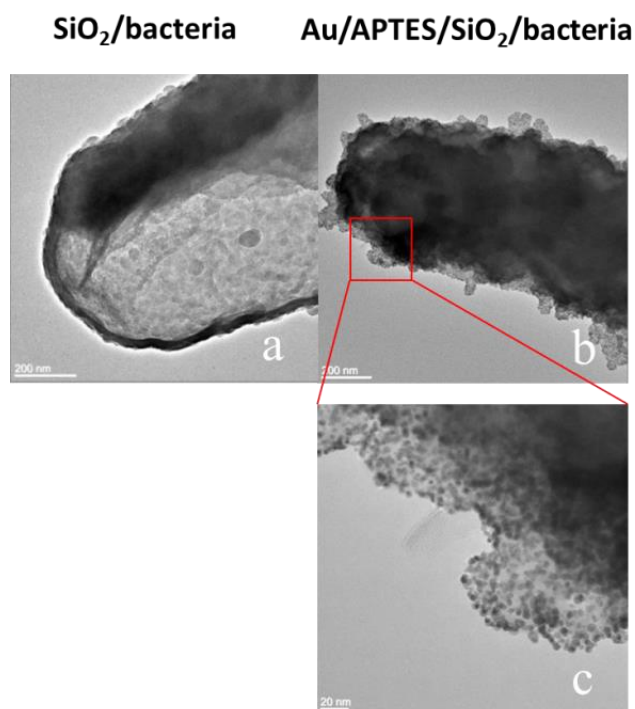


Figure 4.19 TEM images of: a) silica-coated bacteria, b, c) Au/APTES/Silica/Bacteria.

### 4.7.1.6 Growth of Au Nanowires

The growth of Au nanowires was modified from Chen's method [59]. However, their method cannot be used to grow Au nanowires in the solution. Here their method was modified by introducing silica shell coated bacteria as a substrate in study. In this growth mode, silica shell was used as the gold nanowire growth substrate to allow gold nanowires formed on its surface. This is a critical part of the nanostructure, as the gold seed cannot grow nanowires without the substrate. During the nanowires growth, the reaction solution color changed colorless to red then end with dark blue at the final stage of the reaction (Figure. 4.20), which is a typical plasmonic color shift.

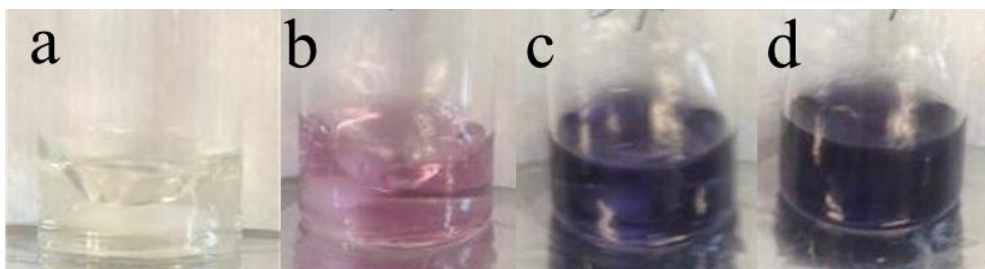


Figure 4.20 Process of Au nanowires growth. (a) Before the start of the reaction, the solution is colorless. After 5 s (b), 20 s (c), and 30 s (d), the reaction solution color changed from colorless to dark blue.

From the SEM image (Figure. 4.21) it was found the length of Au nanowire is more than 100 nm long. It is also found that these Au nanowires entangled together at the outer layer, however in the inner layer Au nanowires grow very straight and parallel to each other (Figure. 4.21). Chen [59] pointed out that Au growth occurred at the Au-substrate interface after the seed was elevated from the substrate. In this study, it was found the Au nanowires only entangled together at the outer layer, which confirmed this growth mechanism same as literature reported.

In this Au nanowire growth reaction, Au nanowires are grown from the inner Au seed to the outer layer. The growth is completed by two key components in the reaction. The first is the binding ligand MBA, which serves as cement in the nanowire growth. The second key components are the  $\text{HAuCl}_4$  and reducing agent L-ascorbic acid, which works for the Au deposition and serves as blocks in the nanowire growth. In study, morphology of Au nanowires can be controlled by adjusting the concentration of these key components in the nanowires growth system. This will discuss in the following sections.

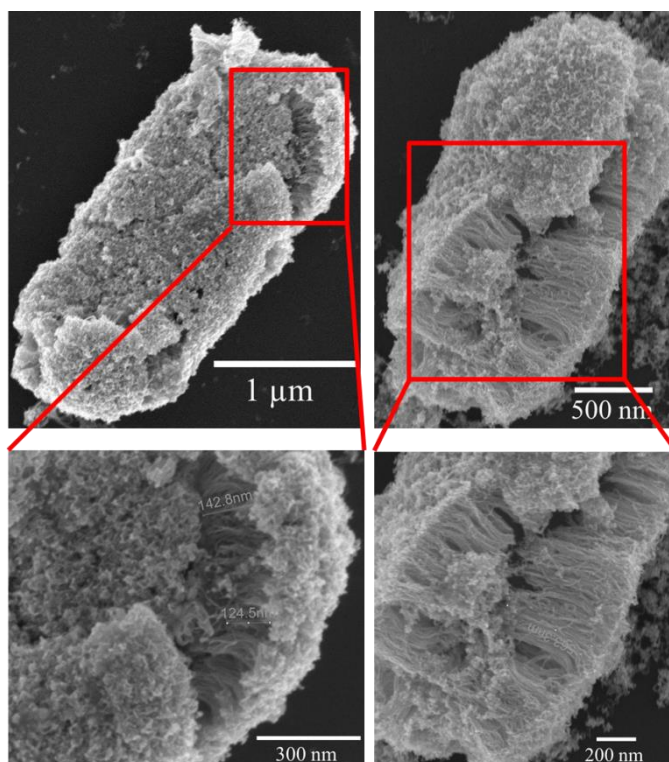


Figure 4.21 SEM image of AuNWs/APTES/Silica/Bacteria. It can see that Au nanowires entangled together at the outer layer, however in the inner layer it was found the Au nanowires grow very straight and parallel to each other.

#### 4.7.2 Nanowire Length Control by MBA

In this study, the Nanowire length can be controlled by change MBA concentration. Keeping  $\text{HAuCl}_4$  and L-ascorbic acid at 0.425 and 1.205 mM, the concentration of MBA was lowered to 27.5, 11, 5.5, and 2.75  $\mu\text{M}$ , respectively. From the SEM images (Figure. 4.22) it is observed that as the concentration of MBA was decreased, Au deposited on Au seed-shell interface formed from long nanowires to island. This clearly suggested that the length of nanowires can be controlled by concentration of binding ligand MBA. The mechanism for the nanowire length control by MBA is mainly because as the concentration of the ligand was increasing, the power was relatively higher to push nanowire go upwards growing and absorbs Au deposition.

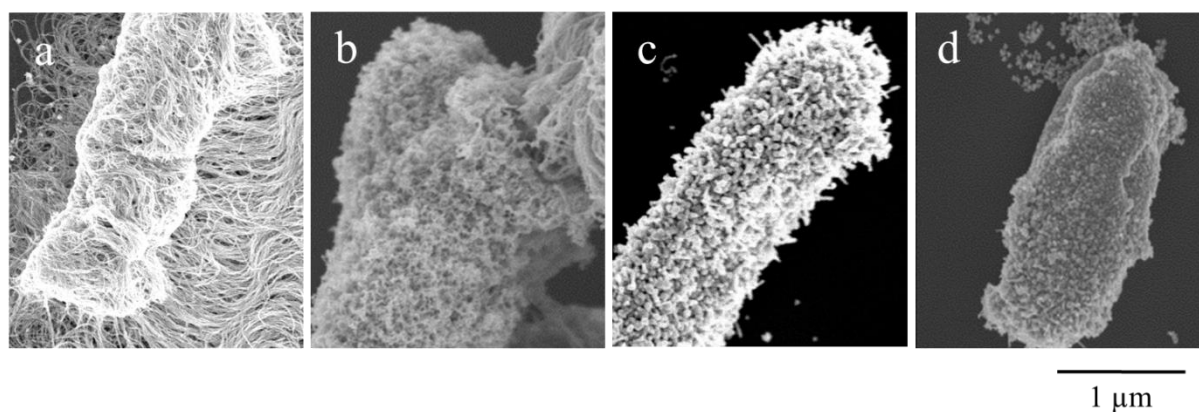


Figure 4.22 SEM images of Nanowire length control by MBA.  $\text{HAuCl}_4$  and L-ascorbic acid were at 0.425 and 1.205 mM, and the concentration of MBA was lowered to 27.5 (a), 11 (b), 5.5 (c), and 2.75 (d)  $\mu\text{M}$ , respectively.

#### 4.7.3 Nanowire Size Control by $\text{HAuCl}_4$ and L-ascorbic Acid

In this study, the Nanowire size can be controlled by adjusting concentration of  $\text{HAuCl}_4$  and L-ascorbic acid. Keeping MBA at 5.5  $\mu\text{M}$ , the concentration of  $\text{HAuCl}_4$  and L-ascorbic acid decreased from 0.43-1.03 mM to 0.21-0.51 mM. From the SEM images (Figure. 4.23) it is show that as the concentration of  $\text{HAuCl}_4$  and L-ascorbic acid decreased, Au deposited on Au seed-shell interface formed from large island to thin nanowires. This clearly suggested that the size of nanowires can be controlled by the amount of  $\text{HAuCl}_4$  and L-ascorbic acid. Higher concentration of  $\text{HAuCl}_4$  and L-ascorbic acid means gold deposition speed increase at certain amount of ligand, which results in short and wide nanowires.

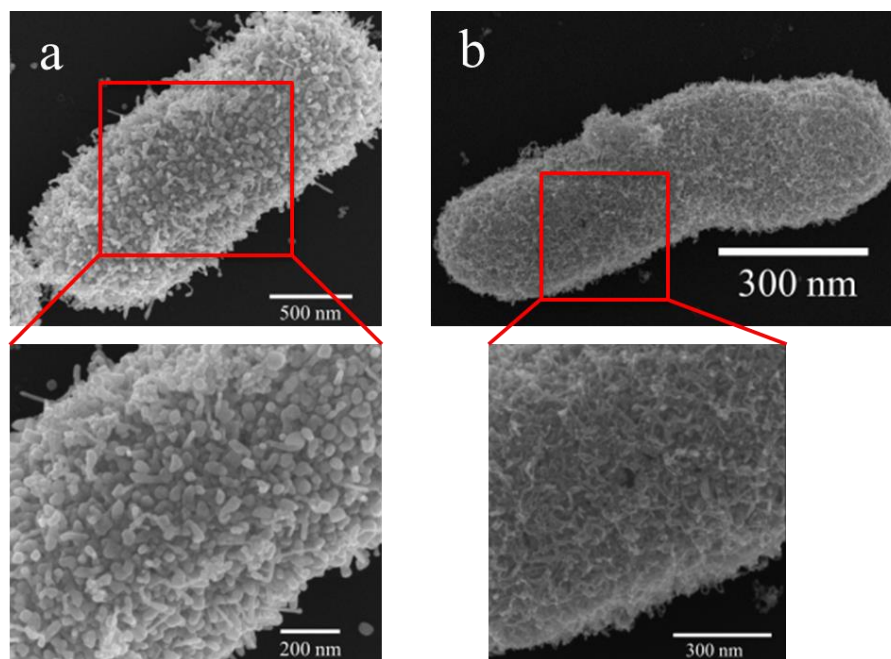
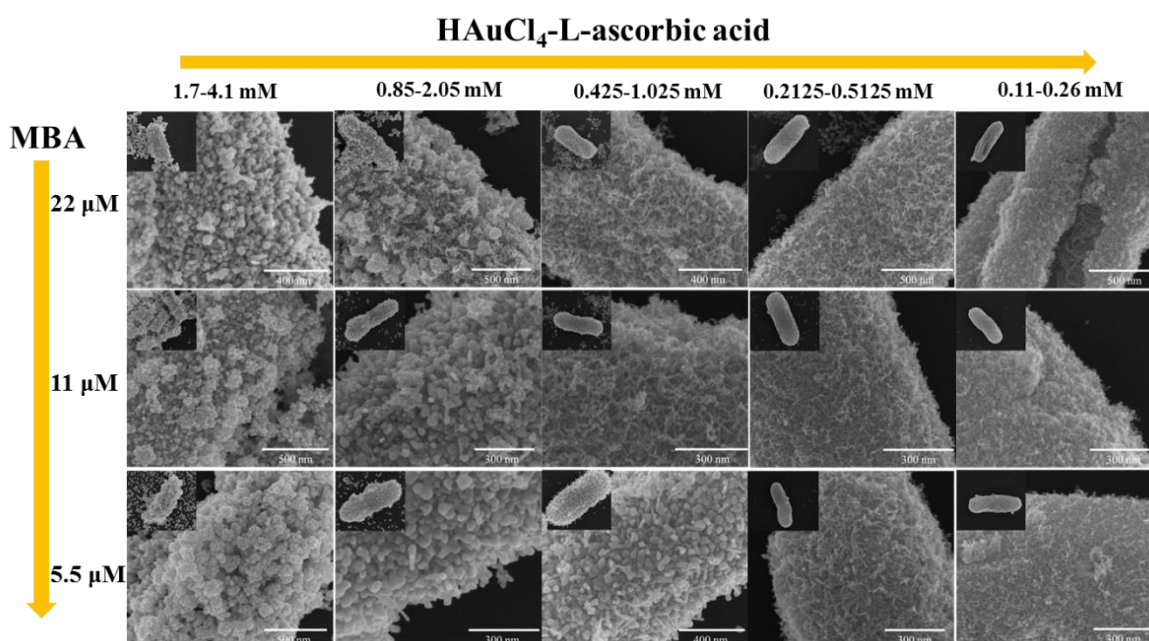


Figure 4.23 SEM images of Nanowire size control by  $\text{HAuCl}_4$  and L-ascorbic acid.

Form the a matrix SEM image (Figure. 4.24) it is clear show that this tendency that  $\text{HAuCl}_4$  and L-ascorbic acid affect the nanowires size is not only display at MBA at 5.5  $\mu\text{M}$ .



## Chapter 4

Figure 4.24 Matrix SEM images of different combinations of MBA and  $\text{HAuCl}_4$  - L-ascorbic acid.

When MBA concentration increased to 11  $\mu\text{M}$  and 22  $\mu\text{M}$ , the nanowires change from short and thick size to long and thin size with  $\text{HAuCl}_4$  and L-ascorbic acid decreased from 0.85-2.05 mM to 0.43-1.03 mM. However, this tendency is not work at all conditions when the concentration of  $\text{HAuCl}_4$  and L-ascorbic acid decreased. In some high concentration conditions, there are excess agglomerations of Au nanoparticles in the solution and on the surface of template structures. Therefore, these matrix results support a dynamic balance between MBA ligand binding and Au deposition. Only changing one factor of dynamic balance would cause nanowires formed different morphology.

### 4.7.4 AuNP Seeds Density Control

In this study, Au NP Seed density control was done. Diluted the concentrations of the gold seed colloid solution was used for Au nanoparticles attachment on silica shell from  $2.93 \times 10^{14}$  to  $2.93 \times 10^{13}$ ,  $2.93 \times 10^{12}$ , and  $2.93 \times 10^{11}$  particles/mL. Then the obtained Au seed-shell was used to grow nanowires. SEM images (Figure. 4.25) display as the concentration of Au seed decreased, Au deposited on Au seed-shell interface formed from normal nanowires to long nanowires, but the Au coverage was decreased. This is mainly due to the low Au seed on the silica shell made each seed get more growth solutions, which result it grow longer nanowires.

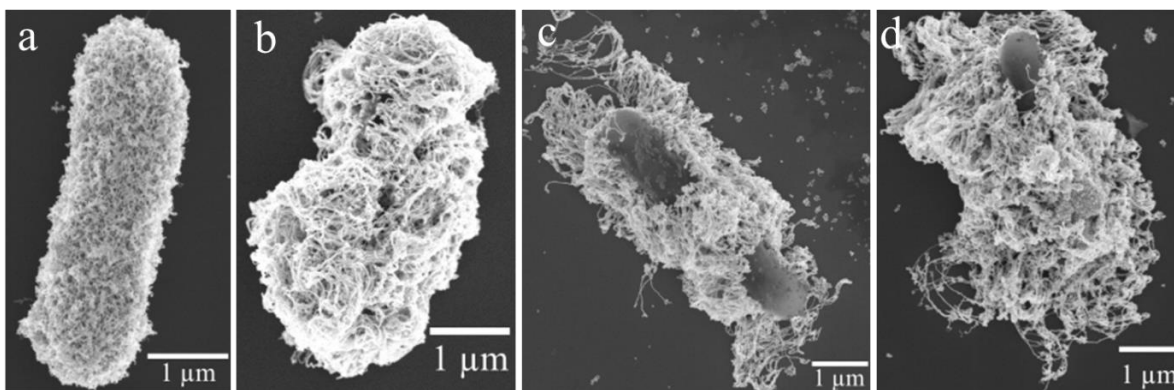
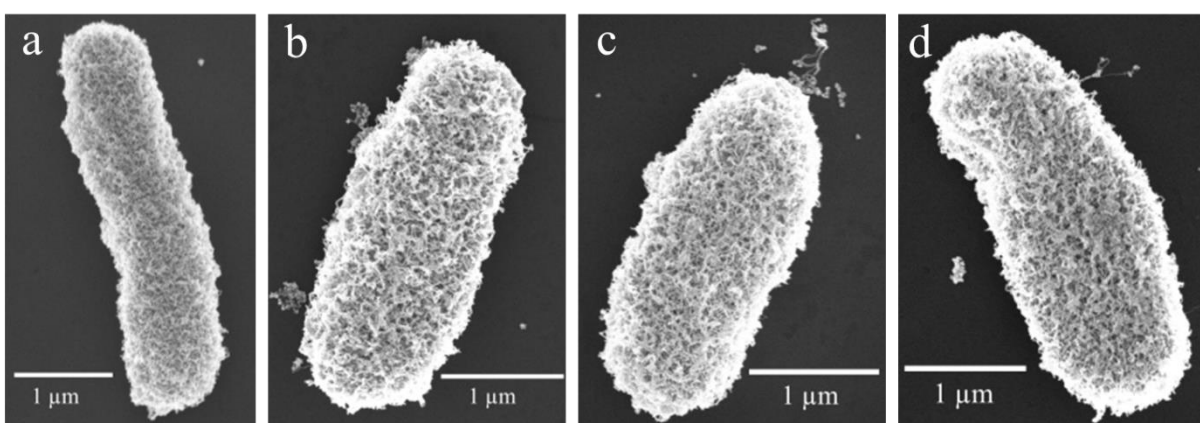


Figure 4.25 SEM images of AuNP seeds density control. Concentrations of the gold seeds were diluted the colloid solution to  $2.93 \times 10^{14}$  (a) to  $2.93 \times 10^{13}$  (b),  $2.93 \times 10^{12}$  (c), and  $2.93 \times 10^{11}$  (d) particles/mL. Then the obtained Au seed-shell was used to grow nanowires.

#### 4.7.5 Growth Time Control

In this study, growth time was study for trying to the control for the nanowires. In this study, all the reaction conditions were kept same, except the growth time. Growth time was compared between 0, 1, 5, and 15 min. SEM images (Figure. 4.26) showed no extinguished different between the lengths of growth time.



## Chapter 4

Figure 4.26 SEM images of AuNWs growth time control. Growth time was compared between 0, 1, 5, and 15 min. There are no extinguished different between the lengths of growth time.

### 4.8 Conclusion

In conclusion, we have successfully obtained hairy gold bacteria by *E. coli* bacteria templated synthesis. We demonstrated that the ultrathin gold nanowires could be grown selectively on bacteria surface by a seed-mediated growth progress. The morphology of Au nanowires can be controlled by adjusting the concentration of these key components in the nanowires growth system. In this part, the bacteria were successful used as bio-template to build plasmonic structures with gold nanowires growth on the bacteria surface. Due to the sample and repeatable process, this synthesis method could extend to other shape bio-template to work out the various needs for different fields of application. The hairy gold structures would be used in the piezoresistive strain sensor. The soft and elastic nanowires on the surface of bacteria template give the potential application in the sensor.

### 4.9 References

1. Schuller, J.A., et al., *Plasmonics for extreme light concentration and manipulation*. Nat Mater, 2010. **9**(3): p. 193-204.
2. Kelly, K.L., et al., *The Optical Properties of Metal Nanoparticles: The Influence of Size, Shape, and Dielectric Environment*. The Journal of Physical Chemistry B, 2003. **107**(3): p. 668-677.
3. Chen, H., et al., *Shape- and Size-Dependent Refractive Index Sensitivity of Gold Nanoparticles*. Langmuir, 2008. **24**(10): p. 5233-5237.
4. Jain, P.K., et al., *Calculated Absorption and Scattering Properties of Gold Nanoparticles of Different Size, Shape, and Composition:*

## Chapter 4

- Applications in Biological Imaging and Biomedicine*. The Journal of Physical Chemistry B, 2006. **110**(14): p. 7238-7248.
5. Shipway, A.N., E. Katz, and I. Willner, *Nanoparticle Arrays on Surfaces for Electronic, Optical, and Sensor Applications*. ChemPhysChem, 2000. **1**(1): p. 18-52.
  6. Ozbay, E., *Plasmonics: Merging Photonics and Electronics at Nanoscale Dimensions*. Science, 2006. **311**(5758): p. 189-193.
  7. Cui, P., et al., *Nonvolatile Memory Device Using Gold Nanoparticles Covalently Bound to Reduced Graphene Oxide*. ACS Nano, 2011. **5**(9): p. 6826-6833.
  8. Narayanan, R. and M.A. El-Sayed, *Shape-Dependent Catalytic Activity of Platinum Nanoparticles in Colloidal Solution*. Nano Letters, 2004. **4**(7): p. 1343-1348.
  9. Tang, Y. and W. Cheng, *Nanoparticle-Modified Electrode with Size- and Shape-Dependent Electrocatalytic Activities*. Langmuir, 2013. **29**(9): p. 3125-3132.
  10. Jing, H., et al., *Tunable Plasmonic Nanoparticles with Catalytically Active High-Index Facets*. Nano Letters, 2014. **14**(6): p. 3674-3682.
  11. Baaziz, W., et al., *Magnetic Iron Oxide Nanoparticles: Reproducible Tuning of the Size and Nanosized-Dependent Composition, Defects, and Spin Canting*. The Journal of Physical Chemistry C, 2014. **118**(7): p. 3795-3810.
  12. Demortiere, A., et al., *Size-dependent properties of magnetic iron oxide nanocrystals*. Nanoscale, 2011. **3**(1): p. 225-232.
  13. Park, T.-J., et al., *Size-Dependent Magnetic Properties of Single-Crystalline Multiferroic BiFeO<sub>3</sub> Nanoparticles*. Nano Letters, 2007. **7**(3): p. 766-772.
  14. Chen, Y., et al., *Mechanically Strong, Optically Transparent, Giant Metal Superlattice Nanomembranes From Ultrathin Gold Nanowires*. Advanced Materials, 2013. **25**(1): p. 80-85.
  15. Gao, T., et al., *Uniform and Ordered Copper Nanomeshes by Microsphere Lithography for Transparent Electrodes*. Nano Letters, 2014. **14**(4): p. 2105-2110.

## Chapter 4

16. Gong, S., et al., *A wearable and highly sensitive pressure sensor with ultrathin gold nanowires*. Nat Commun, 2014. **5**.
17. Gong, S., et al., *Highly Stretchy Black Gold E-Skin Nanopatches as Highly Sensitive Wearable Biomedical Sensors*. Advanced Electronic Materials, 2015. **1**(4): p. n/a-n/a.
18. Lee, S., et al., *Ag Nanowire Reinforced Highly Stretchable Conductive Fibers for Wearable Electronics*. Advanced Functional Materials, 2015. **25**(21): p. 3114-3121.
19. Tan, S.J., et al., *Building plasmonic nanostructures with DNA*. Nat Nano, 2011. **6**(5): p. 268-276.
20. Zheng, N., J. Fan, and G.D. Stucky, *One-Step One-Phase Synthesis of Monodisperse Noble-Metallic Nanoparticles and Their Colloidal Crystals*. Journal of the American Chemical Society, 2006. **128**(20): p. 6550-6551.
21. Jin, R., et al., *Controlling anisotropic nanoparticle growth through plasmon excitation*. Nature, 2003. **425**(6957): p. 487-490.
22. Sun, Y. and Y. Xia, *Shape-Controlled Synthesis of Gold and Silver Nanoparticles*. Science, 2002. **298**(5601): p. 2176-2179.
23. Wang, C., et al., *A General Approach to the Size- and Shape-Controlled Synthesis of Platinum Nanoparticles and Their Catalytic Reduction of Oxygen*. Angewandte Chemie, 2008. **120**(19): p. 3644-3647.
24. Sau, T.K. and C.J. Murphy, *Room Temperature, High-Yield Synthesis of Multiple Shapes of Gold Nanoparticles in Aqueous Solution*. Journal of the American Chemical Society, 2004. **126**(28): p. 8648-8649.
25. He, J., et al., *Forest of Gold Nanowires: A New Type of Nanocrystal Growth*. ACS Nano, 2013. **7**(3): p. 2733-2740.
26. Farrokhtakin, E., et al., *Radial growth of plasmon coupled gold nanowires on colloidal templates*. Journal of Colloid and Interface Science, 2015. **449**: p. 87-91.
27. Jana, N.R., L. Gearheart, and C.J. Murphy, *Seed-Mediated Growth Approach for Shape-Controlled Synthesis of Spheroidal and Rod-like Gold Nanoparticles Using a Surfactant Template*. Advanced Materials, 2001. **13**(18): p. 1389-1393.

## Chapter 4

28. Nikoobakht, B. and M.A. El-Sayed, *Preparation and Growth Mechanism of Gold Nanorods (NRs) Using Seed-Mediated Growth Method*. Chemistry of Materials, 2003. **15**(10): p. 1957-1962.
29. Chen, Y.-S., et al., *Enhanced thermal stability of silica-coated gold nanorods for photoacoustic imaging and image-guided therapy*. Optics Express, 2010. **18**(9): p. 8867-8878.
30. Pastoriza-Santos, I., J. Pérez-Juste, and L.M. Liz-Marzán, *Silica-Coating and Hydrophobation of CTAB-Stabilized Gold Nanorods*. Chemistry of Materials, 2006. **18**(10): p. 2465-2467.
31. Fernández-López, C., et al., *Highly Controlled Silica Coating of PEG-Capped Metal Nanoparticles and Preparation of SERS-Encoded Particles*. Langmuir, 2009. **25**(24): p. 13894-13899.
32. Halas, N.J., et al., *Plasmons in Strongly Coupled Metallic Nanostructures*. Chemical Reviews, 2011. **111**(6): p. 3913-3961.
33. Xiong, W., et al., *Multilayered core-satellite nanoassemblies with fine-tunable broadband plasmon resonances*. Nanoscale, 2015. **7**(8): p. 3445-3452.
34. Tan, S.J., et al., *Building plasmonic nanostructures with DNA*. Nature Nanotechnology, 2011. **6**: p. 268-276.
35. Liz-Marzán, L.M., *Tailoring Surface Plasmons through the Morphology and Assembly of Metal Nanoparticles*. Langmuir, 2005. **22**(1): p. 32-41.
36. Kelly, K.L., et al., *The Optical Properties of Metal Nanoparticles: The Influence of Size, Shape, and Dielectric Environment*. The Journal of Physical Chemistry B, 2002. **107**(3): p. 668-677.
37. Mulvaney, P., *Surface Plasmon Spectroscopy of Nanosized Metal Particles*. Langmuir, 1996. **12**(3): p. 788-800.
38. Mathiowitz, E., et al., *Biologically erodable microsphere as potential oral drug delivery system*. Nature, 1997. **386**(6623): p. 410-414.
39. Huang, H.Y., et al., *Nanocages derived from shell cross-linked micelle templates*. Journal of the American Chemical Society, 1999. **121**(15): p. 3805-3806.
40. Ohmori, M. and E. Matijevic, *Preparation and Properties of Uniform Coated Colloidal Particles .7. Silica on Hematite*. Journal of Colloid and Interface Science, 1992. **150**(2): p. 594-598.

## Chapter 4

41. Nam, K.T., et al., *Virus-enabled synthesis and assembly of nanowires for lithium ion battery electrodes*. Science, 2006. **312**(5775): p. 885-888.
42. Avery, K.N., J.E. Schaak, and R.E. Schaak, *M13 Bacteriophage as a Biological Scaffold for Magnetically-Recoverable Metal Nanowire Catalysts: Combining Specific and Nonspecific Interactions To Design Multifunctional Nanocomposites*. Chemistry of Materials, 2009. **21**(11): p. 2176-2178.
43. Berry, V., S. Rangaswamy, and R.F. Saraf, *Highly selective, electrically conductive monolayer of nanoparticles on live bacteria*. Nano Letters, 2004. **4**(5): p. 939-942.
44. Kuo, W.S., et al., *Biocompatible bacteria @Au composites for application in the photothermal destruction of cancer cells*. Chemical Communications, 2008(37): p. 4430-4432.
45. Neu, B., et al., *Biological cells as templates for hollow microcapsules*. Journal of Microencapsulation, 2001. **18**(3): p. 385-395.
46. Balkundi, S.S., et al., *Encapsulation of Bacterial Spores in Nanoorganized Polyelectrolyte Shells*. Langmuir, 2009. **25**(24): p. 14011-14016.
47. Franz, B., et al., *Layer-by-Layer Nano-Encapsulation of Microbes: Controlled Cell Surface Modification and Investigation of Substrate Uptake in Bacteria*. Macromolecular Bioscience, 2010. **10**(2): p. 164-172.
48. Krol, S., et al., *Encapsulated living cells on microstructured surfaces*. Langmuir, 2005. **21**(2): p. 705-709.
49. Krol, S., et al., *Encapsulated yeast cells inside Paramecium primaurelia: a model system for protection capability of polyelectrolyte shells*. Journal of Microscopy-Oxford, 2003. **212**: p. 239-243.
50. Kozlovskaya, V., et al., *Hydrogen-bonded LbL shells for living cell surface engineering*. Soft Matter, 2011. **7**(6): p. 2364-2372.
51. Germain, M., et al., *Protection of mammalian cell used in biosensors by coating with a polyelectrolyte shell*. Biosensors & Bioelectronics, 2006. **21**(8): p. 1566-1573.
52. Swiston, A.J., et al., *Surface Functionalization of Living Cells with Multilayer Patches*. Nano Letters, 2008. **8**(12): p. 4446-4453.

## Chapter 4

53. Matsusaki, M., et al., *Fabrication of cellular multilayers with nanometer-sized extracellular matrix films*. Angewandte Chemie-International Edition, 2007. **46**(25): p. 4689-4692.
54. Ahmad, A., et al., *Extracellular biosynthesis of silver nanoparticles using the fungus Fusarium oxysporum*. Colloids and Surfaces B-Biointerfaces, 2003. **28**(4): p. 313-318.
55. Daniel, M.C. and D. Astruc, *Gold nanoparticles: Assembly, supramolecular chemistry, quantum-size-related properties, and applications toward biology, catalysis, and nanotechnology*. Chemical Reviews, 2004. **104**(1): p. 293-346.
56. Giljohann, D.A., et al., *Gold Nanoparticles for Biology and Medicine*. Angewandte Chemie-International Edition, 2010. **49**(19): p. 3280-3294.
57. Nomura, T., et al., *Synthesis of hollow silica microparticles from bacterial templates*. Advanced Powder Technology, 2010. **21**(2): p. 218-222.
58. Oldenburg, S.J., et al., *Surface enhanced Raman scattering in the near infrared using metal nanoshell substrates*. Journal of Chemical Physics, 1999. **111**(10): p. 4729-4735.
59. He, J.T., et al., *Forest of Gold Nanowires: A New Type of Nanocrystal Growth*. Acs Nano, 2013. **7**(3): p. 2733-2740.



---

## **Chapter 5. Self-Assembly Nanoparticle**

### **Pyramids: Shape-Dependent Plasmonics**

### **and SERS Enhancement**

---



## Chapter 5

### 5.1 Introduction

Surface-enhanced Raman spectroscopy (SERS) is a powerful technique for sensing molecules in trace amounts down to single-molecule detection level, which has a great impact in fields of biology and medicine [1-5]. Noble metal could provide a large SERS effect for roughened metal surfaces and colloidal metal particles with dimensions in the order of nanometers [6-8]. Therefore, the SERS activity strongly depends on the nature of the substrates such as the size and shape of nanoparticles as well as the interparticles distance and arrangement pattern [9-14]. Fabricating substrate with high sensitivity and reproducibility is a crucial step for SERS enhancement.

Usually there are two ways for fabrication, one is bottom up method to self-assembly nanoparticles to complex structure, and another method is top down method utility of conventional lithographic technique [15-20]. The combination of bottom up and top down own benefits of two methods, evaporation the nanoparticles solution at the mask with reusability, low cost, precise definition pattern, high throughput, simplicity of the assembly procedure, and possibility to scale up to macroscale assemblies[21-23].

One of the classic Klarite substrate with array of inverted pyramid structures is widely used as commercial SERS substrate [24-27]. The unique property of pyramid structure produce hot spot that could remarkable enhanced the SERS intensity. Many research have focused concerted efforts toward increasing the enhancement ability of pyramid shape substrate [28-31]. One simple procedure was reported that generation free-standing mesoscale metallic pyramids have well-defined ultrasharp tips, and they have potential use as substrates for SERS

## Chapter 5

application [28]. Researchers found that by integrating nanocones on silicon micropillar array devices can improve the SERS enhancement property [29]. It is found that the SERS substrates with nanopillar-on-pyramid structure always have the stronger enhancement factor than the SERS substrates with only pyramids or nanopillars [30]. A recent study using template-assisted method fabricate gold spherical nanoparticle assembly pyramidal periodical arrays that exploited as carbon monoxide SERS sensor [31].

We aim to understand and maximize the SERS effect on pyramidal substrates. For this purpose, large-scale nanoparticle building blocks with controllable morphologies are highly desirable. This study offered a combined top-down and bottom-up approach to fabricate structurally well-defined nanoparticle pyramids, which can help us better understand nanoparticle shape and pyramid structure for SERS enhancement.

Here, I describe a simple yet efficient approach to fabricate plasmonic nanoparticle pyramids via combining top-down lithography and bottom-up self-assembly. In order to understand and maximize the SERS effect, large-scale nanoparticle building block with controllable morphologies are highly desirable. Three types of shapes of gold nanoparticles with identical size were assembled to pyramid building block for SERS substrate. We investigated the nanoparticle shape effect and building block morphology effect on the assembly pyramid for SERS, and their optical property. We found that the tip of pyramid building block exhibit significantly strong SERS intensity than other parts. And we also found rhombic dodecahedral (RD) shape nanoparticles assembly pyramid building block give the strongest SERS enhancement.

## Chapter 5

### 5.2 Method and Materials

#### 5.2.1 Materials

Gold (III) chloride trihydrate ( $\text{HAuCl}_4 \cdot 3\text{H}_2\text{O}$ ,  $\geq 99.9\%$ ), hexadecyltrimethylammonium bromide (CTAB), silver nitrate ( $\text{AgNO}_3$ ), sodium borohydride ( $\text{NaBH}_4$ ), L-ascorbic acid (AA), potassium bromide (KBr), potassium hydroxide (KOH), isopropyl alcohol (IPA), 4-aminothiophenol (4-ATP), cetylpyridinium chloride (CPC), ammonium hydroxide solution ( $\text{NH}_4\text{OH}$ ), hydrogen peroxide solution ( $\text{H}_2\text{O}_2$ ) were purchased from Sigma-Aldrich. Poly (dimethylsiloxane) (PDMS) Sylgard (184) silicon elastomer, curing agent, and precursor were purchased from Dow Corning, USA. All chemicals were used as-received unless otherwise indicated. Deionized water was used in all aqueous solutions, which were further purified with a Milli-Q system (Millipore). All glassware used in the following procedures were cleaned in a bath of freshly prepared aqua regia and were rinsed thoroughly in  $\text{H}_2\text{O}$  prior to use.

#### 5.2.2 Synthesis of Gold Nanocrystals

##### 5.2.2.1 Synthesis of Gold Seeds

The synthesis of gold nanocrystal occurred with a series of seed-mediated growth [32]. A 100  $\mu\text{L}$  aliquot of 25 mM  $\text{HAuCl}_4$  and 5 mL of 0.2 M CTAB solution were added to solution in sequence at 30  $^\circ\text{C}$  under stirring, after 1 min mixture, 0.6 mL of 10 mM ice-cold  $\text{NaBH}_4$  solution was added into the mixture solution, keeping stirring 5 min to ensure well mixing. The CTAB capped gold seeds solution was stored at 30  $^\circ\text{C}$  for future use.

##### 5.2.2.2 Synthesis of Gold Nanorods

## Chapter 5

The nanorod growth solution was prepared by addition of the following in sequence: 200  $\mu\text{L}$  of 4 mM  $\text{AgNO}_3$ , 5 mL of 0.2 M CTAB, 5 mL  $\text{HAuCl}_4$  of 1 mM and 80  $\mu\text{L}$  of 0.08 M AA solution. The mixture solution was shaken once following each addition. 12  $\mu\text{L}$  CTAB capped gold seeds were added into the growth solution and shaken once. The tube was then placed into a 30  $^\circ\text{C}$  water bath for 2 hours.

### 5.2.2.3 Synthesis of Overgrown Gold Nanorods

After 2 hours, 30 mL gold nanorods solution was centrifuged and redispersed in water to examine with UV-Vis spectroscopy. Subsequently, the solution was centrifuged again and redispersed in 30 mL of 10 mM CTAB solution at 40  $^\circ\text{C}$ . Lastly, 1.5 mL of 10 mM  $\text{HAuCl}_4$  solution and 0.3 mL of 100 mM AA solution were added in sequence and mixed thoroughly. The mixture was allowed to react at 40  $^\circ\text{C}$  for 1 hour, after reaction the overgrown gold nanorods was washed and redispersed on 30 mL 0.01 M CTAB for next step growth.

### 5.2.2.4 Synthesis of Near-Spherical Gold Nanoparticle

600  $\mu\text{L}$  of 10 mM  $\text{HAuCl}_4$  was added into the overgrown nanorods solution. The mixture solution was left in water bath 40  $^\circ\text{C}$  for 12 hours. The reaction was stopped by centrifuging, and the supernatant was removed to separate the near-spherical nanoparticles from the growth solution. The near-spherical nanoparticles were redispersed with 30 mL of 100 mM cetylpyridinium chloride (CPC) solution before washed twice. This CPC-capped near-sphere gold nanoparticles were examined with UV-Vis spectroscopy.

## Chapter 5

### 5.2.2.5 Synthesis of Rhombic Dodecahedral Gold Nanocrystals

The growth solution of rhombic dodecahedral gold nanocrystals was prepared by addition of the following in sequence: 5mL of 0.01 M CPC, 100  $\mu$ L of 0.01 M HAuCl<sub>4</sub>, and 200  $\mu$ L of 0.1M AA. The mixture solution was shaken once following each addition. 100uL of the CPC-capped near-sphere gold nanoparticles was added into the growth solution and shaken once. The tube was then placed into a 30 °C water bath for 2 hours. The synthesized RD was stopped growth by centrifugation and redispersed in 200  $\mu$ L H<sub>2</sub>O.

### 5.2.2.6 Synthesis of Octahedral Gold Nanocrystals

The growth solution of octahedral gold nanocrystals was prepared by addition of the following in sequence: 5 mL of 0.1 M CPC, 100  $\mu$ L of 0.01 M HAuCl<sub>4</sub>, and 13  $\mu$ L of 0.1 M AA. The mixture solution was shaken once following each addition. 100  $\mu$ L of the CPC-capped near-sphere gold nanoparticles was added into the growth solution and shaken once. The tube was then placed into a 30 °C water bath for 2 hours. The synthesized RD was stopped growth by centrifugation and redispersed in 200  $\mu$ L H<sub>2</sub>O.

### 5.2.2.7 Synthesis of Sphere Nanocrystals

The growth solution of sphere nanocrystals was prepared by addition of the following in sequence: 5 mL of 0.1M CPC, 500  $\mu$ L of 100 mM KBr solution, 100  $\mu$ L of 0.01 M HAuCl<sub>4</sub>, and 15  $\mu$ L of 0.1 M AA.. The mixture solution was shaken once following each addition. 100uL of the CPC-capped near-sphere gold nanoparticles was added into the growth solution and shaken once. The tube was then placed into a 30 °C water bath for 2 hours. The synthesized RD was stopped growth by centrifugation and redispersed in 200  $\mu$ L H<sub>2</sub>O.

## Chapter 5

### 5.2.2.8 Template Fabrication

The template was prepared according to the procedure reported previously[33, 34]. Firstly, the silicon nitride was deposited on the clean silicon wafer. Then, wafer was coated with pattern photoresist, following transferred the designed mask patterns onto the silicon substrate through the photolithography means (The mask was made by Minnesota Nano Center at the University of Minnesota.). Then the substrate was etched in the wet etching solution containing KOH (30%) and IPA (5%) at 40 °C. The etching time depends on the size of pyramid, and it takes 30min for 5.0  $\mu\text{m}$  sides of square pyramid to finish the etching. The etch angle is 54.7°, so the height of pyramid is around 3.5  $\mu\text{m}$ . After that, the etched inverted pyramid template was wash by MQ water, and cleaned in the cleaning solution ( $\text{H}_2\text{O}:\text{NH}_4\text{OH}:\text{H}_2\text{O}_2=5:1:1$ ) to remove the bumps on the pyramid surface.

### 5.2.2 Nanoparticles Assembly

10  $\mu\text{L}$  of concentrated gold nanocrystals solution was dropped on the surface of the template. The system was placed in a chamber with high humidity for slowly evaporated. After 96 hours, the drop was dried on the template, and then transfer to the carbon tape or PDMS for characterization and SERS measurement.

### 5.2.4 Structural and Optical Characterization

Scanning electron microscopy (SEM) images of the nanostructures were taken with a field emission SEM (JEOL 7001 F). Absorption spectra of the nanoparticle solution were recorded using an Agilent 8453 UV–Vis spectrometer. The scattering spectra of the pyramid films and the single pyramid images were

## Chapter 5

obtained using CytoViva hyperspectral imaging system. Dark field optical images were taken by Nikon Ti-U microscope.

### 5.2.5 SERS Measurement

The pyramid film assembled with different shapes of nanoparticles (sphere, octahedral and RD nanoparticles) were immersed in the 1 mL 4-ATP (100 mM) overnight, then washed by ethanol, and allowed to dry prior to SERS measurements. The SERS measurement was carried out using a WITTEC 300R Raman microscope taking mapping areas of  $26 \times 36 \mu\text{m}^2$ , with a step size of 500 nm (100 $\times$  objective) upon excitation with 532 nm and NIR (785 nm) laser line.

## 5.3 Results and Discussion

### 5.3.1 Fabrication Nanoparticles Assembly Pyramid Arrays

The scheme of assembly pyramid arrays film was illustrated in Figure 5.1. This method was modified from previously reported method [31], which combined self-assembly and templates methods to form superstructure with the defined shape. Firstly, the silicon template with inverted pyramid shape was prepared by photolithography technique, followed by wet etching process to yield pyramidal pattern substrate. SEM image (Figure 5.1d) shows the single inverted pyramid template. Then, concentrated nanoparticle solution was dropped on the template to allow dry under sealed high humidity condition. When the solvent completely vaporized, the assembled nanoparticles were then transferred into a flat substrate, the transferred assembled nanoparticles with pyramid arrays on the PDMS. Figure 5.1e and f showed the SEM images of RD nanoparticles assembly pyramid before and after transfer to PDMS.

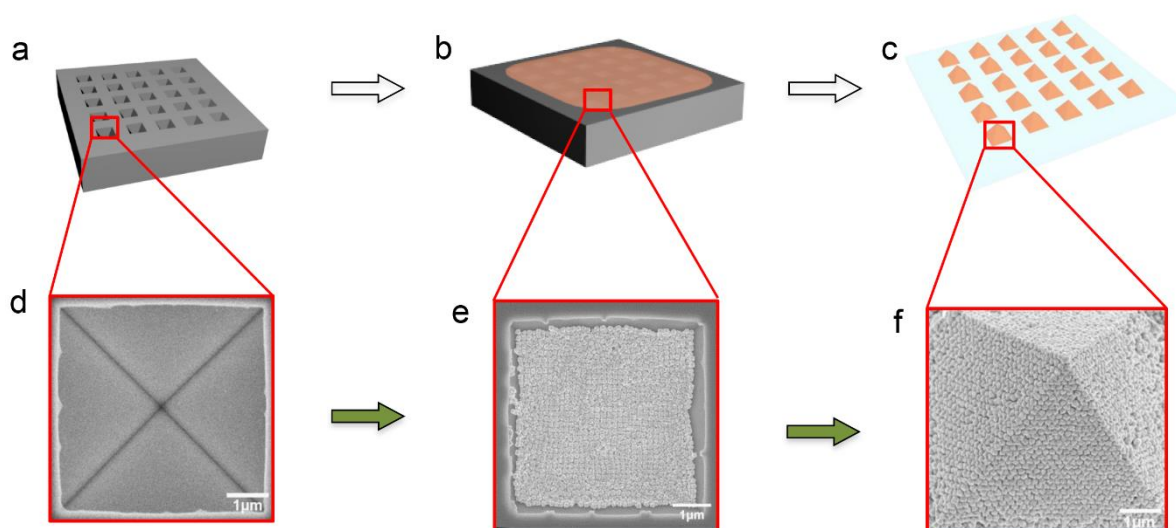


Figure 5.1 Schematic of fabrication nanoparticles assembly pyramid arrays film and corresponding experimental results of single pyramid SEM images.

In this method, template is crucial factor in the pyramid arrays fabrication. The surface smooth and uniform template decide the assembly pyramid quality. Anisotropic KOH etching process yields homogeneous periodic pattern with inverted square pyramids, the side of square is  $5.0\ \mu\text{m}$  and the height of pyramid is  $3.5\ \mu\text{m}$ . After cleaning process, surface smooth pyramid template was formed, Figure 5.1d showed a single inverted pyramid template and Figure 5.2a display the smooth surface pyramid pattern. Due to the template with well-patterned pyramid structure, the RD nanoparticles building block also formed the neat pyramid arrays (Figure 5.2b).

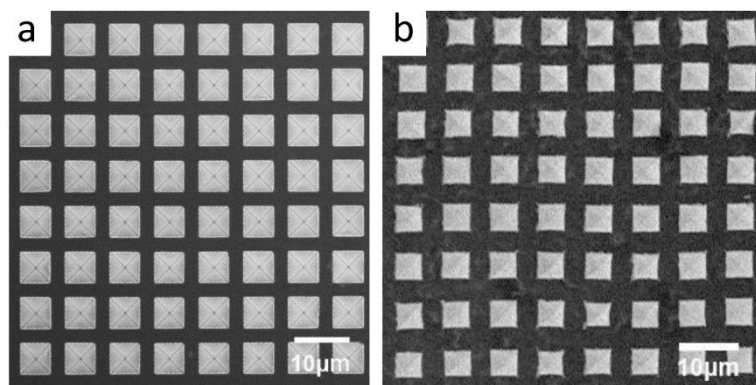


Figure 5.2 SEM images of (a) Si wafer template with inverted pyramid pattern at low magnification and (b) transfer RD nanoparticles assembly pyramid arrays.

In this study, three different shapes of gold nanoparticles, rhombic dodecahedral (RD), octahedral and sphere were chose to assembly pyramid building blocks. In order to keep all factors same except the shape, these three shapes of single-crystalline nanoparticles are synthesis by similar seed-mediated growth method with similar size, the shape was manipulated by kinetics of the nanoparticles.

### 5.3.2 Morphological Characterization of Pyramid Arrays

After RD nanocrystal assembly, transferred assembly pyramid was characterized by SEM. Low magnification SEM (Figure 5.2b) image show homogeneous RD nanoparticles assembly pyramid sit in line to form periodic arrays. Each pyramid was intact with tip and edges. A single pyramid building block was displayed in Figure 5.3a, and RD nanocrystal closed packed into pyramid structure. There was one RD nanocrystal sit at the tip of pyramid building block, the next layer was four RD nanocrystal and the third layer was composed of 9 RD nanocrystal (Figure 5.3b). RD nanoparticles array to a line formed the edge of pyramid (Figure 5.3c). What is more, not only RD nanoparticles

## Chapter 5

assembled pyramid arrays, the octahedral and sphere shape nanoparticles also assembled to pyramid building block, the SEM images (Figure 5.3d and g) showed octahedral and sphere nanoparticles assembled to pyramid. Thus, the shape of nanoparticles do not affect the nanoparticles to assembly pyramid with assist of template.

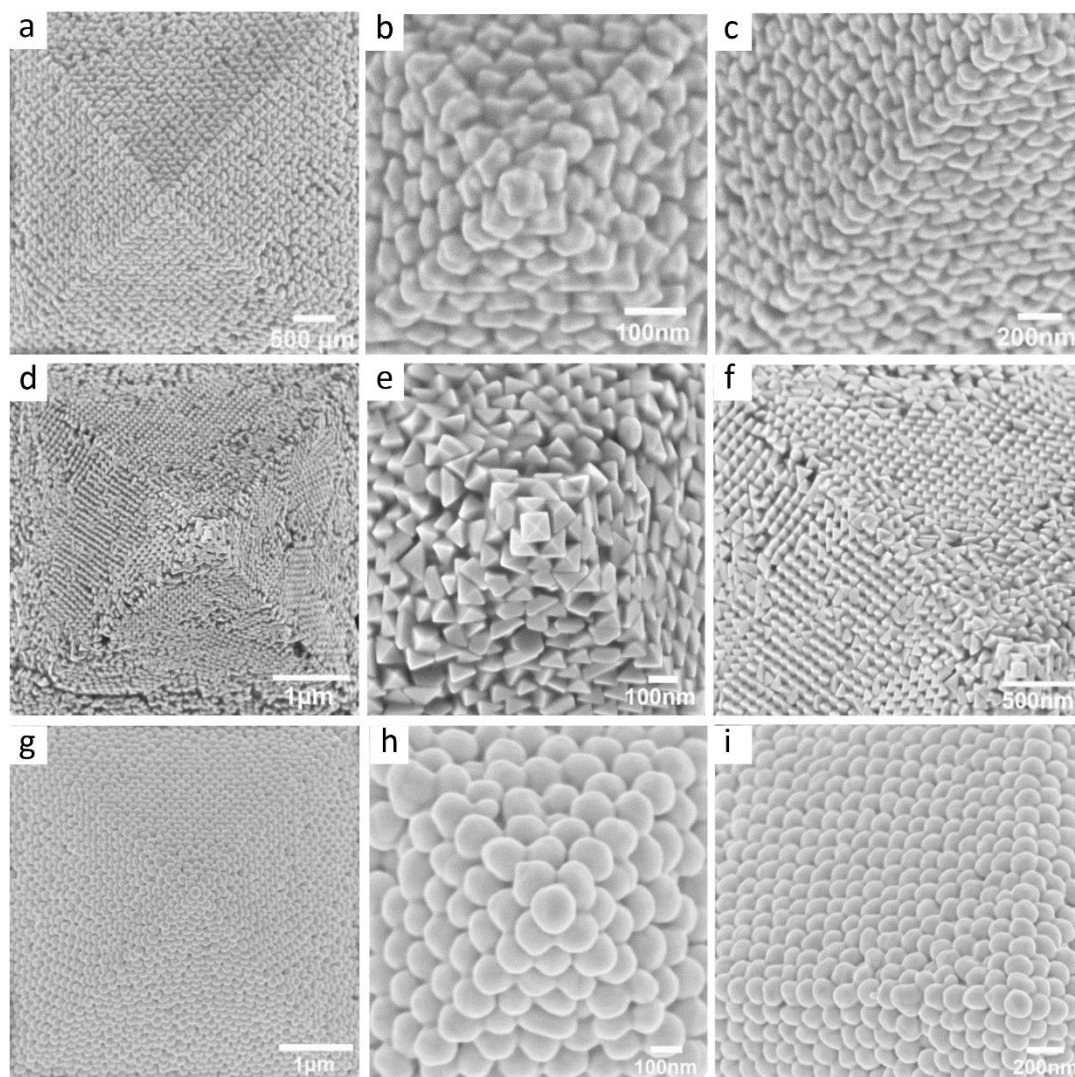


Figure 5.3 SEM images of single pyramid building block assembly by (a) RD NPs, (b) tip of pyramid and (c) edge of pyramid; (d) octahedral NP assembly pyramid and (e) tip and (f) edge; (g) octahedral NP assembly pyramid and (h) tip and (i) edge

## Chapter 5

### 5.3.3 Scattering Property of Pyramid Arrays

In this study we also characterized the assembly pyramid arrays using dark field (DF) microscopy. In Figure 5.4, the pyramid arrays can easily be observed under the DF microscope at low magnification for three shapes of nanoparticle assembly films. What is more, the side, edge and tip are clearly distinguished due to the different brightness of reflection at different areas of the pyramid. Interestingly, the three different shapes of nanoparticle assembly films displayed different colors under the same DF microscopy condition. RD and sphere pyramid films displayed similar orange yellow color (Figure 5.4a, c), but the octahedron pyramid film presented the golden color (Figure 5.4b). The difference in color is mainly caused by the shape and arrangements of nanoparticles.

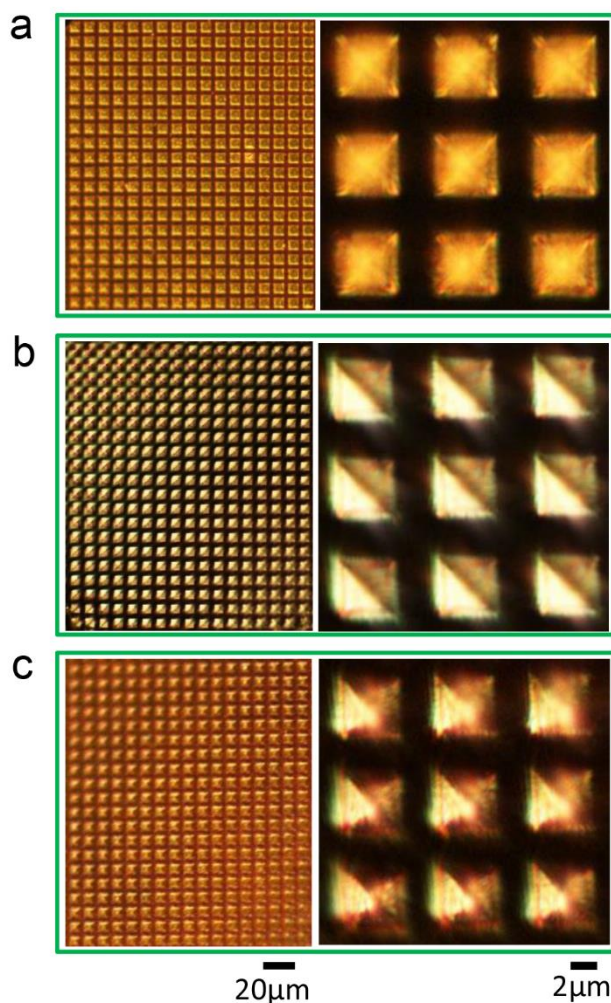


Figure 5.4 Darkfield images of (a) RD nanoparticles, (b) octahedral nanoparticles and (c) sphere nanoparticles assembly pyramid arrays at low magnification and high magnification

To investigate this more specifically the optical property at different areas of pyramid, we employed CytoViva hyperspectral imaging system to study the scattering property of the pyramid. In the scattering spectrum measurement, whole pyramid was divided into three parts: tip, side, edge. Several points of the scattering spectra measured along the line of side or edge showed in the scheme from tip to bottom (Figure 5.5). Similarly, the three shapes nanoparticles assembly pyramid showed different color under CytoViva optical microscopy

## Chapter 5

(Figure 5.6a, d and h). From the Cytoviva data we get two parameters, spectra wavelength and intensity, and plot the peak wavelength and intensity of each point in a same figure (Figure 5.6b, c, e, f, i, j). We can see that for all these three shapes of nanoparticle assembly pyramid, the scattering wavelength of the peak position show red shift from bottom to tip, and the peak wavelength of tip is the highest. This phenomenon of wavelength shift is caused by interparticle coupling. The central of pyramid showed the strongest coupling effect.

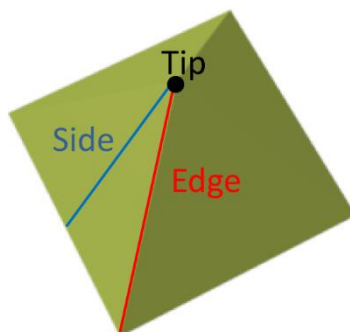


Figure 5.5 Schematic of scattering spectra measurement. The pyramid was divided into three parts: tip, side and edge.

## Chapter 5

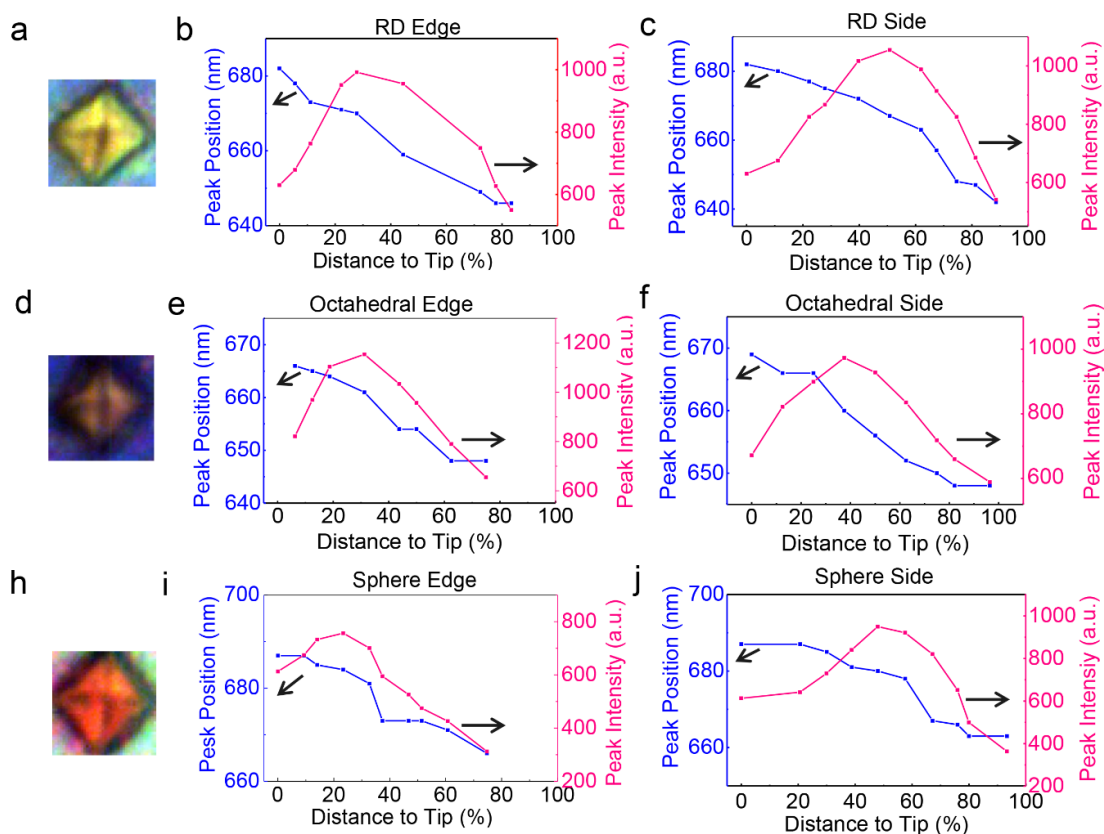


Figure 5.6 Optical images of RD (a), octahedral (d) and sphere (h) nanoparticles assembly pyramid. And their corresponding peak position and intensity of scattering spectra at edge and side of pyramid.

Unlike the scattering wavelength of the peak position, the intensity show highest value around the middle of the pyramid. There is still slightly difference between edge and side. For the edge, the highest intensity point emerge in the position of around 30% distance to top for all three shapes of building nanoparticle. While for the side, the highest intensity point emerge in the position of around 40-50% distance to top for all three shapes of building nanoparticle. The scattering intensity value is depend on the pyramid shape. At the tip of pyramid the few nanoparticles cannot absorb and scattering much light comparing with the middle

part of pyramid. So the intensity of middle position is the highest. Therefore, the scattering intensity of each point is affected by the whole pyramid structure.

### 5.3.4 Nanoparticle Shape and Pyramid Structure for SERS Enhancement

As the intimately contacting nanoparticles can create hot spots with high local electromagnetic field for the surface-enhanced Raman scattering (SERS) detection of adsorbed molecules. In this study Raman signal for sphere, octahedral and RD shape nanocrystal assembly pyramids were measured with both 785 nm and 535 nm laser power using 4-aminothiophenol (4-ATP) as the detection molecular. 4-ATP can self-assemble through strong Au-S interaction on the gold surfaces, therefore commonly used in the SERS evaluation of Au nanostructures.

The characteristic scattering peak of 4-ATP can be clearly observed for all three shapes of nanoparticles pyramid assembly at excitation wavelengths of 785nm (laser power 2mW, an acquisition time 0.1s) (Figure 5.6). The strongest peak is at  $1078\text{ cm}^{-1}$ , which is the CS stretching mode and another main peak at  $1588\text{ cm}^{-1}$  is attributed to the ring stretch [35]. The peak intensities at  $1078\text{ cm}^{-1}$  for the nanoparticles assembled pyramid used to be compared for the following pyramid area intensity and shape effect on the SERS enhancement.

To compare the SERS enhancement of different position on the pyramid, we investigated the SERS mapping for the pyramid arrays film. From the optical image under Raman microscope and corresponding SERS mapping image of RD pyramid film at 785 laser excitation (Figure 5.7a), the center of the pyramid showed the highest intensity. SERS mapping data of the RD assembly pyramid, the intensity at tip showed the distinctly higher than other parts (Figure 5.7b). It

## Chapter 5

clearly demonstrated that enhancement intensity depends on the position of pyramid structure, and all three shapes assembly pyramid show the same trends (Figure 5.7c, d, e and f). The mapping results from laser 532 nm showed the similar trend, which the tip of pyramid gave the strongest signal than other area of pyramid (Figure 5.8).

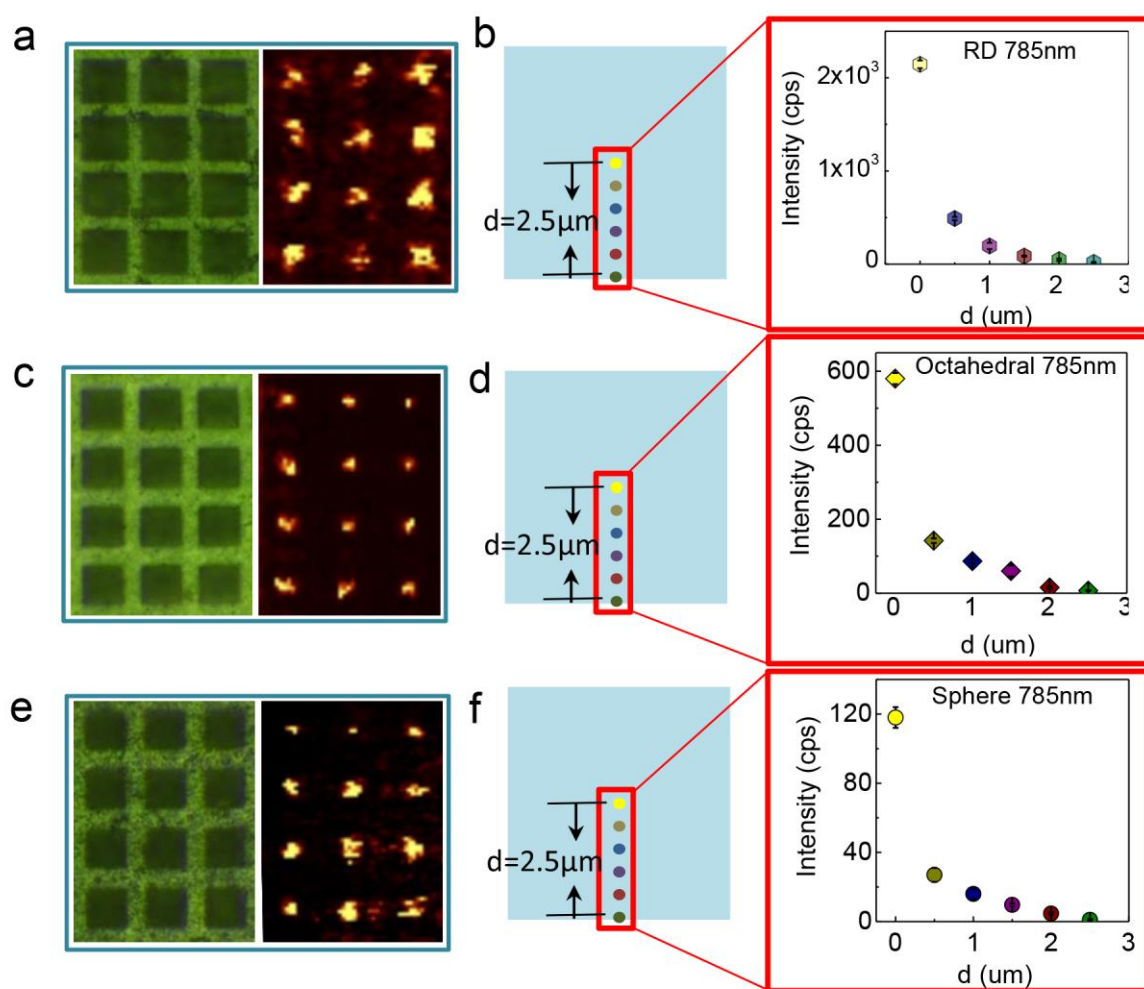


Figure 5.7 (a, c, e) optical images and SERS imaging of 1078 peak band in Raman spectra of RD, octahedral and sphere nanoparticles assembly pyramid film by laser 785nm. (b, d and f).

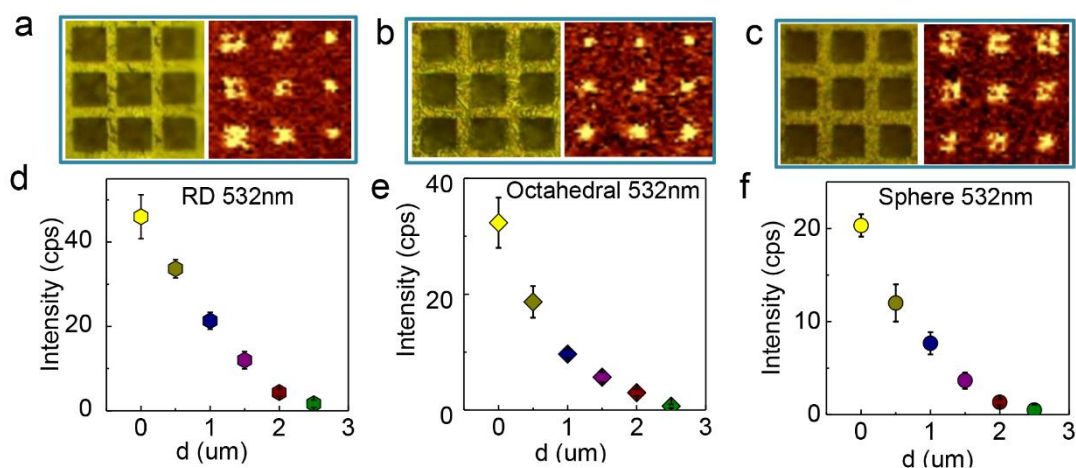


Figure 5.8 (a, b, c) optical image and SERS imaging of 1078 peak band in Raman spectra of RD, octahedral, sphere nanoparticles assembly pyramid film by laser 532nm (b, d and f).

Further, the shape effect on the SERS enhancement is investigated with peak intensity at  $1078\text{ cm}^{-1}$ . Clearly, the SERS activates of RD pyramid is the strongest among those signals in 785 nm lasers (Figure 5.9a). SERS spectra of three shapes assembly pyramid were also acquired with the excitation laser of 532 nm and compared in Figure 5.9b. Interestingly, similar trends of SERS intensity changes at  $1078\text{ cm}^{-1}$  were observed, and RD pyramid give the strongest SERS intensity. One important reason for the high SERS intensity of RD is that RD nanoparticles contain more highly anisotropic tips and edges that can create more efficient hot spots between the junction regions among the adjacent nanoparticles for SERS and assembly RD nanoparticles form long-ranges ordered arrangements, therefore, leading to higher SERS intensity [12, 36, 37]. Another reason is the active sites on the surfaces of nanoparticles could promote the adsorptions of the probe molecules to their surface. It is reported that gold RD nanoparticles showed the largest SERS intensity because the Au

## Chapter 5

(110) facets binding molecules energy are much higher than those of the Au (111) and (110) facets [38].

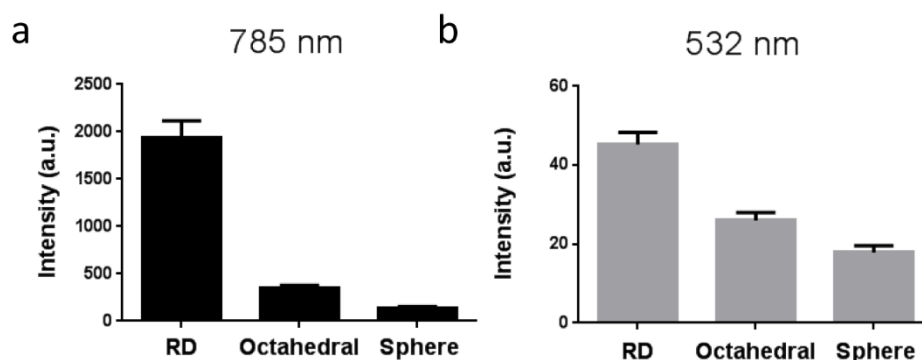


Figure 5.9 SERS intensity of RD, octahedral and sphere nanoparticles assembly pyramid film under (a) 785 nm and (b) 532 nm laser excitation.

The peak intensity of 785 nm laser was significant strong than 532 nm laser. This is because the SERS peak intensities depend on the excitation laser wavelength used [15, 39]. The excitation wavelength of 785 nm as compared 532 nm closely matches the plasmon resonance (around 680 nm) of pyramid building block, which provides significant local electromagnetic field confinement on the plasmonic nanostructure.

### 5.4 Conclusion

In conclusion, we fabricated the nanoparticles assembly pyramid and investigated their optical property and SERS activity. The RD, octahedral and sphere nanoparticles was succeed to assembly pyramid building block under the template assisted. Due to the coupling effect of interparticles and pyramid structure, plasmon resonance red-shift from bottom to the tip of pyramid and the

## Chapter 5

highest peak intensity at the middle of pyramid. All these pyramid films have been explored as SERS substrate to investigate the Raman intensity on shape effect. The pyramid tip showed the strongest Raman enhancement than other parts, and maximized Raman enhancement was achieved at pyramid substrate assembled by RD nanoparticles.

### 5.5 References

1. Vo-Dinh, T., F. Yan, and M.B. Wabuyele, *Surface-enhanced Raman scattering for medical diagnostics and biological imaging*. Journal of raman spectroscopy, 2005. 36(6-7): p. 640-647.
2. Kneipp, K., et al., *Single Molecule Detection Using Surface-Enhanced Raman Scattering (SERS)*. Physical Review Letters, 1997. 78(9): p. 1667-1670.
3. Lane, L.A., X. Qian, and S. Nie, *SERS Nanoparticles in Medicine: From Label-Free Detection to Spectroscopic Tagging*. Chemical Reviews, 2015.
4. Schlücker, S., *Surface-Enhanced Raman Spectroscopy: Concepts and Chemical Applications*. Angewandte Chemie International Edition, 2014. 53(19): p. 4756-4795.
5. Jeanmaire, D.L. and R.P. Van Duyne, *Surface raman spectroelectrochemistry*. Journal of Electroanalytical Chemistry and Interfacial Electrochemistry, 1977. 84(1): p. 1-20.
6. Nie, S. and S.R. Emory, *Probing Single Molecules and Single Nanoparticles by Surface-Enhanced Raman Scattering*. Science, 1997. 275(5303): p. 1102-1106.
7. Chen, C.Y., et al., *Giant Raman scattering and luminescence by molecules adsorbed on Ag and Au metal island films*. Surface Science, 1980. 101(1): p. 363-366.
8. Orendorff, C.J., et al., *Aspect ratio dependence on surface enhanced Raman scattering using silver and gold nanorod substrates*. Physical Chemistry Chemical Physics, 2006. 8(1): p. 165-170.

## Chapter 5

9. Cialla, D., et al., *Surface-enhanced Raman spectroscopy (SERS): progress and trends*. Analytical and Bioanalytical Chemistry, 2012. 403(1): p. 27-54.
10. Lin, W.-C., et al., *Size Dependence of Nanoparticle-SERS Enhancement from Silver Film over Nanosphere (AgFON) Substrate*. Plasmonics, 2011. 6(2): p. 201-206.
11. Chen, J., et al., *Fabrication of Large-Area, High-Enhancement SERS Substrates with Tunable Interparticle Spacing and Application in Identifying Microorganisms at the Single Cell Level*. The Journal of Physical Chemistry C, 2012. 116(5): p. 3320-3328.
12. Zhu, Z., et al., *Superstructures and SERS Properties of Gold Nanocrystals with Different Shapes*. Angewandte Chemie International Edition, 2011. 50(7): p. 1593-1596.
13. Guo, P., et al., *Plasmonic core-shell nanoparticles for SERS detection of the pesticide thiram: size- and shape-dependent Raman enhancement*. Nanoscale, 2015. 7(7): p. 2862-2868.
14. Si, K.J., et al., *Dual-Coded Plasmene Nanosheets as Next-Generation Anticounterfeit Security Labels*. Advanced Optical Materials, 2015: p. n/a-n/a.
15. Chen, Y., et al., *Ultrathin Plasmene Nanosheets as Soft and Surface-Attachable SERS Substrates with High Signal Uniformity*. Advanced Optical Materials, 2015. 3(7): p. 919-924.
16. Freeman, R.G., et al., *Self-Assembled Metal Colloid Monolayers: An Approach to SERS Substrates*. Science, 1995. 267(5204): p. 1629-1632.
17. Lee, W., et al., *Self-Assembled SERS Substrates with Tunable Surface Plasmon Resonances*. Advanced Functional Materials, 2011. 21(18): p. 3424-3429.
18. Pingping, Z., et al., *Large-scale uniform Au nanodisk arrays fabricated via x-ray interference lithography for reproducible and sensitive SERS substrate*. Nanotechnology, 2014. 25(24): p. 245301.
19. Nakagawa, Y., et al., *Formation of Monocrystalline 1D and 2D Architectures via Epitaxial Attachment: Bottom-Up Routes through Surfactant-Mediated Arrays of Oriented Nanocrystals*. Langmuir, 2015. 31(22): p. 6197-6201.

## Chapter 5

20. Bigioni, T.P., et al., *Kinetically driven self assembly of highly ordered nanoparticle monolayers*. Nat Mater, 2006. 5(4): p. 265-270.
21. Biswas, A., et al., *Advances in top-down and bottom-up surface nanofabrication: Techniques, applications & future prospects*. Advances in Colloid and Interface Science, 2012. 170(1-2): p. 2-27.
22. Cheng, W., et al., *Nanopatterning self-assembled nanoparticle superlattices by moulding microdroplets*. Nat Nano, 2008. 3(11): p. 682-690.
23. Cheng, J.Y., et al., *Templated Self-Assembly of Block Copolymers: Top-Down Helps Bottom-Up*. Advanced Materials, 2006. 18(19): p. 2505-2521.
24. Alexander, T.A. *Applications of surface-enhanced Raman spectroscopy (SERS) for biosensing: an analysis of reproducible, commercially available substrates*. 2005.
25. Alexander, T.A., *Development of Methodology Based on Commercialized SERS-Active Substrates for Rapid Discrimination of Poxviridae Virions*. Analytical Chemistry, 2008. 80(8): p. 2817-2825.
26. Alexander, T.A., P.M. Pellegrino, and J.B. Gillespie, *Near-Infrared Surface-Enhanced-Raman-Scattering-Mediated Detection of Single Optically Trapped Bacterial Spores*. Applied Spectroscopy, 2003. 57(11): p. 1340-1345.
27. Netti, M.C., et al. *Probing molecules by surface-enhanced Raman spectroscopy*. 2006.
28. Henzie, J., E.-S. Kwak, and T.W. Odom, *Mesoscale Metallic Pyramids with Nanoscale Tips*. Nano Letters, 2005. 5(7): p. 1199-1202.
29. Xu, Z., et al., *Monolithic Integrations of Slanted Silicon Nanostructures on 3D Microstructures and Their Application to Surface-Enhanced Raman Spectroscopy*. The Journal of Physical Chemistry C, 2012. 116(45): p. 24161-24170.
30. Chao, B.-K., et al., *Anti-reflection textured structures by wet etching and island lithography for surface-enhanced Raman spectroscopy*. Applied Surface Science, 2015. 357, Part A: p. 615-621.
31. Alba, M., et al., *Macroscopic Plasmonic Substrates for Highly Sensitive Surface-Enhanced Raman Scattering*. Angewandte Chemie International Edition, 2013. 52(25): p. 6459-6463.

## Chapter 5

32. Niu, W., et al., *Selective Synthesis of Single-Crystalline Rhombic Dodecahedral, Octahedral, and Cubic Gold Nanocrystals*. Journal of the American Chemical Society, 2009. 131(2): p. 697-703.
33. Gosálvez, M.A. and R.M. Nieminen, *Surface morphology during anisotropic wet chemical etching of crystalline silicon*. New Journal of Physics, 2003. 5(1): p. 100.
34. Sparacin, D.K., S.J. Spector, and L.C. Kimerling, *Silicon Waveguide Sidewall Smoothing by Wet Chemical Oxidation*. Journal of Lightwave Technology, 2005. 23(8): p. 2455.
35. Domenici, F., A.R. Bizzarri, and S. Cannistraro, *SERS-based nanobiosensing for ultrasensitive detection of the p53 tumor suppressor*. International Journal of Nanomedicine, 2011. 6: p. 2033-2042.
36. McLellan, J.M., et al., *Comparison of the surface-enhanced Raman scattering on sharp and truncated silver nanocubes*. Chemical Physics Letters, 2006. 427(1–3): p. 122-126.
37. Ko, H., S. Singamaneni, and V.V. Tsukruk, *Nanostructured Surfaces and Assemblies as SERS Media*. Small, 2008. 4(10): p. 1576-1599.
38. Wu, H.-L., et al., *A Comparative Study of Gold Nanocubes, Octahedra, and Rhombic Dodecahedra as Highly Sensitive SERS Substrates*. Inorganic Chemistry, 2011. 50(17): p. 8106-8111.
39. Haynes, C.L. and R.P. Van Duyne, *Plasmon-Sampled Surface-Enhanced Raman Excitation Spectroscopy*. The Journal of Physical Chemistry B, 2003. 107(30): p. 7426-7433.

---

## **Chapter 6      Conclusions                      and**

## **Recommendations for Future Work**

---



## Chapter 6

### 6.1 Conclusions

Despite the encouraging progresses in synthesizing metallic nanoparticles, it is still far from the capability of constructing any plasmonic arbitrary nanostructures with well-defined structures and finely-tunable properties. The contribution of this thesis is synthesis and characterization of few types of new plasmonic nanostructures, including plasmonic hairy gold nanorods, hairy bacteria, and nanoparticle pyramids. Also, it is the first time that SANS is used to reveal soft DNA corona structures. Below is the detailed description of my work.

Soft DNA corona structures have been investigated in detail by neutron scattering techniques and clearly demonstrate that DNA-capped gold nanoparticle conjugates form globular particles in the absence of salt, regardless of the DNA sequence. However, distinct behaviours were observed for palindromic and non-palindromic DNA sequences. The non-palindromic DNA sequences maintain a globular or sphere-like shape under all the conditions investigated here although their corona heights are responsive to ionic strength and temperature. However, the palindromic DNA corona only maintains a sphere-like shape in the absence of salt and quickly exhibits hand-shaking base-pairing interactions upon addition of salt, leading to dimeric and multimeric aggregates depending on ionic strength.

A new type of metal nanoarchitectures – hairy gold nanorods were successfully obtained by the two-step seed-mediated growth processes. The entire growth process was undertaken in aqueous environment. The hairy nanowires could be obtained in a wider range of ratios (2.5 to 25) of gold precursor to ligand than that reported on solid surfaces or silica beads in the literature. What is more,

## Chapter 6

width of nanowires would be controlled by the ratio, and width changed from 5nm to 9nm in this ratio range. It could control the length of nanowires from 47 nm to 15  $\mu\text{m}$ , simply by adjusting amount of nanorod. The unique hairy high-aspect-ratio gold nanowires tethered to concentric nanorod allowed for constructing flexible and stretchable percolation conductivity network. This conductive network could be used as high performance piezoresistive strain sensors with high stretchability and durability. Next, a novel plasmonic hairy bacteria structure was fabricated. In this initial *E. coli* bacteria were employed for the first time as templates for successful synthesis of hairy plasmonic nanostructure. Furthermore, it demonstrated that the ultrathin gold nanowires could be grown selectively on bacteria surface by a seed-mediated growth progress.

By combining bottom-up and top-down approaches, I have successfully assembled plasmonic pyramidal microstructure, with detailed investigation on the theoretical insights properties and surface-enhanced Raman scattering (SERS) applications. The rhombic dodecahedral (RD), octahedral and sphere nanoparticles was succeed to assembly pyramid building block under the template assisted. Due to the coupling effect of interparticles and pyramid structure, plasmon resonance red-shift from bottom to the tip of pyramid and the highest peak intensity at the middle of pyramid. All these pyramid films have been explored as SERS substrate to investigate the Raman intensity on shape effect. The pyramid tip showed the strongest Raman enhancement than other parts, and maximized Raman enhancement was achieved at pyramid substrate assembled by RD nanoparticles.

## Chapter 6

### 6.2 Recommendations for Future Work

In this thesis, the small angle neutron scattering technique was used to study the information of DNA capped on gold nanoparticles. From the investigation, the detailed information of DNA corona is obtained such as corona thickness decreased with increasing of salt concentration that can't be obtained from DLS data. This is the first time to using neutron technology investigate the structure of DNA-capped gold nanoparticles. In this preliminary study we only characterized the simple system--dispersed gold nanoparticles. Beyond this work results, more complex gold nanoparticle structure will be investigated by employing SANS technology in the future. In this study we fixed the length of DNA sequence to investigate the effect of temperature and salt concentration, which is the start of our neutron study of DNA capped gold nanoparticles. The length of DNA sequence is also an important factor in the conjugate and it is also reported that different types of salt ions can show different effect on the DNA-capped gold nanoparticles. Hence, more complex DNA sequences may be investigated in future.

Two new nanostructure are fabricated by wet chemical synthesis. Gold nanowires grow on the nanorod and bacteria template formed hairy gold nanorod and hairy gold bacteria structures. In this method, the gold nanowires can be grown on the substrate that scale range from bulk to macro-level and nano-level. These gold nanowire with high stability, good conductivity and high aspect ratio of nanowires is the perfect candidature for the electro sensors. In this preliminary study, only fundamental data about performance of sensor are tested. More investigations for sensor ability need to be done in the future. For example, as the length of nanowire is tunable, the effect of nanowire length on sensor ability

## Chapter 6

could be investigated. What is more, hairy nanorod applied in the strain sensor, hairy bacteria also can apply in the sensor.

In SERS measurement, the intensity strongly depends on the nature of the substrates such as the size and shape of nanoparticles as well as the interparticles distance and arrangement pattern. Fabricating substrate with high sensitivity and reproducibility is a crucial step for SERS enhancement. In this project, SERS substrate was fabricated by the template assisted self-assembly method. In this method, the template size is fixed (5  $\mu\text{m}$ ), in the future work different sizes of templates can be choose to assembly nanoparticles, so the size effect of templates on the SERS enhancement can be systemically investigated. The size of nanoparticles used in the assembly can also vary from 10 nm to 200 nm to study the nanoparticles effect on the SERS enhancement.

---

# **Appendix**

## **Publications Relevant to This Thesis**

---



# Probing Soft Corona Structures of DNA-Capped Nanoparticles by Small Angle Neutron Scattering

Wenjuan Yang,<sup>†,‡</sup> Jingxiong Lu,<sup>†</sup> Elliot Paul Gilbert,<sup>§</sup> Robert Knott,<sup>§</sup> Lizhong He,<sup>\*,†</sup> and Wenlong Cheng<sup>\*,†,‡</sup>

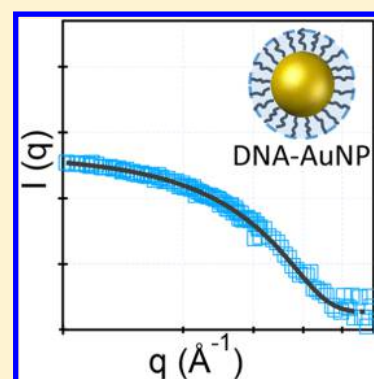
<sup>†</sup>Department of Chemical Engineering, Monash University, Clayton, Victoria 3800, Australia

<sup>‡</sup>The Melbourne Centre for Nanofabrication, 151 Wellington Road, Clayton, Victoria 3800, Australia

<sup>§</sup>Bragg Institute, Australian Nuclear Science and Technology Organisation (ANSTO), Locked Bag 2001, Kirrawee DC, New South Wales 2232, Australia

## S Supporting Information

**ABSTRACT:** Soft corona structures of DNA-capped nanoparticles are crucial for their applications in diagnostics, gene delivery, and superlattice growth. While conventional X-ray techniques can only provide information on their inorganic cores, here we report substantial new insights of DNA corona structures within DNA-capped nanoparticles in this first study employing small angle neutron scattering (SANS). Using two 15-mer DNA strands with palindromic sequence and poly(dT) sequence under high number density packing on gold nanoparticle surfaces, the influence of ionic strength and temperature on DNA corona structures and resultant hybridization has been investigated. Poly(dT) sequences were found to maintain globular corona structures across a range of ionic strengths and temperatures, but the corona thickness decreased with increasing salt concentration and increased with increasing temperature. In contrast, palindromic sequenced DNA had globular corona structures in the absence of salt but quickly evolved into dimeric and multimeric structures under high ionic strength or under low annealing temperatures. The structural insights revealed by SANS can guide the design of tailor-made DNA corona structures for customizable designer materials and devices.



## 1. INTRODUCTION

Since 1996, DNA-capped nanoparticles have demonstrated a plethora of exciting applications including advanced materials,<sup>1,2</sup> biodiagnostics,<sup>3,4</sup> and drug delivery.<sup>5</sup> It has been shown that they may be exploited to detect trace amounts of DNA,<sup>6</sup> protein,<sup>7,8</sup> small molecules,<sup>9</sup> and metal ions<sup>10–13</sup> as well as nanocarriers of nucleic acids for gene regulation.<sup>5,14</sup> In addition, DNA-capped nanoparticles are promising building blocks for novel plasmonic metamaterials and nanodevices.<sup>2,6,15</sup> They can be employed to build highly ordered superstructures with precise periodicity and complexity,<sup>16</sup> forming well-defined assemblies (“artificial molecules”<sup>17,18</sup> and “superacrystals”<sup>19–21</sup>).

For any particular application, the key parameters affecting DNA corona structures such as DNA sequence, length and number density, and ionic strength require a high degree of control and selection.<sup>15,19,22,23</sup> For example, it has been found that DNA density directly affects the cellular uptake efficiency of nanoparticles.<sup>24</sup> The DNA density on gold nanoparticle surfaces also influences the hybridization kinetics:<sup>25</sup> in the low density ( $<3 \times 10^{12}$  molecules/cm<sup>2</sup>) regime, almost all the DNA can be hybridized, and the kinetics of binding are faster; however, at a high density ( $<5 \times 10^{12}$  molecules/cm<sup>2</sup>), the extent of hybridization reduces by 10%, and the kinetics are much slower.

In principle, DNA molecules are polyelectrolytes which can form a brush-like polymer conformation on nanoparticles, with mushroom, crossover, and highly stretched regimes depending on the grafting number densities.<sup>26</sup> Dynamic light scattering has shown that highly stretched DNA brush heights correspond to the length of single-stranded DNA.<sup>15</sup> The microcantilever technique has also indicated that the pH-dependent changes of DNA conformation occur, revealing the effects of hydration and electrostatic forces on DNA hybridization.<sup>27</sup> In addition, curvature of the particle surface can affect DNA loading capacity and DNA hybridization.<sup>28</sup> Smaller nanoparticles show a higher probe-loading capacity than the larger ones, and when particle diameter increases to 60 nm, DNA packing is similar to that of a planar metal surface.<sup>29</sup> Classical density functional theory and molecular dynamics simulations have been utilized to develop a cell model to predict the ion cloud around spherical nanoparticles affected by DNA densities, bulk ionic concentrations, and the sizes of nanoparticles and chains.<sup>30</sup>

Despite these advances, complex DNA corona structures remain elusive. Recent advances in synchrotron-based X-ray techniques have revealed the crystalline structures of DNA-

Received: May 11, 2015

Revised: July 21, 2015

Published: July 23, 2015

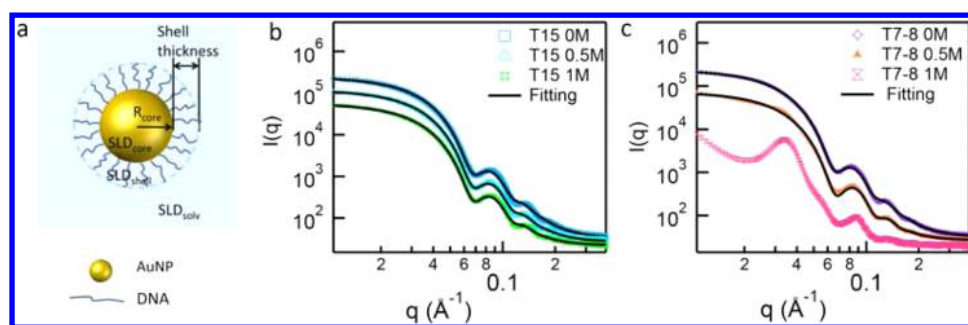


**Figure 1.** (a) Schematic of the DNA-Au conjugate in the polycore-shell model. SAXS scattering data of T15 (b) and T7-8(c) at various salt concentrations (0 M, 0.5 M, and 1 M). Solid lines show the fits by Schulz distribution of spheres.

capped nanoparticle assemblies under various conditions<sup>15,19,23,31</sup> but provided no information on the DNA corona since the scattering signals mainly arise from the electron-dense nanoparticle cores.<sup>32</sup> However, it is possible to manipulate the signal from the DNA corona using small angle neutron scattering (SANS) combined with solvent contrast variation, and this forms the motivation for the present investigation.

## 2. RESULTS AND DISCUSSION

As a model system, two thiolated 15-mer single stranded DNA (ssDNA) strands were selected. The first one has nonbase-pairing poly thymine sequence (5'-SH-T<sub>15</sub>-3', denoted as T15) while the second one comprises a segment of 7 thymine bases at the 5' end followed by a palindromic segment with 8 bases (5'-SH-T<sub>7</sub>-CTCATGAG-3', denoted as T7-8). Following the previous protocol,<sup>15</sup> the two types of DNA strands were conjugated to spherical ~13 nm gold nanoparticle surfaces with nearly highest number density. The as-prepared conjugates are stable at high ionic strength and a wide range of temperatures without forming permanent aggregates.

By combined small-angle X-ray scattering (SAXS) and SANS, the effects of salt concentration on the two types of DNA coronas at 22 °C were first examined (Figures 1 and 2).

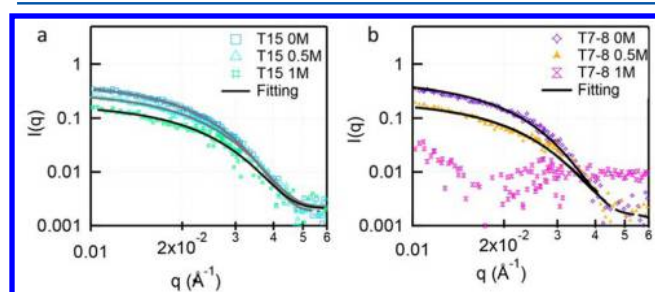


**Figure 2.** SANS scattering data of T15 (a) and T7-8 (b) at various salt concentrations (0 M, 0.5 M, and 1 M). Solid lines show the fits by the polycore-shell model.

While the scattering curves of T15-AuNP have similar shapes in 10 mM Tris buffer (pH 7.2) under different salt concentrations (Figures 1b and 2a), there are significant changes in the scattering curves for T7-8-AuNP at increased salt concentration (Figures 1c and 2b). Particularly, a peak in the low  $q$  region emerged when the salt concentration increased to 1 M. Model-independent analysis via Indirect Fourier Transform (IFT) shows that T15-AuNP and T7-8-AuNP have almost identical symmetric bell-shaped pair-distance distribution,  $p(r)$ , functions, suggesting these two DNA sequences give the same

spherical shape as the conjugates in the absence of salt.<sup>33</sup> In accord with their similar  $p(r)$  functions, IFT yielded particles of a similar radius of gyration,  $R_g$  (88.0 Å for T15-AuNP and 87.9 Å for T7-8). Although the  $R_g$  values from Guinier analysis are slightly higher than those from IFT, T15-AuNP and T7-8-AuNP have similar values (90.6 and 90.3 Å, respectively). Also, both particles have a similar hydrodynamic radius (DLS measurements, Table S1) in the absence of salt.

However, T15-AuNP and T7-8 AuNP show significant differences in both  $R_g$  and  $p(r)$  functions at higher salt concentrations. While the  $R_g$  value of T15-AuNP decreases from 88.0 to 83.4 Å (0.5 M NaCl) and 81.4 Å (1 M NaCl), the  $R_g$  value of T7-8-AuNP increases from 87.9 to 132.1 Å (0.5 M NaCl). As shown in Figure 3a, there is a slight decrease in maximum diameter ( $D_{\text{max}}$ ) in the  $p(r)$  function for T15-AuNP at higher salt concentration, and the T15 conjugate retains a bell-shape  $p(r)$ . This suggests that the shape of the T15 conjugate remains largely the same, although its size is smaller.

In contrast, there are two peaks in the distribution function for the T7-8 conjugate in 0.5 M salt, suggesting that the palindromic DNA hybrid possibly forms a dimer structure (Figure 3d). The first peak shows the same position as T15, corresponding to the remaining monomers of T7-8. The second peak is an indication of dimer formation. Consistent with IFT data, DLS data also shows two peaks for T7-8 at 0.5 M. With further salt increase to 1 M, the T7-8 conjugate aggregated to form a larger-scale cluster; the oscillations in the  $p(r)$  function are a result of data truncation due to the aggregates being larger than the inverse of minimum  $q$ . As a result, both  $D_{\text{max}}$  and  $R_g$  cannot be reliably determined for T7-8-AuNP at 1 M NaCl concentration due to the polydisperse nature of the aggregated system and the limit of  $q_{\text{min}}$ . Nevertheless, the SANS data reflects the aggregation of T7-8-AuNP at high salt concentrations. Aggregation was also confirmed by DLS measurements (Figure 3b). The different effects of salt on poly(dT) sequenced T15-AuNP and palindromic sequenced T7-8-AuNP are schematically presented in Figure 3c and d. For T7-8-AuNPs, their palindromic sequences hybridize at high ionic strength, resulting in the observed large aggregates. For T15-AuNPs, the DNA corona was compressed at higher salt concentration without the formation of aggregates.

Further analysis of the small-angle scattering data has been carried out by model-dependent fitting. Since the X-ray signal from the gold core vastly dominates that from the DNA, a model using a Schulz distribution of spheres is sufficient to describe the SAXS data (Figure 1b and c). In the absence of salt, the fitting gives the radius of the gold core as 63.8 and 65.7 Å for T15-AuNP and T7-8 conjugates with a small

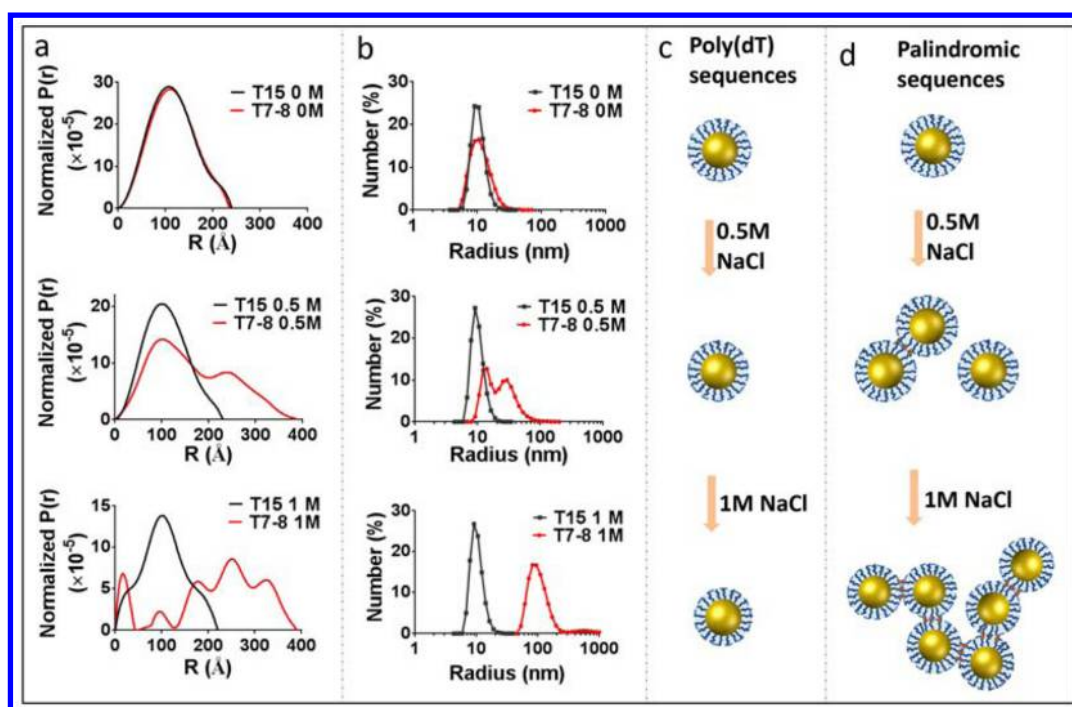


**Figure 3.** (a)  $p(r)$  function and (b) size distribution of T15 and T7-8 conjugates at various salt concentrations (0 M, 0.5 M, and 1 M) obtained from IFT analysis and DLS measurements, respectively. Panels c and d represent a scheme for the salt effect on poly(dT) sequences DNA and palindromic sequenced DNA.

**Table 1.** Fit Parameters from SAXS and SANS Data Using Schulz Sphere Distribution and the Polycore–Shell Model, respectively

sample	salt concentration (M)	SAXS		SANS				
		AuNP core radius ( $\text{\AA}$ )	polydispersity	shell thickness ( $\text{\AA}$ )	SLD of shell ( $\times 10^{-6} \text{\AA}^{-2}$ )	shell volume ( $\times 10^3 \text{\AA}^3$ )	DNA molecular volume ( $\times 10^3 \text{\AA}^3$ )	DNA fraction v/v % in shell
T15-AuNP	0	63.8	0.128	65.8	6.00	8.06	4.63	11.08
T15-AuNP	0.5	64.0	0.125	60.7	5.97	7.02	4.41	12.05
T15-AuNP	1	64.1	0.120	59.1	5.95	6.73	4.31	12.31
T7-8-AuNP	0	65.7	0.126	65.2	5.96	8.21	4.78	13.80

polydispersity value of 0.128 and 0.126, respectively. To fit the SANS data, a core–shell model was used that accounts for the contributions both from the gold core and the DNA corona (Figure 2). The values from the SAXS fits are used to constrain the core parameters (size and polydispersity) in the SANS fitting. As the scattering length density of the solution and gold core can be determined from their mass density and chemical composition (Table S2), only the thickness and scattering length density of the shell are refinable parameters for the fitting of SANS data. The resultant parameters for the core–shell models at different salt concentrations are summarized in Table 1. Note that no model fitting has been attempted for T7-8-AuNP at 0.5 and 1 M due to the aggregation.

In the absence of salt, the thickness of the T7-8 corona (65.2  $\text{\AA}$ ) is similar to the T15 corona (65.8  $\text{\AA}$ ) while its SLD ( $5.96 \times 10^{-6} \text{\AA}^{-2}$ ) is slightly smaller than the T15 corona ( $6.00 \times 10^{-6} \text{\AA}^{-2}$ ). Note that the T15 molecule has a smaller scattering length ( $1.517 \times 10^{-10} \text{ cm}$ ) and hence a higher contrast than T7-8 ( $1.715 \times 10^{-10} \text{ cm}$ ) with respect to  $\text{D}_2\text{O}$  (Table S3). However, there are fewer oligomers on T15-AuNP

( $192 \pm 8$  oligonucleotides per particle) than T7-8 ( $237 \pm 13$  oligonucleotides/particle) as determined from the DNA adsorption curve (Figure S1). These two opposing effects result in similar shell scattering length density for both particles. Despite the difference in their surface coverage, the T15 corona and T7-8 corona have similar values of shell thickness, suggesting that both DNAs extend from the gold particle surface in a similar configuration. In fact, the  $p(r)$  functions of T15 and T7-8 share a similar shape (Figure 3a), suggesting a similar conformation of T15 and T7-8 in the absence of salt.

As the palindromic sequence T7-8-AuNP forms aggregates at high salt concentrations, the following discussions on the salt-induced conformation change of DNA are focused on poly(dT) sequences T15-AuNP. Importantly, the increase of the salt concentration does not change the polydispersity of T15-AuNP (Supporting Information), confirming that the system is well dispersed even at high salt concentration. Although salt did not affect the shape of the poly(dT) sequenced DNA capped conjugate, the thickness of the DNA corona decreases with salt addition. The shell thickness of the

T15 conjugate (from the polycore–shell model) reduced from 65.8 Å (0 M NaCl) to 60.7 Å (0.5 M NaCl) and 59.1 Å (1 M NaCl). As the salt concentration increases, excess cations are anticipated to reduce repulsion along the negatively charged backbone of the DNA, thus resulting in a compaction of the DNA corona. Our findings are consistent with Chen et al. which also showed that the length of poly(dT) sequences of DNA in free solution decreased with increased salt concentration.<sup>34</sup> It is possible that electrostatic repulsion within the DNA chain is sufficiently depressed at a salt concentration of 0.5 M, and further DNA compaction is reduced when salt concentration is increased to 1 M.

A decrease of the shell thickness from 65.8 Å (0 M salt) to 60.7 Å (0.5 M salt) corresponds to a change of shell volume from  $8.06 \times 10^6 \text{ Å}^3$  to  $7.02 \times 10^6 \text{ Å}^3$ . Note that the corona is occupied by DNA and solvent; as a result, the decrease in the shell volume would imply a reduction in proportion of solvent in the corona. Since the SLD of the solvent is greater than that of DNA, decreased solvation would therefore result in a decrease in the corona SLD. However, this is not observed here. In the absence of salt, the difference of SLD between the shell ( $6.00 \times 10^{-6} \text{ Å}^{-2}$ ) and the solvent ( $6.34 \times 10^{-6} \text{ Å}^{-2}$ ) is  $0.34 \times 10^{-6} \text{ Å}^{-2}$ ; at a salt concentration of 0.5 M, the contrast between the shell ( $5.97 \times 10^{-6} \text{ Å}^{-2}$ ) and the solvent ( $6.31 \times 10^{-6} \text{ Å}^{-2}$ ) remains as  $0.34 \times 10^{-6} \text{ Å}^{-2}$ , i.e., the smaller volume of the DNA corona does not lead to an increase in contrast between the DNA shell and bulk solvent. The observed behavior may arise from either a decrease in volume of the DNA itself, an increase in the physical density of the solvent in the corona (decrease in solvent volume) compared to the bulk, or a combination thereof. Further calculations (see Supporting Information) assuming solely the former effect suggest that the molecular volume of DNA decreases from  $4.63 \times 10^3 \text{ Å}^3$  (0 M NaCl) to  $4.41 \times 10^3 \text{ Å}^3$  (0.5 M NaCl) and  $4.31 \times 10^3 \text{ Å}^3$  (1 M NaCl). Thus, the increase of salt concentration does not only result in a decrease in the total volume of the DNA corona but also the volume occupied by individual DNA chains. However, this does not preclude the influence of solvent density increase in the corona. In an analysis of the protein–solvent interface, it is demonstrated that the hydration shell around proteins is denser than the bulk solvent.<sup>35</sup>

The influence of temperature was also investigated by SANS (Figure 4) at a fixed salt concentration of 0.5 M by measuring

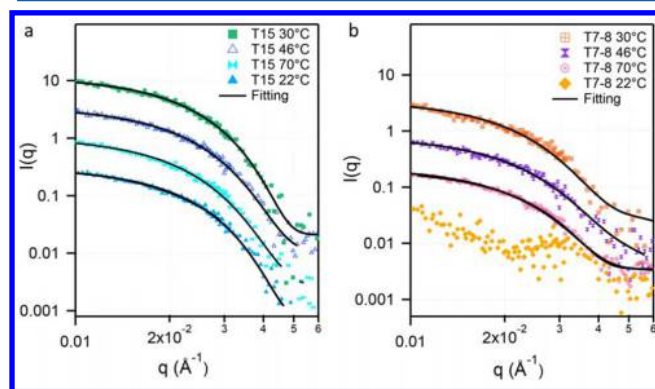


**Figure 4.** SANS scattering data of T15 (a) and T7–8 (b) as a function of temperature. Solid lines show the fits by the polycore–shell model. The plotted data are offset for clarity as follows: 10× for T15 70 °C and T7–8 46 °C; 20× for T15 46 °C and T7–8 70 °C; and 30× for T15 30 °C.

the scattering at an initial 30 to 46 °C, 70 °C, and then decreasing to 22 °C.  $p(r)$  functions are shown in Figure 5. The T15 conjugate maintains a bell-shape function as the temperature is changed, which indicates that the particle shape is largely conserved (Figure 5a). The  $p(r)$  function of the T7–8 conjugate maintains two peaks at 30 °C, but as the temperature is increased from 30 to 46 °C, the T7–8 conjugate  $p(r)$  function changed from two peaks to a single bell-shape peak (Figure 5b) suggesting a dimer to globule transition. Figure 5b shows the schematic of the shape change at different temperatures for palindromic sequenced DNA conjugates. DNA dehybridization occurs on increasing the temperature to 46 °C; this is above the melting temperature of 8-base palindromic sequences (35–37 °C, at 50  $\mu\text{M}$  DNA and 0.5 M salt conditions calculated by an IDT OligoAnalyzer). As the temperature is further increased from 46 to 70 °C, the globular structure remains unchanged. However, when the temperature is reduced from 70 to 22 °C, the T7–8 conjugate forms larger-scale clusters (as observed by the data-truncated oscillations in the  $p(r)$  function). The possible explanation for this interesting behavior is that palindromic sequenced T7–8 reforms to the hybrid state on cooling, and annealing enables more DNA strands to hybridize to form clusters. Indeed in Mirkin and Gang's studies,<sup>19,20</sup> it was found that slow annealing of DNA-capped gold nanoparticles can lead to particle self-assembly and crystallization to form ordered structures. Interparticle organization of such crystalline nanostructure could also be investigated by neutron scattering.

The corona of the poly(dT) sequenced DNA capped conjugate increased slightly on increasing temperature but appears to be reversible; from Table S4, the shell thickness of T15 increased from 60.4 Å (30 °C) to 60.5 Å (46 °C), 65.1 Å (70 °C), and decreased to 60.9 Å at 22 °C. Similarly, the increased and decreased corona thickness resulted in fluctuation of the corona SLD. The DNA corona size change is also confirmed by  $R_g$  values from both IFT and Guinier analysis (Table S4). These findings are consistent with Jiang et al., who also showed that ssDNA stretched as temperature was increased.<sup>36</sup>

### 3. CONCLUSIONS

In conclusion, soft DNA corona structures have been investigated in detail by neutron scattering techniques and clearly demonstrate that DNA-capped gold nanoparticle conjugates form globular particles in the absence of salt, regardless of the DNA sequence. However, distinct behaviors were observed for palindromic and nonpalindromic DNA sequences. The nonpalindromic DNA sequences maintain a globular or sphere-like shape under all the conditions investigated here, although their corona heights are responsive to ionic strength and temperature. However, the palindromic DNA corona only maintains a sphere-like shape in the absence of salt and quickly exhibits hand-shaking base-pairing interactions upon addition of salt, leading to dimeric and multimeric aggregates depending on ionic strength. Our work has demonstrated that small angle neutron scattering can provide structural insights on DNA-capped gold nanoparticles, and this opens the way to systematically study effects of different factors such as DNA length and type of ions on DNA structure in future. The results shown here may guide the design of tailor-made DNA corona structures for customizable designer materials for versatile applications in a range of arenas including life sciences and optoelectronics.

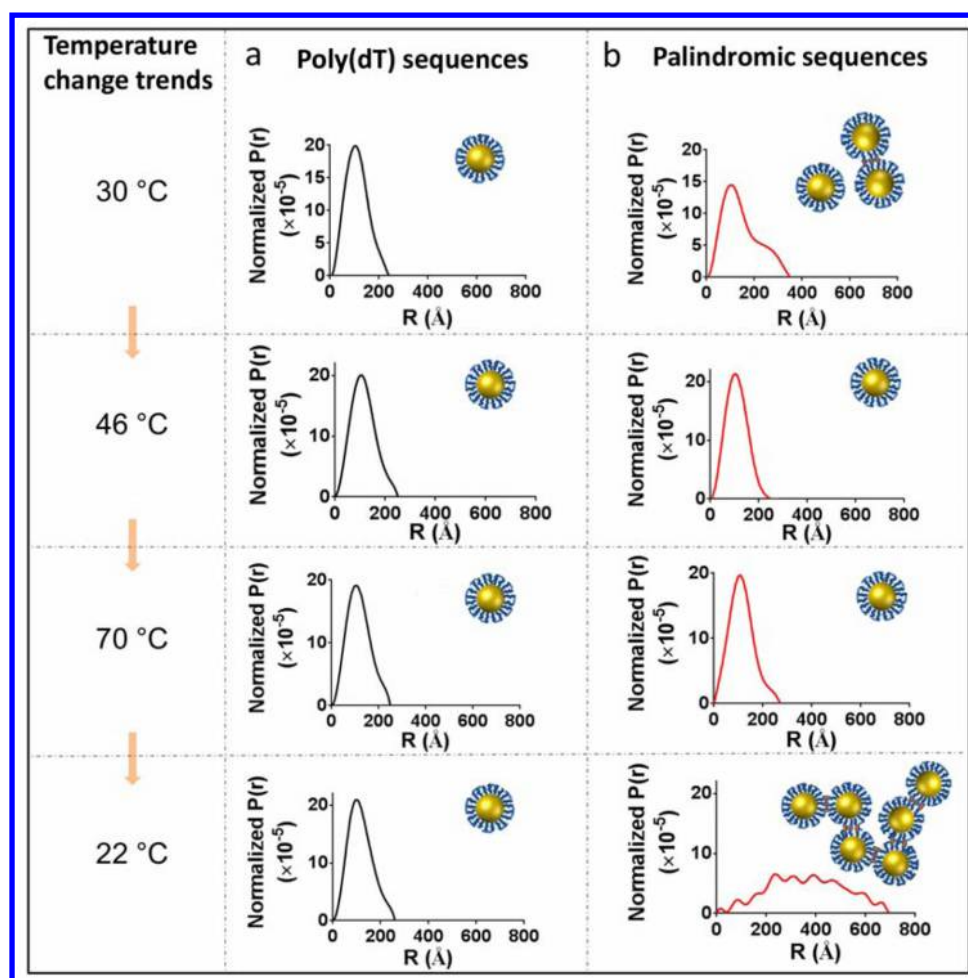


**Figure 5.**  $p(r)$  distribution of T15 (a) and T7–8 (b) conjugates computed at various temperatures (30 °C, 46 °C, 70 °C, and 22 °C) in 0.5 M salt buffer. Insets are the scheme of temperature effect on poly(dT) sequenced DNA and palindromic sequenced DNA.

## ■ ASSOCIATED CONTENT

### Supporting Information

The Supporting Information is available free of charge on the ACS Publications website at DOI: 10.1021/acs.jpcc.5b04494.

Experimental details and data  
(PDF)

## ■ AUTHOR INFORMATION

### Corresponding Authors

[Redacted contact information]

### Notes

The authors declare no competing financial interest.

## ■ ACKNOWLEDGMENTS

This research was financially supported under Australian Research Council's Discovery projects funding scheme (DP120100170 and DP140100052) and AINSE E06001 2437579 (GL 732041). This work was performed in part at the Melbourne Centre for Nanofabrication (MCN) in the Victorian Node of the Australian National Fabrication Facility (ANFF). Scattering measurements were performed at the Australian Nuclear Science and Technology Organisation

(ANSTO) on the 40 meter QUOKKA SANS and Bruker Nanostar SAXS instruments.

## ■ REFERENCES

- (1) Alivisatos, A. P.; Johnsson, K. P.; Peng, X.; Wilson, T. E.; Loweth, C. J.; Bruchez, M. P.; Schultz, P. G. Organization of 'nanocrystal molecules' using DNA. *Nature* **1996**, *382*, 609–611.
- (2) Mirkin, C. A.; Letsinger, R. L.; Mucic, R. C.; Storhoff, J. J. A DNA-based method for rationally assembling nanoparticles into macroscopic materials. *Nature* **1996**, *382*, 607–609.
- (3) Elghanian, R.; Storhoff, J. J.; Mucic, R. C.; Letsinger, R. L.; Mirkin, C. A. Selective colorimetric detection of polynucleotides based on the distance-dependent optical properties of gold nanoparticles. *Science* **1997**, *277*, 1078–1081.
- (4) Dubertret, B.; Calame, M.; Libchaber, A. J. Single-mismatch detection using gold-quenched fluorescent oligonucleotides. *Nat. Biotechnol.* **2001**, *19*, 365–370.
- (5) Rosi, N. L.; Giljohann, D. A.; Thaxton, C. S.; Lytton-Jean, A. K. R.; Han, M. S.; Mirkin, C. A. Oligonucleotide-modified gold nanoparticles for intracellular gene regulation. *Science* **2006**, *312*, 1027–1030.
- (6) Li, H. X.; Rothberg, L. Colorimetric detection of DNA sequences based on electrostatic interactions with unmodified gold nanoparticles. *Proc. Natl. Acad. Sci. U. S. A.* **2004**, *101*, 14036–14039.
- (7) Pavlov, V.; Xiao, Y.; Shlyahovsky, B.; Willner, I. Aptamer-functionalized Au nanoparticles for the amplified optical detection of thrombin. *J. Am. Chem. Soc.* **2004**, *126*, 11768–11769.

- (8) Huang, C. C.; Huang, Y. F.; Cao, Z.; Tan, W.; Chang, H. T. Aptamer-modified gold nanoparticles for colorimetric determination of platelet-derived growth factors and their receptors. *Anal. Chem.* **2005**, *77*, 5735–5741.
- (9) Liu, J.; Lu, Y. Fast colorimetric sensing of adenosine and cocaine based on a general sensor design involving aptamers and nanoparticles. *Angew. Chem., Int. Ed.* **2005**, *45*, 90–94.
- (10) Li; Rothberg, L. J. Label-free colorimetric detection of specific sequences in genomic DNA amplified by the polymerase chain reaction. *J. Am. Chem. Soc.* **2004**, *126*, 10958–10961.
- (11) Wang, Z. D.; Lee, J. H.; Lu, Y. Label-free colorimetric detection of lead ions with a nanomolar detection limit and tunable dynamic range by using gold nanoparticles and DNAzyme. *Adv. Mater.* **2008**, *20*, 3263–3267.
- (12) Liu, C.-W.; Hsieh, Y.-T.; Huang, C.-C.; Lin, Z.-H.; Chang, H.-T. Detection of mercury(II) based on Hg<sup>2+</sup>-DNA complexes inducing the aggregation of gold nanoparticles. *Chem. Commun.* **2008**, 2242–2244.
- (13) Wang, L.; Liu, X.; Hu, X.; Song, S.; Fan, C. Unmodified gold nanoparticles as a colorimetric probe for potassium DNA aptamers. *Chem. Commun.* **2006**, 3780–3782.
- (14) Seferos, D. S.; Prigodich, A. E.; Giljohann, D. A.; Patel, P. C.; Mirkin, C. A. Polyvalent DNA nanoparticle conjugates stabilize nucleic acids. *Nano Lett.* **2009**, *9*, 308–311.
- (15) Cheng, W.; Campolongo, M. J.; Cha, J. J.; Tan, S. J.; Umbach, C. C.; Muller, D. A.; Luo, D. Free-standing nanoparticle superlattice sheets controlled by DNA. *Nat. Mater.* **2009**, *8*, 519–525.
- (16) Tan, S. J.; Campolongo, M. J.; Luo, D.; Cheng, W. L. Building plasmonic nanostructures with DNA. *Nat. Nanotechnol.* **2011**, *6*, 268–276.
- (17) Maye, M. M.; Kumara, M. T.; Nykypanchuk, D.; Sherman, W. B.; Gang, O. Switching binary states of nanoparticle superlattices and dimer clusters by DNA strands. *Nat. Nanotechnol.* **2010**, *5*, 116–120.
- (18) Urzhumov, Y. A.; Shvets, G.; Fan, J. A.; Capasso, F.; Brandl, D.; Nordlander, P. Plasmonic nanoclusters: a path towards negative-index metafluids. *Opt. Express* **2007**, *15*, 14129–14145.
- (19) Nykypanchuk, D.; Maye, M. M.; van der Lelie, D.; Gang, O. DNA-guided crystallization of colloidal nanoparticles. *Nature* **2008**, *451*, 549–552.
- (20) Auyeung, E.; Li, T. I. N. G.; Senesi, A. J.; Schmucker, A. L.; Pals, B. C.; de la Cruz, M. O.; Mirkin, C. A. DNA-mediated nanoparticle crystallization into Wulff polyhedra. *Nature* **2014**, *505*, 73–77.
- (21) Cheng, W. L.; Hartman, M. R.; Smilgies, D.-M.; Long, R.; Campolongo, M. J.; Li, R.; Sekar, K.; Hui, C.-Y.; Luo, D. Probing in real time the soft crystallization of DNA-capped nanoparticles. *Angew. Chem., Int. Ed.* **2010**, *49*, 380–384.
- (22) Tan, S. J.; Kahn, J. S.; Derrien, T. L.; Campolongo, M. J.; Zhao, M.; Smilgies, D.-M.; Luo, D. Crystallization of DNA-capped gold nanoparticles in high-concentration, divalent salt environments. *Angew. Chem., Int. Ed.* **2014**, *53*, 1316–1319.
- (23) Park, S. Y.; Lytton-Jean, A. K. R.; Lee, B.; Weigand, S.; Schatz, G. C.; Mirkin, C. A. DNA-programmable nanoparticle crystallization. *Nature* **2008**, *451*, 553–556.
- (24) Giljohann, D. A.; Seferos, D. S.; Patel, P. C.; Millstone, J. E.; Rosi, N. L.; Mirkin, C. A. Oligonucleotide loading determines cellular uptake of DNA-modified gold nanoparticles. *Nano Lett.* **2007**, *7*, 3818–3821.
- (25) Peterson, A. W.; Heaton, R. J.; Georgiadis, R. M. The effect of surface probe density on DNA hybridization. *Nucleic Acids Res.* **2001**, *29*, 5163–5168.
- (26) Brittain, W. J.; Minko, S. A structural definition of polymer brushes. *J. Polym. Sci., Part A: Polym. Chem.* **2007**, *45*, 3505–3512.
- (27) Zhang, J.; Lang, H. P.; Yoshikawa, G.; Gerber, C. Optimization of DNA hybridization efficiency by pH-driven nanomechanical bending. *Langmuir* **2012**, *28*, 6494–6501.
- (28) Demers, L. M.; Mirkin, C. A.; Mucic, R. C.; Reynolds, R. A.; Letsinger, R. L.; Elghanian, R.; Viswanadham, G. A fluorescence-based method for determining the surface coverage and hybridization efficiency of thiol-capped oligonucleotides bound to gold thin films and nanoparticles. *Anal. Chem.* **2000**, *72*, 5535–5541.
- (29) Hill, H. D.; Millstone, J. E.; Banholzer, M. J.; Mirkin, C. A. The role radius of curvature plays in thiolated oligonucleotide loading on gold nanoparticles. *ACS Nano* **2009**, *3*, 418–424.
- (30) Zwanikken, J. W.; Guo, P.; Mirkin, C. A.; Olvera de la Cruz, M. Local ionic environment around polyvalent nucleic acid-functionalized nanoparticles. *J. Phys. Chem. C* **2011**, *115*, 16368–16373.
- (31) Campolongo, M. J.; Tan, S. J.; Smilgies, D.-M.; Zhao, M.; Chen, Y.; Xhangolli, I.; Cheng, W.; Luo, D. Crystalline Gibbs monolayers of DNA-capped nanoparticles at the air–liquid interface. *ACS Nano* **2011**, *5*, 7978–7985.
- (32) Von White, G.; Mohammed, F. S.; Kitchens, C. L. Small-angle neutron scattering investigation of gold nanoparticle clustering and ligand structure under antisolvent conditions. *J. Phys. Chem. C* **2011**, *115*, 18397–18405.
- (33) Svergun, D. Determination of the regularization parameter in indirect-transform methods using perceptual criteria. *J. Appl. Crystallogr.* **1992**, *25*, 495–503.
- (34) Chen, H.; Meisburger, S. P.; Pabit, S. A.; Sutton, J. L.; Webb, W. W.; Pollack, L. Ionic strength-dependent persistence lengths of single-stranded RNA and DNA. *Proc. Natl. Acad. Sci. U. S. A.* **2012**, *109*, 799–804.
- (35) Svergun, D. I.; Richard, S.; Koch, M. H. J.; Sayers, Z.; Kuprin, S.; Zaccai, G. Protein hydration in solution: experimental observation by x-ray and neutron scattering. *Proc. Natl. Acad. Sci. U. S. A.* **1998**, *95*, 2267–2272.
- (36) Jiang, H.-R.; Sano, M. Stretching single molecular DNA by temperature gradient. *Appl. Phys. Lett.* **2007**, *91*, 154104.